Theoretical Study and Experimental Implementation of an Ion-Nanowire Hybrid System

Inauguraldissertation

zur

Erlangung der Würde eines Doktors der Philosophie

vorgelegt der

Philosophisch-Naturwissenschaftlichen Fakultät

der Universität Basel

von

Panagiotis Fountas

aus Athen, Griechenland

Basel, 2020

Genehmigt von der Philosophisch-Naturwissenschaftlichen Fakultät
auf Antrag von

Prof. Dr. Stefan Willitsch
(Universität Basel)
Fakultätsverantwortlicher/Dissertationsleiter

Prof. Dr. Martino Poggio
(Universität Basel)
Korreferent

Prof. Dr. Martin Spiess
(Dekan)

Basel, den 26.05.2020

Abstract

Numerous efforts are currently aiming at the implementation of hybrid quantum systems in the quest for developing new devices for quantum technologies. The motivation for a solid state-atomic interface emerges from the possibility to couple otherwise incompatible platforms in order to combine the advantages of both in a complementary fashion. Under this scope, we report in this thesis the implementation of a new quantum device for the interface of an ultracold trapped ion and a conductive nanowire. The experimental measurements obtained here seem promising for the realization of the hybrid dynamics of the ion-nanowire hybrid system. Additionally, we performed numerical calculations in order to characterize the perturbation of the trapping potential for the ion by the nanowire. From our classical and quantum dynamics calculations we explored possibilities of generating Gaussian and non-Gaussian quantum states of the ion from the nanowire drive. Our modelling indicated, also, that sympathetic cooling and quantum entanglement can be realized when both subsystems operate in the quantum regime. The present ion-nanowire hybrid system might prove promising as a new quantum device for quantum information and quantum sensing experiments, for spectroscopy and for mass spectrometry.

Acknowledgements

I would like to thank my supervisors, Professor Stefan Willitsch and Professor Martino Poggio for giving me the opportunity to study in Basel and entrusting me with this project. I would also like to thank all the members of the Willitsch group. Special thanks to Claudio von Planta, for providing me his software for live pressure measurements and for the great times inside and outside University. I would like to thank Ziv Meir for his helpful input on some laser and electronics occasions, Kaveh Najafian for his help with the RF resonator, and to Ardita Kilaj for guiding me during the bakeout process of the chamber. I would, also, like to thank Moritz Weegen for his help in the lab during the final stages of the project, and wish him good luck for the next stages. I would like to thank all the members from Poggio group for the great times we had, especially during extracurricular activities (football, hockey, bbq etc.). Special thanks to Marcus Wyss for guiding me and training me patiently with the equipment that I needed to use during the fabrication process of the chip trap. Many thanks, also, to Nicola Rossi for useful discussions around the nanomechanical setup and for providing me the nanomechanical readout software. I would also like to acknowledge Dr. Roman Schmied and Dr. Niels Lörch for their fruitful discussions during the initial stage of the quantum calculations.

Many special thanks all the staff of the mechanical workshop, Philipp Knöpfel and Grischa Martin, in making all the custom-made parts of the apparatus, and in guiding me during the design of the ion trap. Special thanks also to Georg Holderied for guiding me and helping me with the electrical circuits of the experiment, as well as to Anatoly Johnson for his input in my laser setup. I am really grateful to Beat Lüscher of the Fachhochschule Nordwestschweiz for his extraordinary laser-cutting work on the wafers of my chip trap.

I would like to gratefully acknowledge the funding for this project from the Swiss Nanoscience Institute (P1407), as well as the funding from the Swiss National Science Foundation through the National Center of Competence in Research "Quantum Science and Technology".

Finishing the acknowledgements, many special and great thanks should go to my family, my two parents, my two brothers and my sister. And last but definitely not least to Christiana, for her constant support, her amazing patience throughout my PhD, and being there for me at any time, and so much more.

Contents

List of Figures

List of Tables

Chapter 1

Introduction

Quantum physics has extended our understanding of physical phenomena that classical physics failed to describe, and it was a major catalyst for a large number of technological inventions. Starting from the groundbreaking work of M. Planck in 1900, where the energy-'quanta' was introduced to describe the spectrum of blackbody radiation, through the A. Einstein's generalization of Planck's concept to explain the photo-electric effect, a full theory of quantum mechanics was developed in the 1920s. At that time many experiments were performed on ensembles of particles, where many quantum states were measured at once, thus leading to the invention of devices that were using the emergent phenomena from quantum physics.

Over the last three decades, we are experiencing a second technological jump, where the constructed quantum devices are using directly the quantum states and their properties, rather than as emergent phenomena, that was seen in the experiments laid in 1970s and 1980s by Serge Haroche and David Wineland, where the experimental methods used enabled the direct measurement and manipulation of individual quantum systems, that laid to a better control over quantum-matter. Apart from the atomic domain, experiments were performed with a wide variety of physical systems, ranging from solid-state devices featuring superconducting circuitry [5] to color-centers in diamonds [6,7]. A major goal of all these various research approaches is the realization of a large-scale quantum computer, which should outperform its classical counterpart in several computational tasks by manipulating directly the quantum systems [8]. Furthermore, there are various other application under this scope, that are more feasible with nowadays technology, like quantum communication [9] and

quantum enhanced metrology [10, 11], in the domains of time measurement [12, 13], magnetic fields [14] and gravitation [15, 16]. Those potential applications have attracted so much attention, that even big companies like Google, Microsoft and IBM are investing resources in this field of research.

However, one century after Planck's and Einstein's breakthroughs quantum physics still poses conceptual difficulties to the research community. The greatest challenge is the understanding of the transition from the microscopic world, governed by the laws of quantum mechanics, to the macroscopic world that is accurately described by classical mechanics. This is one of the most important reasons that many research teams are investing at the moment towards the research of coupled quantum and classical systems, often called *hybrid systems*. For the understanding of this quantum to classical transition it is essential that the quantum properties are protected against the harmful effects of their coupling to the environment. That is currently the greatest challenge for the technologies under development, that might lead to the next technological revolution.

From the quantum information perspective every quantum state may be used to encode information. The decay of the quantum state is synonymous to the loss of information it carries. Understanding decoherence in the context of quantum information, is understanding what happens to the information: if it is completely lost or if it is encoded in a different form or system. An example of a technique that preserves the information that is carried by a quantum state is the *spin echo* [17] that was developed in the field of nuclear magnetic resonance and is often used today in quantum information experiments. Another example of preservation of quantum state information is the Quantum Zeno effect, that was first observed by Itano *et al.* [18], where the Zeno's paradox was resolved by hindering the evolution of a quantum system through constant measurement, thus preserving its initial state.

An alternative approach is to construct quantum states robust against certain decay, that can be done by choosing convenient methods of encoding information, even encoding classical information. Some examples of this approach are the *magnetic field independent qubit* with trapped ions [19] or a *superconducting qubit* [20,21]. More complex versions of encoding information are examples of *decoherence free subspaces*

realized with trapped ions in [22, 23], where the quantum information is preserved at the expense of the system size.

In most of the cases the quantum information is encoded in the quantum counterpart of the classical bit that is called *qubit*. The classical bit can take only two states, namely 0 and 1, while the qubit can take the states $|0\rangle$, $|1\rangle$ and every possible superposition of those.

Furthermore, different encodings of quantum information are possible even with the use of continuous systems. These are typically more complex, but they may offer higher flexibility on encoding schemes. An example is the quantum harmonic oscillator, where two qubit states can be encoded in the complementary position and momentum states of the oscillator [24]. Additionally, the harmonic oscillator exists in both classical and quantum world, something that a spin system cannot offer. With the harmonic oscillator the quantum-classical divide can be studied, by exploring the differences of those two domains and the transition from one to another. Inspired by this, first experiments were performed by cooling a single ion to its motional ground state in a harmonic potential in 1995 [25] and again in the same year the cooling of an ensemble of $\sim 10^5$ neutral atoms forming a *Bose-Einstein condensate* was reported [26, 27].

Important experiments were performed by the Wineland group studying the quantum harmonic oscillator with the motional states of trapped ions. They were able to prepare fundamental, quasi-classical and non-classical states of motion like the coherent and squeezed states [28]. They have also demonstrated the creation of a unique motional state, the *Schrödinger's cat* state, where the ion's wavepacket was split spatially in two parts by a distance of more than ten times their size [29]. Recently, the creation of those motional states was performed by environmental engineering [30,31]. This technique was proposed in [32,33] and is similar to the ground-state cooling, but the difference lies in the direct preparation of superposition states. From this technique, a novel analysis method was developed, which allowed for the first time a phase and fidelity measurement for the prepared squeezed states with trapped ions [34]. It was also outlined that this dissipative state preparation may outperform traditional non-dissipative methods [35–37], and because of its generality it can be used to other physical systems, featuring superconducting or opto-mechanical candidates. More-

over, in a very recent publication [38], it was demonstrated that by accurately manipulating the superposition of two squeezed states, which are separated in space, it is possible to encode the qubit into the harmonic oscillator states of the trapped ion. In this way, a universal logical single qubit state was presented, which might open a route for exploring continuous variable error correction and hybrid quantum information schemes with discrete and continuous variables. Those encoded states can be applied also in quantum sensing experiments, allowing the simultaneous measurement of small displacements in both position and momentum.

Apart from the quantum information and quantum computing regime, trapped ions have already been used in a plethora of experiments. Being a well controlled isolated system, qubits from various ion sources have been implemented like Zeeman [39], hyperfine [40] and optical [41] qubits. Additionally, by trapping multiple ions together one can form spatially well defined ordered structures called Coulomb crystals. In these systems, molecular ions can be sympathetically cooled [42] by interacting with the crystallized atomic counterparts, high-precision spectroscopic measurements [43] have been demonstrated, as well as controlled chemical reactions [44, 45]. Even a heat engine was realized by using a single trapped ion [46].

So far, all of the aforementioned studies have shown an unprecedented level of coherent control of motional and spin degrees of freedom for the trapped ion. However, solid-state physicists have started to achieve similar level of control over individual vibrational modes of high-quality fabricated mechanical structures. In the very active field of optomechanics light forces are exploited for cooling and control of the vibrations of mechanical oscillators ranging from macroscopic mirrors to micro-membranes and nanoscale cantilevers [47–51]. Notably, the ground-state of a single mechanical mode of an optomechanical crystal was reached by laser cooling [52]. Experiments with other types of mechanical oscillators have also reached phonon occupation numbers very close to the ground state using laser cooling [53, 54]. In addition, very high-frequency oscillators have been cooled to their ground state by simply placing them in a dilution refrigerator [55], and by using additional radiation pressure cooling in the microwave domain [56].

Beyond cooling, a subsequent goal is to coherently control these mechanical devices on the quantum level, analogously to what has been achieved with atomic systems.

A necessary prerequisite for this is the quantum coherent coupling regime, where the fundamental quantum fluctuations of the mechanical oscillators equal or exceed their thermal fluctuations, and has been reached in experiments [54, 55, 57]. This would allow one to study quantum physics on a macroscopic scale [58, 59], possibly revealing yet unobserved quantum decoherence mechanisms [60–62]. From a more applied physics perspective, such devices provide quantum-limited force sensing in precision measurements. The limits of spatial resolution have been pushed to unprecedented levels, allowing to achieve subatomic resolution [63] and to image the chemical structure of a single molecule [64]. This type of force sensitivity provided by conventional cantilevers is usually enough to detect the strong short-range forces which dominate at sub-nanometric tip-sample separation. Also, other applications require sensitivity to small forces. These range from mass detection [65], to cantilever magnetometry [66,67], to observation of persistent currents in normal metal rings [68], to scanning measurements of friction forces [69, 70], to force-detected magnetic resonance [71, 72] and for simultaneously detecting and imaging in-plane nanoscale force fields [73, 74]. With the rise of nano-technologies, the sensitivity was pushed even further with the use of smaller mechanical force transducers, like nanowires and carbon nanotubes (CNTs) that have unprecedented mechanical properties. Doubly-clamped CNTs resonators have reached a record in force sensitivity of 1 $zN/\sqrt{Hz}$[1] [75, 76], thus enabling mass detection with a resolution of 1.7 yg[2] corresponding to the mass of one proton [77].

Combining all the aforementioned advancements in atomic and solid-state physics, a number of theoretical proposals have been published for the choice of proper candidates from both worlds for the realization of a hybrid system. On one hand, some studies have proposed the use of light forces to couple the motion of neutral atoms in a trap to the vibrations of a single mode of mechanical oscillators [78–88]. Additionally, the Treutlein group have studied different interfaces between atoms and mechanical oscillators based on magnetic [89], van der Waals [90] and optical forces [91–93]. On the other hand, only a few theoretical studies and proposals of hybrid systems consisting of trapped ions and nanooscillators have been published [94–96]. In [94] it was proposed that an ion trap could be built from conductive nanowires or nanotubes,

[1] 1 zeptoNewton = 10^{-21} N
[2] 1 yoctogram = 10^{-24} g

where one could realize the coupling of the nanoelectrodes with the motional modes of the ion. It was predicted that in this way the nanomechanical motion could be probed, the nanomechanical modes could be cooled, and entanglement between the fundamental modes of the two nanoelectrodes could be realized via the ion. In general, such a system could be advantageous for the implementation of higher frequency ion traps with faster qubit gates for quantum computing. Similarly, in [95] it was demonstrated theoretically that the ion could be used as a probe for the quantum nature of mesoscopic oscillators and that the modes of the nanooscillator could be cooled down to its ground state via the ion. Conversely, in [96] it was argued that ion-based hybrid systems are in general not favourable for implementing a hybrid quantum system due to the low coupling rates in comparison with the decoherence rates, and that trapped electrons may prove more advantageous for achieving higher cooling rates and for the implementation of faster gates.

In view of these varied and partly contrasting predictions about the possibilities offered by ion-nanomechanical hybrid systems, we study in this work the theoretical and experimental implementation of a trapped ultracold $^{40}Ca^{+}$ ion interacting with a metallic nanowire. As part of this thesis a new complex experimental apparatus was constructed, combining the two aforementioned objects each described from a fundamentally different theory. We present initially the characterization of the perturbation of the trapping potential by the nanowire using Finite Elements Calculations (FEM) and we define suitable parameters for the experimental implementation. We present, additionally, all the steps of the fabrication process for the ion trap, along with the rest of the components of the experimental apparatus. We, also, present results of Molecular Dynamics numerical calculations, with the custom implementation of the force-field describing the effect of the nanowire on the ion motion from the classical point of view. We show, then, how the approximation considering the nanowire as a point-like spherical particle can be implemented in a semi-classical fashion, where the motion of the ion is described quantum mechanically in a truncated Hilbert space. These calculations show how one can map the nanowire motion on the ion vibrational degrees of freedom, and how this can be read via the ion spin-motion coupling. Additionally, we present how at room temperature one can combine the trap anharmonicites and off-resonant drive of the nanowire in order to encode non-Gaussian

states (e.g. quantum information) on the ion. Moreover, we present the conditions under which a full quantum description of both systems can be done. In this case, we investigated the extremely low bath temperatures that one should achieve in order to sympathetically cool a carbon nanotube from a single trapped ion, which means the regime where the ion backaction on the nanowire stops being negligible. This cooling mechanism can be implemented with and without continuous laser cooling of the ion. Additionally, we present how the prepared quantum state of one system can be transferred onto the other, opening up in this way many possibilities in quantum information, where scalable quantum tranducers are required for long-distance operations. Finally, we present the first characterization measurements of the nanowire under non-optimal conditions and we discuss how this localized field, with accurate spatial positioning and highly interfaced with all the fields, might open pathways to a possible future experiments in the fields of energy, quantum metrology, quantum information and quantum computing, as well as alternative methods of ultrasensitive measurements.

The possibilities for future experiments and theoretical work are vast. This thesis presents the necessary steps towards the first experimental implementation of the ion-nanowire hybrid system, with the goal to push even further the technological complexity and versatility. The theory established as part of this work presents reasonable experimental observables, in different regimes, with the motivation to be expanded and include all possible interactions from the hybrid system, and ultimately to act as an optimization or prediction mechanism for future experiments. Possible future experimental improvements or theoretical approaches are discussed in the corresponding chapters.

Chapter 2

Theory of ion-trapping and nanomechanics

2.1 Radiofrequency ion traps

2.1.1 Linear Paul traps

Charged particles can be confined in ion traps with a combination of electric fields. According to *Earnshaw's theorem* it is not possible to create confining potentials along all three dimensions with only static electric fields [97]. In a *linear Paul trap* a static potential is applied along the longitudinal axis, which is also called axial direction or symmetry axis. For the sake of brevity we will denote in this chapter the symmetry axis as z. This creates a confining potential along the axial direction and an anti-confining potential in the radial plane perpendicular to the axial direction. For the radial confinement an oscillating electric field is applied in the radial direction, which forms a *pseudopotential*. Constraining the potential to only quadratic terms the overall potential near the geometrical center of the trap may be written as

$$\Phi(x,y,z,t) = \frac{V_{RF}}{2}\left(1 - \frac{(x^2-y^2)}{r_0^2}\right)\cos(\Omega_{RF}t) + \frac{\kappa U_{DC}}{z_0^2}\left(z^2 - \frac{x^2+y^2}{2}\right), \qquad (2.1)$$

where U_{DC} would be the static voltage applied to the endcaps, U_{RF} the radiofrequency voltage applied to the electrodes, r_0 is a scaling factor that is often taken as the distance between the trap center and the nearest electrode [98], $2z_0$ is the distance between the endcap electrodes, and κ is a geometrical factor which is determined

either from numerical solutions of the Laplace equation or experimentally [99]. Here the coordinate is already chosen such that x and y align with the principal axes of the pseudopotential. In the general case a rotation angle would have to be included ($x' =$ cos(α)x - sin(α)y), which leads to cross-terms xy after squaring. Due to the symmetry of such a trap it is usually sufficient to assume that only orthogonal harmonic terms contribute to the static potential

$$\Phi_{DC} = C_{2x}x^2 + C_{2y}y^2 + C_{2z}z^2. \tag{2.2}$$

The coefficients above can be extracted from a three-dimensional fit to numerically calculated potentials, and thus κ is given by:

$$\kappa = \frac{C_{2z}z_0^2}{U_{DC}} = \frac{-2C_{2x}z_0^2}{U_{DC}} = \frac{-2C_{2y}z_0^2}{U_{DC}} \tag{2.3}$$

and the electric field near the trap center is written as:

$$E = -\nabla\Phi = \begin{pmatrix} -\frac{V_{RF}}{r_0^2}\cos(\Omega_{RF}t)x + \frac{\kappa U_{DC}}{z_0^2}x \\ +\frac{V_{RF}}{r_0^2}\cos(\Omega_{RF}t)y + \frac{\kappa U_{DC}}{z_0^2}y \\ -2\frac{\kappa U_{DC}}{z_0^2}z \end{pmatrix}. \tag{2.4}$$

2.1.2 The Mathieu equations

From the electric field expression in eq. 2.4 the equations of motion for a single ion with mass m in a linear Paul trap can be derived. More specifically $F_i = m\ddot{r}_i = qE_i$, where r_i stands for the three directions. Thus, this is formulated as [100]

$$\ddot{r}_i + [a_i + 2q_i\cos(2\tau)]\, r_i = 0, \tag{2.5}$$

where $\tau \equiv \frac{\Omega_{RF}}{2}\tau$ and:

$$a_x = a_y = -\frac{1}{2}a_z = -\frac{\kappa 4qU_{DC}}{m\Omega_{RF}^2 z_0^2} \tag{2.6}$$

$$q_x = -q_y = \frac{2qV_{RF}}{m\Omega^2 r_0^2}, \quad q_z = 0 \tag{2.7}$$

In the z direction ions are confined in a harmonic well with frequency $\omega_z = \frac{\Omega_{RF}}{2}\sqrt{a_z}$. In the x and y directions Eq. 2.5 has the form of the standard Mathieu equation and the solutions are given by

$$r_j(\tau) = A_j e^{i\beta_j \tau} \sum_{n=-\infty}^{n=+\infty} C_{2n} e^{i2n\tau} + B_j e^{-i\beta_j \tau} \sum_{n=-\infty}^{n=+\infty} C_{2n} e^{-i2n\tau}, \; j \in \{x, y\} \tag{2.8}$$

The A_j and B_j constants depend on the initial conditions. Substituting Eq. 2.8 into Eq. 2.5 a recursion relation for C_{2n} can be obtained along with an expression for β_i [100]. Stable trapping conditions lie on the primary stability region of the $a_i - q_i$ space [100, 101]. When $|a_i|, \; |q_i| \ll 1$, the solution in Eq. 2.8 can be approximated by keeping only the C_{-2}, C_0 and C_{+2} coefficients. Thus, the values of β_i can be analytically calculated as

$$\beta_i \simeq \sqrt{a_i + \frac{q_i^2}{2}}, \tag{2.9}$$

and the solution of Eq. 2.5 is given by

$$r_i(t) \simeq r_{1i} \cos(\omega_i t + \phi_i)[1 + \frac{q_i}{2} \cos(\Omega_{RF} t)], \tag{2.10}$$

where ϕ_i depends on the initial conditions of the position and velocity of the ion. The first term is the harmonic oscillation of the ion with frequency ω_i and is called *secular* motion. The *secular* frequency can be expressed as

$$\omega_i \simeq \frac{\Omega_{RF}}{2} \beta_i. \tag{2.11}$$

The second term arises from the driven RF field of the trap and is referred to as *micromotion* of the ion. This intrinsic ion motion is unavoidable and if the ion is additionally subject to a static electric field then the solution in Eq. 2.10 becomes

$$r_i(t) \simeq r_{1i} \cos(\omega_i t + \phi_i)[1 + \frac{q_i}{2} \cos(\Omega_{RF} t)] + \frac{q E_{DC,i}}{m\omega_i^2} + \frac{\sqrt{2} E_{DC,i}}{m\omega_i \Omega_{RF}} \cos(\Omega_{RF} t) \tag{2.12}$$

where those two additional terms result from the displacement of the ion form the RF null line. The third term is an offset in ion position caused by $\mathbf{E}_{DC}$ and the fourth term is called *excess micromotion*. This cannot be compensated by laser cooling and the static fields that drive-off the ions from the RF null line must be suppressed, in

order to avoid adverse effects of excess micromotion, such as changes in the atomic transition line shape and second order Doppler-shift which influences dramatically the laser cooling rate [98]. The Eq. 2.5 can be expressed in a more general fashion as [102]

$$\ddot{x}_i + \sum_j A_{ij} x_j + 2 \sum_j Q_{ij} x_j \cos(2\tau) = 0 \tag{2.13}$$

where x_i are the ion coordinates in the three dimensions. The A and Q matrices represent the generalized multidimensional stability parameters [102, 103]

$$A_{ij} = \frac{4q}{m\Omega_{RF}^2} \left(\frac{\partial^2 \Phi_{DC}}{\partial x_i \partial x_j} \right), \tag{2.14}$$

$$Q_{ij} = \frac{2q}{m\Omega_{RF}^2} \left(\frac{\partial^2 \Phi_{RF}}{\partial x_i \partial x_j} \right). \tag{2.15}$$

If the trapping potential is perfectly harmonic then the A and Q matrices are traceless according to the Laplace equation. In order to determine the trapping frequencies the *pseudopotential* approximation is usually used. More specifically, the trapping frequencies are obtained form the eigenvalues of the Hessian matrix of the trapping potential,

$$H_{ij} = \begin{pmatrix} \frac{\partial^2}{\partial x^2} & \frac{\partial^2}{\partial x \partial y} & \frac{\partial^2}{\partial x \partial z} \\ \frac{\partial^2}{\partial y \partial x} & \frac{\partial^2}{\partial y^2} & \frac{\partial^2}{\partial y \partial z} \\ \frac{\partial^2}{\partial z \partial x} & \frac{\partial^2}{\partial z \partial y} & \frac{\partial^2}{\partial z^2} \end{pmatrix} \tag{2.16}$$

where the partial derivatives are evaluated in the trapping center. The harmonic oscillations occur along three orthogonal eigenvectors which define a basis along which the ion motion is independent from other directions. Thus, these eigenvalues and eigenvectors define the normal modes of oscillation of a trapped ion. When multiple particles exist or when anharmonic terms become relevant then the motion of each degree of freedom is coupled with the other directions [104]. In general, in the absence of static fields the transverse secular frequencies can be approximated by $\omega_x = \omega_y = q_x \Omega_{RF}/\sqrt{8}$ [105]. When $\omega_x \neq \omega_y$ then the degeneracy is broken.

2.1.3 Adiabatic approximation

For a particle with mass m and charge q under the influence of a trapping electric field $\mathbf{E} = \mathbf{E}_0(\mathbf{r})\cos(\Omega_{RF} t)$, we can make the assumption that the spatial variation of

this field is smooth such that the Taylor expansion of $\mathbf{E}_0(\mathbf{r})$ can be truncated after two terms such as

$$\mathbf{E}_0(\mathbf{r}(t)) = \mathbf{E}_0(\mathbf{r}_s(t)) - (r_0 \cdot \nabla)\mathbf{E}_0(\mathbf{r}_s(t)) \cos(\Omega_{RF} t). \tag{2.17}$$

Here, the ion coordinate $\mathbf{r}(t)$ is given by superimposing a smooth drift term $\mathbf{r}_s(t)$ and a fast oscillating term $\mathbf{r}_\mu(t)$:

$$\mathbf{r}(t) = \mathbf{r}_s(t) + \mathbf{r}_\mu(t) = \mathbf{r}_s(t) + \mathbf{r}_0 \cos(\Omega_{RF} t), \tag{2.18}$$

where $\mathbf{r}_0 = -q\mathbf{E}_0/m\Omega_{RF}^2$. By substituting Eq. 2.17 and 2.18 into the equation of motion of the ion $m\ddot{\mathbf{r}} = q\mathbf{E}$, one obtains

$$m\ddot{r}_s - m\Omega_{RF}^2 \mathbf{r}_0 \cos(\Omega_{RF} t) = q\mathbf{E}_0(\mathbf{r}_s)\cos(\Omega_{RF} t) - q(\mathbf{r}_0 \cdot \nabla)\mathbf{E}_0(\mathbf{r}_s)\cos^2(\Omega_{RF} t). \tag{2.19}$$

This expression is simplified using the vector analysis identity $(\mathbf{E}_0 \cdot \nabla)\mathbf{E}_0 = \frac{1}{2}\nabla \mathbf{E}_0^2 \times (\nabla \times \mathbf{E}_0)$, and because $\nabla \times \mathbf{E}_0 = 0$ the time-averaged form of 2.19 can be written as

$$\langle m\ddot{\mathbf{r}}_s \rangle_t = \langle q^2 \frac{1}{2} \nabla \mathbf{E}_0^2 \cos^2(\Omega_{RF} t) \rangle_t \tag{2.20}$$

$$m\ddot{\mathbf{r}}_s = -\frac{q^2}{4m\Omega_{RF}^2} \nabla \mathbf{E}_0^2. \tag{2.21}$$

The right-hand side of Eq. 2.21 represents the negative gradient of a time-independent potential and is called *pseudopotential*. For clarity this can be expressed as

$$\phi_{ps} = \frac{q^2}{4m\Omega_{RF}^2} \mathbf{E}_o^2. \tag{2.22}$$

This result is obtained based on two assumptions. First, $\mathbf{r}_s(t)$ changes slowly on the time scale of $2\pi/\Omega_{RF}$, i.e. $\ddot{\mathbf{r}}_s \ll \Omega_{RF}\dot{\mathbf{r}}_s$. The second is that $\mathbf{E}_0(\mathbf{r}_z(t))$ is approximately constant over one cycle of the RF oscillation, that is $\dot{\mathbf{r}} \ll \Omega_{RF}\mathbf{r}_0$. These two assumptions together are referred to as the *adiabatic approximation*. Behaving adiabatically

typically requires a high RF frequency and other changes in time to be slow. This is quantified using a dimensionless ratio called the *adiabacity parameter*

$$\eta = \frac{\|2(\mathbf{r}_0 \cdot \nabla)\mathbf{E}_0(\mathbf{r}_s)\|}{\|\mathbf{E}_0(\mathbf{r}_s)\|} \tag{2.23}$$

which simplifies to

$$\eta = \frac{2q\|\nabla\mathbf{E}_0(\mathbf{r}_s)\|}{m\Omega_{RF}^2}. \tag{2.24}$$

The validity of the adiabatic approximation relies on small values of $\eta < 0.3$ [106]. This ensures that the spatial variation of the inhomogeneous electric field is smooth such that the change of the field is much smaller than the field itself. The total energy of ions within this approximation is a constant of a motion, and is formulated as

$$E = \frac{1}{2}m\dot{\mathbf{r}}_s^2 + \frac{q^2}{4m\Omega_{RF}^2}\|\nabla\Phi_{RF}\|^2 + q\Phi_{DC}. \tag{2.25}$$

The first term is the kinetic energy of the slow motion and is called *secular* kinetic energy. The second and the third term together form the total effective trapping potential Φ_{tot} experienced by the ions as the sum of a time-independent *pseudopotential* Φ_{ps} and a static potential Φ_{DC}

$$\Phi_t(x,y,z) = \Phi_{ps} + \Phi_{DC} = \frac{q^2}{4m\Omega_{RF}^2}\|\nabla\Phi_{RF}\|^2 + q\Phi_{DC}. \tag{2.26}$$

The pseudopotential represents the kinetic energy of the micromotion of the ion, and the position and kinetic energy of the ion due to micromotion can be written as

$$\mathbf{r}_\mu(t) = -\frac{q}{m\Omega_{RF}^2}\mathbf{E}_0\cos(\Omega_{RF}t), \tag{2.27}$$

$$E_{\mu,kin} = \frac{q^2}{2m\Omega_{RF}^2}|\mathbf{E}_0|^2\sin^2(\Omega_{RF}t). \tag{2.28}$$

The trap depth is calculated within the adiabatic approximation and is defined as the difference between the pseudopotential minimum at the RF null line and its local maxima. The effective or total trap depth is defined as the difference between the minimum of the total trapping potential (Eq. 2.26) and the saddle points, where the ions can escape from the trap in the presence of a static potential.

2.2 Laser Cooling

Doppler laser cooling is a technique that has been established in atomic physics over the last three decades [107, 108]. More specifically, absorption of light leads to the transfer of momentum from the radiation field to the particles. If the atoms decay via spontaneous emission, the associated recoil is in random direction, and thus, over many scattering events is averaged out. Photons of the laser beam, which is slightly red-detuned from the atomic resonance, are preferentially absorbed from the atoms that are moving anti-parallel to the k-vector of the incident laser beam and better compensate the frequency mismatch according to the Doppler shift. For a detailed and educational explanation of Doppler laser cooling scheme please refer to [97].

2.2.1 The Calcium Ion

The $^{40}Ca^{+}$ ion is widely used in trapped ion experiments and was chosen as the species for the experiment in this work. It has many attractive properties not only for the trapping and cooling processes, but also for acting as a qubit. It has no nuclear spin, which reduces the number of energy levels, since there is no hyperfine structure. The $^{40}Ca^{+}$ electronic structure is shown in Fig. 2.1. It has two possible choices for a pseudospin/qubit transition. The first one is a Raman transition connecting the two $^{2}S_{1/2}$ Zeeman states [109]. The second is the optical qubit in the quadrupole transition connecting the $^{2}S_{1/2}$ to the $^{2}D_{5/2}$ levels, which is usually the choice for many quantum information and high precision quantum experiments. For Doppler cooling and fluorescence detection it features the dipole transition $^{2}S_{1/2}$ to $^{2}P_{1/2}$ which is driven with a laser at 397 nm and a repumper at 866 nm, recycling the population decaying from the $^{2}P_{1/2}$ to the $^{2}D_{3/2}$ state. Another attractive feature of the $^{40}Ca^{+}$ are the comparably easily obtainable wavelegths, which are used to manipulate the ion. Nowadays, all of those wavelengths are accessible using commercially available diode lasers, including the wavelegths to photo-ionize the neutral Ca atom. Nevertheless, the absence of a hyperfine structure is a drawback for high fidelity experiments as no magnetic field independent transition exist [19]. This raises challenges for innovative experimental techniques in order to reduce the magnetic field noise.

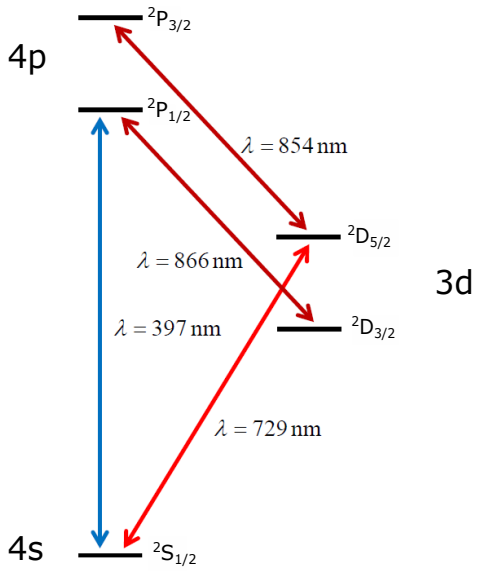

Figure 2.1: The energy level scheme of $^{40}Ca^+$ representing the Doppler cooling laser, the repumpers and the qubit transition.

2.3 Numerical Methods for the Electrodes Basis Functions

For complex trapping architectures the basis functions of the electrodes must be calculated numerically. For layer trap geometries, especially, it is necessary to calculated the electric fields numerically using the FEM (Finite Elements Method) of the BEM (Boundary Elements Method), as opposed to the planar chip geometries, where analytical models can provide an accurate description [102, 110, 111].

FEM is a well-established and powerful technique for the electric potential of a specific arrangement of electrodes. Under the frame of this method, discretisation of the entire boundary-value-problem domain into "mesh" elements is applied. The vertices of these elements are related to each other by a simple linear or quadratic function. The potential is calculated at the vertices following specific algorithms while the boundary conditions are satisfied. These algorithms can be divided in two broad categories: the direct and iterative solvers. During such calculations the convergence of the results needs to be checked and usually can be verified following some conditions.

As a first rule of thumb, the solutions must be independent of the size, the distribution and the shape of the mesh elements that are chosen. To reduce discretisation error, one has to reduce the size of the mesh. Nevertheless, reducing the mesh size

leads to considerable increase in computational time. Consequently, one has to try various mesh sizes in order to find a compromise between accuracy and computational time. Taking advantage of the symmetry and strategic meshing one can achieve desirable results with efficient computational load. More specifically, in this work there were used different regions of interest with different mesh size. For instance, the mesh size was considerably smaller in the trapping region compared to the rest of the geometry, and an additional finer mesh region was implemented inside the trapping region, which was enclosing the nanowire and the holder. The big size mismatch from the millimeters size region of the global boundaries down to the nanometers size of the nano-objects was challenging during the meshing process. The elements that were chosen for the mesh were free-tetrahedrals. Tetrahedrals and triangular mesh elements are recommended for curved and complex geometries, because of the increased number of vertices for convergence solutions.

Secondly, the solutions must be independent of the auxiliary boundary conditions applied to the model. The boundary domain resembling the vacuum chamber walls and surfaces surrounding a given trap are typically implemented with smaller objects for reasonable computational times. Thus, the variation of solutions, due to this size mismatch compared to the actual objects, needs to be reasonably small.

Lastly, the solutions must be independent of the algorithms employed. For example, the solutions provided by the direct algorithms are independent of the algorithm, but this is not the case for the iterative solvers.

The advantages of the FEM calculations are manifold. It is used in a variety of problems in different fields, like electrostatic, hydrodynamics, mechanical properties of solid-state systems, as well as for thermal dissipation. Furthermore, FEMs enable simultaneous modelling of combinations of different effects, when a combined system is under consideration. In addition, complex geometries and effects from non-linear material properties can, also, be simulated. The software package that offers all of those possibilities and was used in this work is COMSOL[1].

An alternative technique for this type of calculations is the BEM, where integral equation formulations are used instead of the differential equations in FEM. For the the case of a trap geometry, the surface of the electrodes are discretised with mesh

[1]COMSOL, MultiPhysics, www.comsol.com

elements and the charge density of each element on the surface is found. The solution at a given point in the problem domain is computed by evaluating the integrals representing the contribution of the potential at this point from each charge element on the surface. BEM offers two advantages: first, the potentials obtained are continuous functions, because the discretisation occurs on the boundary surfaces. Second, they offer considerable improvement in the computational efficiency, owed to the reduction of the dimensionality from a volume in FEM to a surface in BEM. Softwares that implements BEM calculations are *BEMsolver* [112] or the commercially available package *CPO*[2].

2.4 Molecular Dynamics Simulations

Molecular dynamics (MD) simulations [113, 114] have been extensively used for the theoretical understanding of Coulomb crystals or trapped ions in general in Paul or Penning traps [112, 115–119]. Here, we discuss the techniques that have been adapted and implemented for the dynamic description of the ion-nanowire hybrid system of this work. The objects have been implemented in ProtoMol MD framework [120].

Under this framework, the classical equations of motion for the laser-cooled ion and the effect of the nanowire have been solved as:

$$m\ddot{\mathbf{r}} = \mathbf{F}_{trap} + \mathbf{F}_{heating} + \mathbf{F}_{LC} + \mathbf{F}_{nw}, \tag{2.29}$$

where, m and $\mathbf{r}$ are the mass and position of the ion respectively. The rest of the terms are contributions to the total force, and more specifically, $\mathbf{F}_{trap}$ is the trapping force, $\mathbf{F}_{heating}$ is the heating force that induces dissipation and decoherence on the ion, $\mathbf{F}_{LC}$ is the laser cooling force and $\mathbf{F}_{nw}$ is the force that was implemented in order to describe the nanowire effect on the ion motion.

In this approach, the heating force simulates the heating effects that arise in a trap, due to collisions with background gas molecules or imperfections of the trapping

[2]Charged Particle Optics, Electronoptics, http://www.electronoptics.com

setup. Those heating effects were modelled as random momentum kicks on the ion. The Doppler laser cooling force was modelled as a friction force [107]:

$$\mathbf{F}_{LC} = \mathbf{F}_{RP} - \beta \mathbf{v}. \tag{2.30}$$

We see that the laser cooling force consists of one velocity independent term, which represents the radiation pressure and a velocity dependent term. The semi-empirical β parameter in the velocity dependent term was determined from typical experimental parameters and has the form:

$$\beta = -\hbar k^2 \frac{4 s_0 (\delta/\gamma)}{\left(1 + s_0 + (2\delta/\gamma)^2\right)^2}. \tag{2.31}$$

Here, γ is the natural linewidth of the atomic transition, δ is the detuning from the atomic resonance, k is the wavevector of the laser beam, s_0 is the saturation parameter which is related to the Rabi frequency and is defined as $2|\Omega|^2/\gamma^2$. This approximation of the laser-cooling force has been frequently used in the past and successfully described the dynamics that arise from the laser-ion interaction [112, 115, 117].

The trapping force is the one that defines predominantly the ion motion inside the trapping region and depends strongly on the geometrical and operational parameters of the corresponding trap. In the case of linear Paul traps the trapping force is straightforward and is given from the analytical expressions of the gradients of the RF and static potentials. Nevertheless, in order to simulate properly the trapping force for a layer trap some considerations need to be taken into account and specific approaches to be followed.

In the first approach one can derive the A and Q matrices from the FEM calculations, as shown in Eqns. 2.14 and 2.15 and implement the trapping force inside the MD framework as:

$$\mathbf{F}_{trap}(x, y, z, t) = \frac{m\Omega_{RF}^2}{4} \sum_{i=x,y,z} \left(A_{ii} + 2Q_{ii}\cos(\Omega_{RF} t)\right) \mathbf{x}_i. \tag{2.32}$$

This method assumes that the RF and static trapping potentials near the center of the trap are fully described by second-order terms and it neglects the higher order ones.

The second approach, is to use analytic expressions of the trapping potentials into the MD simulations. However, this is not trivial for a segmented layer linear trap, as the one fabricated in this work, and this approach was abandoned.

The third approach, takes advantage of the results from the FEM calculations. Here, the electrode basis functions that are obtained from the FEM calculations, are fitted to a three-dimensional power series expansion for both the static and RF potentials near the trap center. This approach was also used in this work, and the expansion of the trapping potential was implemented inside the MD framework as:

$$\begin{aligned}\mathbf{F}_{trap}(x,y,z,t) = -\nabla\Bigg(&V_{RF}\cos(\Omega t)\sum_{k,l,m} C_{RF_{(k,l,m)}}(x-x_0)^k(y-y_0)^l(z-z_0)^m \\ &+\sum_{i=1}^{n} V_i \sum_{k,l,m} C_{DC,i_{k,l,m}}(x-x_0)^k(y-y_0)^l(z-z_0)^m\Bigg).\end{aligned} \tag{2.33}$$

The coefficients $C_{RF_{(k,l,m)}}$ and $C_{DC,i_{k,l,m}}$ correspond to the (k,l,m)-th order term of the RF and DC electrode potential. In the simulations of the miniaturized layer trap in this work these coefficients were obtained from 4-th order polynomial fits in a 500 μm cube around the trap center.

The pseudopotential approximation can adequately describe the ion dynamics inside the trap [112, 121]. However, due to the assumptions made and the simplified laser-cooling model used, one cannot describe properly the thermalization of the trapped ions after each collision with background molecules as stated in a recent study [119, 122].

2.5 Nanomechanics

2.5.1 Motion of a Resonator

The motion of a mechanical resonator under an external load is described by the Euler-Bernoulli theory [123]. This theory describes the small deflections of a beam that is subject to lateral loads and it can describe almost accurately beams with cross-

sections orders of magnitudes smaller than their length [3]. This is the case for the nano-sized resonators that have been widely used over the last few decades in various experimental setups, because of the benefits provided by their low spring constant and high quality factor.

Within the Euler-Bernoulli theory the three-dimensional motion of a resonator can be described by the displacement function $\mathbf{U}_m(\mathbf{r}, t)$ which accounts for an infinite number of independent vibrational modes. Indicating each mode with the index n and separating the spatial degrees of freedom with the time dependence the displacement function reads:

$$\mathbf{U}(\mathbf{r}, t) = \sum_n x_n(t)\mathbf{u}_n(\mathbf{r}), \tag{2.34}$$

where $\mathbf{u}_n(\mathbf{r})$ is the mode-shape of the n-th mode and $x_n(t)$ describes the time dependence of the motion.

In the case of high-quality factor resonators, the function $x_n(t)$ can be determined by approximating each of the independent vibrational modes as a damped harmonic oscillator [2, 3], with the following equation of motion:

$$m_n\ddot{x}_n + \Gamma_n\dot{x}_n + k_n x = 0. \tag{2.35}$$

Here, m_n is the effective mass, Γ_n is the intrinsic dissipation and k_n is the spring constant for the n-th mode of the resonator. The dissipation and the spring constant can be written in terms of the effective mass, angular resonance frequency ω_n and the quality factor Q_n according to

$$\Gamma_n = \frac{m_n\omega_n}{Q_n} \quad \text{and} \quad k_n = m_n\omega_n^2. \tag{2.36}$$

Detailed definition of the effective mass of the resonator is given further below in the thesis.

2.5.2 Theory of Beams

Many nanomechanical resonators have beam-like geometries and their motion can be described by the reduction of Eq.2.34 into the displacement function of the one-dimensional case:

$$U(z,t) = \sum_n x_n(t) u_n(z), \tag{2.37}$$

where the $u_n(z)$ represents the motion along the z-direction.

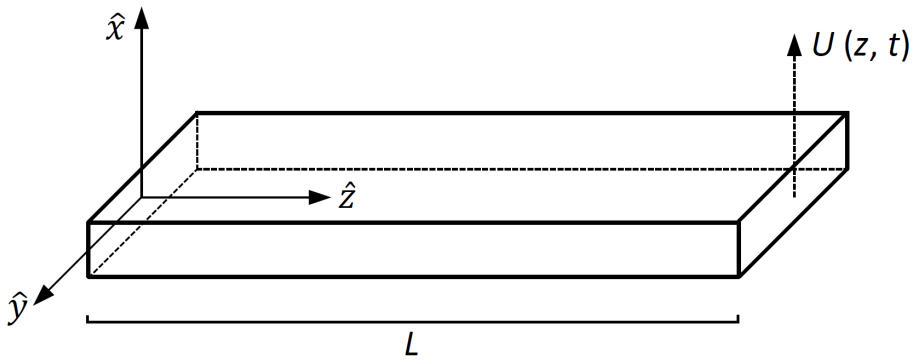

Figure 2.2: Representation of a beam of length L with orientation along the z direction that oscillates along the x direction. The beam cross-section is uniform throughout the length, and the size and displacement amplitude are much smaller than its length.

The equation of motion for a long thin beam of uniform cross-section, as shown in Fig. 2.2 with x being the direction of oscillation reads:

$$E_Y I_y \frac{\partial^4 U}{\partial z^4} + \rho A \frac{\partial^2 U}{\partial t^2} = 0. \tag{2.38}$$

Here E_Y is the Young's modulus of the material, I_y is the polar moment of inertia about y-direction, ρ is the mass density, and A is the cross-sectional area of the beam. According to Eq.2.37, Eq.2.38 can be solved separately for each of the resonator n modes. For the moment neglecting the dampening term $\Gamma_n \ddot{x}$ from Eq.2.35 and letting $x_n(t)$ assume and oscillatory behaviour like:

$$x_n(t) = x_{osc,n} e^{-i\omega_n t}, \tag{2.39}$$

where $x_{osc,n}$ is the oscillation amplitude, then the n-th mode shape function of the resonator must satisfy:

$$\frac{d^4 u_n}{dz^4} - \frac{\beta_n^4}{L^4} u_n = 0, \tag{2.40}$$

where $\beta_n = L((\rho A \omega_n^2)/(E_Y I_y))^{1/4}$ is a dimensionless parameter. The general solution of this differential equation is:

$$u_n(z) = A_n \sin\frac{\beta_n}{L}z + B_n \cos\frac{\beta_n}{L}z + C_n \sinh\frac{\beta_n}{L}z + D_n \cosh\frac{\beta_n}{L}z. \tag{2.41}$$

The values of the mode-dependent parameters β_n, A_n, B_n, C_n and D_n are determined (up to a normalization constant) by setting the boundary conditions for a specific physical system. Together with the determination of the mode shape of each of the beam n modes, it is also possible to calculate the corresponding eigenfrequency, using the relation

$$\omega_n = \frac{\beta_n^2}{L^2}\sqrt{\frac{E_Y I_y}{\rho A}}. \tag{2.42}$$

Mode	β_n	ω_n/ω_0
0	1.875	1.000
1	4.694	6.267
2	7.855	17.547
3	10.996	34.386
n $\geq$ 3	(n+1/2)π	$[(n+1/2)\pi/\beta_0]^2$

Table 2.1: Mechanical parameters of a cantilever. The values of β_n and of the normalized eigenfrequencies are shown for the first four mode shapes, along with the asymptotic values for $n \geq 3$. The values can be found in Refs. [2–4].

2.5.3 Cantilever

A single clamped beam on one end that can freely move on the other is called a cantilever and is subject to the boundary conditions:

$$u_n(0) = \frac{du_n}{dz}(0) = \frac{d^2u_n}{dz^2}(L) = \frac{d^3u_n}{dz^3}(L) = 0. \tag{2.43}$$

Inserting these conditions in Eq. 2.41 we find that β_n must obey the equation:

$$\cos(\beta_n)\cosh(\beta_n) + 1 = 0, \tag{2.44}$$

with solutions as shown in Table 2.1. The mode shape of the cantilever then can be expressed as:

$$u_n(z) = \frac{1}{K_n}\left[S_n\left(\cosh\frac{\beta_n}{L}z - \cos\frac{\beta_n}{L}z\right) - T_n\left(\sinh\frac{\beta_n}{L}z - \sin\frac{\beta_n}{L}z\right)\right], \qquad (2.45)$$

where $K_n = 2[\sin(\beta_n)\cos(\beta_n) - \cos(\beta_n)\sinh(\beta_n)]$, $S_n = \sinh(\beta_n) + \sin(\beta_n)$, and $T_n = \cosh(\beta_n)+\cos(\beta_n)$. The constants have been chosen in order to fulfill the normalization condition that the maximum value of $|u_n(z)|$ is unity. The lowest four normalized mode shape functions of a cantilever are shown in Fig. 2.3.

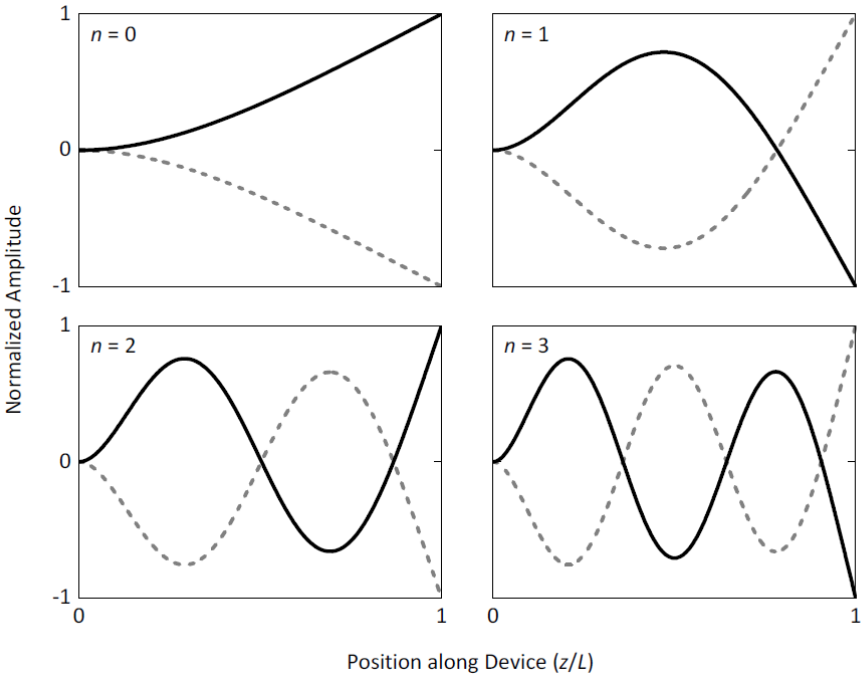

Figure 2.3: The first four mode shape functions of a cantilever are shown according to the normalized function $u_n(z)$. The corresponding eigenfrequencies are given in Table 2.1.

So far the analysis of the cantilevers was independent of the specific shape of the cross-section, maintaining the model general assumptions that the cantilever needs to be thin and uniform throughout the length. However, different cross-section geametrical shapes lead to different cantilever eigenfrequencies. The most discussed one in textbooks is the rectangular cross-section beam of width w and thickness d. Such a geometry is characterized by polar moments of inertia $I_y = wd^3/12$ and $I_x = dw^3/12$,

that correspond respectively to the flexural vibrations along the x and y directions. The associated eigenfrequencies are:

$$\omega_{n,x} = \beta_n^2 \sqrt{\frac{E_Y}{12\rho}} \frac{d}{L^2}, \tag{2.46}$$

$$\omega_{n,y} = \beta_n^2 \sqrt{\frac{E_Y}{12\rho}} \frac{w}{L^2}. \tag{2.47}$$

Thus, the eigenfrequencies are linearly dependent on the cross-section dimensions and inversely proportional to the square of the length. That is, for a squared cross-section beam each mode is doubly degenerate ($w = d$). The considerations are valid for any other regular polygonal cross-section centered around the cantilever axis. This includes the case of a cylindrical beam, which is the most relevant case for this work, where cylindrical cross-section nanowires were used. More specifically, for a cylindrical beam of diameter D, for which $I_x = I_y = \pi D^2/64$ the eigenfrequencies are expressed as:

$$\omega_n = \beta_n^2 \sqrt{\frac{E_Y}{16\rho}} \frac{D}{L^2}. \tag{2.48}$$

Lastly, for the sake of completeness, for the case of a cantilever with hexagonal cross-section of side s, for which $I_x = I_y = 5\sqrt{3}s^4/16$ the eigenfrequencies are:

$$\omega_n = \beta_n^2 \sqrt{\frac{5E_Y}{24\rho}} \frac{s}{L^2}. \tag{2.49}$$

2.5.4 Effective Mass of a Cantilever

The application of external load to a mechanical resonator entails a displacement following a characteristic mode shape. As we have seen in the previous section, the mode shape depends on the mechanical and geometrical properties of the resonator and is in general a non-linear function of position. This means that a volume element in the resonator reacts to the load with an inertia which depends on its specific position. For example, the volume elements that are located closer to the clamped end react as if the local mass would be higher than the mass around the free-end position. In order to account for this position-dependent inertia when studying the mechanical energy of a resonator it is useful to introduce the concept of *effective mass*.

For a generic mechanical resonator the potential energy $\mathrm{d}U_{pot}$ for a volume element $\mathrm{d}V$ can be written according to Hooke's law as:

$$dU_{pot} = \frac{1}{2}\rho(\mathbf{r})\omega_n^2 \left|x_n(t)\mathbf{u}_n(\mathbf{r})\right|^2 dV. \tag{2.50}$$

The total elastic energy associated with the n-th mode is then given by integrating dU_{pot} over the entire volume of the resonator V which gives:

$$\begin{aligned} U_{pot} &= \frac{1}{2}\omega_n^2 \left|x_n(t)\right|^2 \int_V \rho(\mathbf{r}) \left|\mathbf{u}_n(\mathbf{r})\right|^2 dV \\ &= \frac{1}{2}\omega_n^2 \left|x_n(t)\right|^2 \left|\mathbf{u}_n(\mathbf{r}_0)\right|^2 m_n(\mathbf{r}_0). \end{aligned} \tag{2.51}$$

The last equation contains the expression of the effective mass of a mechanical resonator at position $\mathbf{r}_0$ [4]:

$$m_n(\mathbf{r}_0) \equiv \frac{\int_V \rho(\mathbf{r}) \left|\mathbf{u}_n(\mathbf{r})\right|^2 dV}{\left|\mathbf{u}_n(\mathbf{r}_0)\right|^2}. \tag{2.52}$$

Thus, according to this definition the effective mass for a given mode is proportional to the volume of the mode squared inside the resonator. Because of the normalization condition, $|\mathbf{u}_n(\mathbf{r}_0)| \leq 1$, when measuring the motion of the resonator at some position $\mathbf{r}_0$ other than the one of maximum displacement, one has to take into account that the effective mass has increased. The general definition in Eq. 2.52 can be simplified in the case of a resonator with uniform density. As mentioned previously, the motion of a resonator can be considered as a superposition of one-dimensional displacements. Using the initial assumption of resonators with uniform cross-section the expression of the effective mass becomes:

$$m_n(z_0) = \frac{\rho A}{\left|u_n(z_0)\right|^2} \int_V \left|u_n(z)\right|^2 dz. \tag{2.53}$$

The last two definition, Eq. 2.52 and 2.53, depend on the mode shape of the resonator. Specifically, this last expression has been obtained without making any assumption on the specific geometry of the resonator cross-section. Therefore, maintaining the model's general assumptions of a beam with thin, uniform cross-section, the calculation of the effective mass is valid for a cross-section of any shape.

A very useful parameter in nanomechanics is the effective mass ratio, defined as the effective mass of a given resonator m_n at the position of maximum displacement over the total mass M. The effective mass is an intrinsic quantity of mechanical resonators and is independent of their size and material.

In this work, we chose a cantilever, whose maximum displacement is at its free-end. Combining the definition of the effective mass Eq. 2.53 and the expression Eq. 2.45 it follows that $z_0 = L$ and the effective mass ratio of a cantilever reads

$$\frac{m_n}{M} = \frac{1}{L}\int_0^L |u_n(z)|^2 \, dz = \frac{1}{4}. \tag{2.54}$$

This result tells us that the effective mass of a cantilever is constant and equal to 1/4 of its total mass, independently of the mode. According to this expression we used the effective mass value in the theoretical calculations presented in Chapter 4.

2.5.5 Thermal Noise

Nanoresonators are not isolated systems, and apart from externally applied forces, they interact with the environment with a mutual transfer of energy. For instance, they experience collisions with the molecules of the environment, the phonons of their substrate or support are coupled to the resonators via clamping points, the motion of charged defects or ions on the surface of the resonator is another source of interaction and so on. All these aforementioned coupling processes are random and irreversible and they lead to energy dissipation and to fluctuations in the resonator vibrations, which is what is called *Brownian motion*. Thus, the force exerted by the environment on the resonator can be separated into a *dissipation* term, proportional to the resonator's velocity, and a term due to random force F_{th} which is the *thermal noise*. The dynamics of the resonator can therefore be described by the *Langevin equation*:

$$m\ddot{x} + \Gamma\dot{x} + kx = F_{th}. \tag{2.55}$$

This equation describes the motion of one resonator mode, but the same analysis can be extended to other modes.

Displacement Spectral Density

The noisy time-dependent quantity of the resonator displacement can be expressed in terms of the *Spectral density* (or power spectrum), which expresses the intensity of the noise at a given frequency [124]. Defining its Fourier transform over a finite window we have:

$$\hat{x}_\tau(\omega) \equiv \frac{1}{\sqrt{\tau}} \int_{-\tau/2}^{\tau/2} x(t) e^{i\omega t} dt, \tag{2.56}$$

where τ is the sampling time. The definition of spectral density of $x(t)$ is then [124]:

$$\bar{S}_x(\omega) \equiv \lim_{\tau \to \infty} \langle |\hat{x}_\tau(\omega)|^2 \rangle. \tag{2.57}$$

If the last relation is inverted, then the signal fluctuation can be expressed as a function of the spectral density. That can be done by introducing the autocorrelation function $K_x(t)$, which describes how $x(t')$ is related to itself at a later time $t' + t$ [4]:

$$K_x(t) \equiv \lim_{\tau \to \infty} \frac{1}{\tau} \int_0^\tau x(t') x(t' + t) dt'. \tag{2.58}$$

The spectral density is then related to $K_x(t)$ via the Fourier transform [2–4, 124]:

$$\bar{S}_x(\omega) = \int_{-\infty}^{+\infty} K_x(t) e^{i\omega t} dt. \tag{2.59}$$

We see then that the spectral density spans both positive and negative frequencies. However, in physical situations we have real-valued signals and $\bar{S}_x(\omega)$ is an even function [124], thus the spectral density for the single-sided spectra is expressed as:

$$S_x(\omega) \equiv \bar{S}_x(\omega) + \bar{S}_x(-\omega). \tag{2.60}$$

This definition still allows the conservation of the total power of the signal when $S(\omega)$ is integrated over only positive frequencies. Also, the fluctuation of the signal $x(t)$ is connected to the autocorrelation function $K_x(t)$ provided that the sampling time is sufficiently long (i.e. $\tau \gg 2\pi/\omega_0$, where ω_0 is the angular frequency):

$$\langle x^2 \rangle \equiv \frac{1}{\tau} \int_0^\tau [x(t)]^2 \, dt = K_x(0). \tag{2.61}$$

Therefore from the inverse Fourier transform of Eq. 2.59 we get:

$$\langle x^2 \rangle = \frac{1}{2\pi} \int_0^\infty S_x(\omega) d\omega. \tag{2.62}$$

According to this equation there is a direct connection between the root-mean-squared thermal motion x_{rms} and its spectral density:

$$x_{rms} = \frac{x_{osc}}{\sqrt{2}} = \sqrt{\frac{1}{2\pi} \int_0^\infty S_x(\omega) d\omega}. \tag{2.63}$$

An analytical expression of $S_x(\omega)$ can be derived after the Fourier transform of both sides of Eq. 2.55 which provides the frequency response of the resonator:

$$\hat{x}(\omega) = \frac{1/m}{\omega_0^2 - \omega^2 + i\omega_0\omega/Q} \hat{F}_{th}(\omega), \tag{2.64}$$

where the dissipation Γ was replaced with the *quality factor* $Q = m\omega_0/\Gamma$. The random nature of the thermal force implies that on a long time scale F_{th} is uncorrelated with the displacement $x(t)$. Using the definition of Eq. 2.57 the displacement spectral density can be determined as [2, 4, 125]:

$$S_x(\omega) = \frac{1/m^2}{(\omega_0^2 - \omega^2)^2 + \omega_0^2\omega^2/Q^2} S_{F_{th}}, \tag{2.65}$$

where $S_{F_{th}}$ is the spectral density of the thermal noise force, and is considered white in the bandwidth of the resonator. Then $S_{F_{th}}$ is connected to the fluctuations of Brownian motion by solving the integral of Eq. 2.62:

$$\langle x^2 \rangle = \frac{Q}{4\omega_0^3 m^2} S_{F_{th}}. \tag{2.66}$$

In equilibrium the temperature of the resonator is equal to the environmental temperature T. The equipartition theorem establishes a connection between the potential and kinetic energy of the resonator with the equilibrium temperature:

$$\frac{1}{2} k \langle x^2 \rangle = \frac{1}{2} m \langle \dot{x}^2 \rangle = \frac{1}{2} k_B T, \tag{2.67}$$

whre k_B is the Boltzmann's constant. Combining this relation with Eq. 2.66 the thermal force spectral density can be expressed as:

$$S_{F_{th}} = \frac{4k_B T\omega_0 m}{Q} = 4k_B T\Gamma. \tag{2.68}$$

This result is known as the *fluctuation-dissipation theorem* and is valid in general for systems that are governed by a *Langevin equation* [3]. This shows that the thermal force spectral density can be expressed in terms of the intrinsic properties of the resonator and the environmental temperature, ignoring the microscopic origin of the force. Furthermore, it highlights that the force noise determines the quality factor (or conversely the dissipation) of the resonator [2].

Combining the result of Eq. 2.68 into Eq. 2.65 the spectral density of the resonator thermal noise is expressed as:

$$S_x(\omega) = \frac{4k_B T\omega_0}{mQ\left[(\omega_0^2 - \omega^2)^2 + \omega_0^2\omega^2/Q^2\right]}, \tag{2.69}$$

or in terms of the spring constant $k = m\omega^2$:

$$S_x(\omega) = \frac{4k_B T\omega_0^3}{kQ\left[(\omega_0^2 - \omega^2)^2 + \omega_0^2\omega^2/Q^2\right]}. \tag{2.70}$$

Experimentally, the motion of the resonator is transduced by the measurement apparatus into a time-varying electrical signal. This signal is transformed into the frequency domain by the means of a spectrum analyzer, and providing in this fashion the spectral representation of the resonator motion. The response of the spectrum analyzer is typically the one-sided spectral density $S_x(\omega)$, combined with other measurement noise sources. Assuming this noise to be white and uncorrelated to the displacement of the resonator, the two signals add to each other in quadrature, giving a measured voltage spectral density of the form:

$$S_V(\omega) = \alpha^2\left[S_{x_n} + S_x(\omega)\right]. \tag{2.71}$$

Here S_{x_n} represents a constant offset due to the white measurement noise and α is a coupling coefficient which accounts for the transduction of the resonator motion into a voltage signal. A typical experimental displacement spectrum of the fundamental

mode of a nanomechanical resonator is shown in Fig. 2.4 [1]. The function $S_V(\omega)$ can be fit directly to physical data for the extraction of the mechanical properties of the resonator. The *sensitivity* of the detector is given by $\sqrt{S_{x_n}}$ and is expressed in units of $m/\sqrt{Hz}$, which shows that the sensitivity does not depend on the bandwidth of a specific measurement nor on the wait time. Longer measurements average out the white noise, leading to a reduction of the displacement uncertainty: this bandwidth-dependent parameter is usually referred to as the *resolution* of the detector [2]. The signal-to-noise (SNR) ratio is given by the height of the resonance peak divided by the height of the noise floor (i.e. the sensitivity squared). As shown in Fig. 2.4 in order to obtain a large SNR it is advantageous to have a resonator with high Q and low k.

Out of equilibrium the fluctuation-dissipation theorem no longer holds and the temperature of the resonator might be different from the one of the environment. It is then necessary to define an effective temperature of the resonator as:

$$T_{eff} \equiv \frac{k\langle x^2 \rangle}{k_B} = \frac{k}{2\pi k_B} \int_0^\infty S_x(\omega) d\omega, \tag{2.72}$$

which makes apparent that the effective temperature of the resonator is proportional to the are under the spectral density, or in terms of experimental data, to the area between $S_V(\omega)/\alpha^2$ and the noise floor S_{x_n} as shown in Fig. 2.4. In equilibrium $T_{eff} = T$ is still valid. However, the force noise can be larger or smaller than the equilibrium value expressed in Eq. 2.68 leading to an effective heating or cooling of the resonator. In this way the cantilever's fundamental mode can be cooled below the bath temperature by means of an applied feedback force.

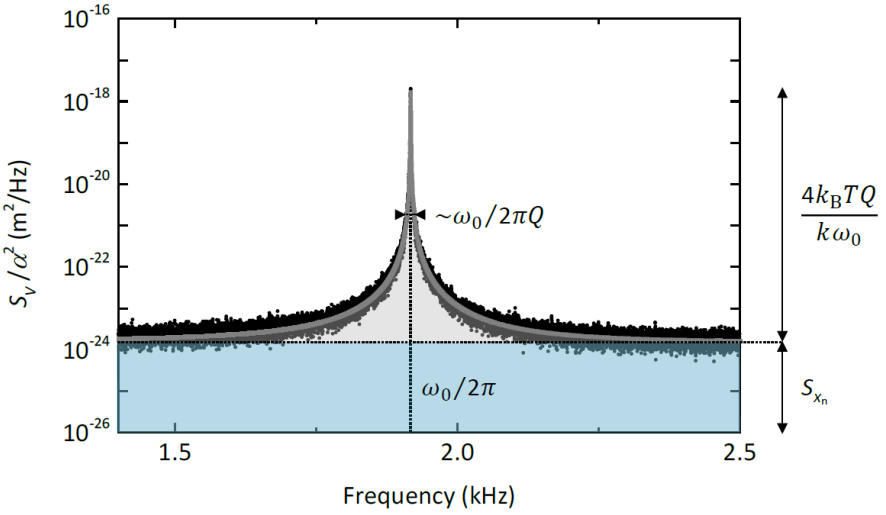

Figure 2.4: The image is taken from [1]. It shows in black dots the thermal spectrum of the fundamental mode of an ultra-soft Si cantilever, at $T = 4.2$ K, $p < 10^{-6}$ mbar with $Q_0 = 10^4$. The grey area between the fit and the noise floor S_{x_n} is proportional to the effective temperature of the resonator.

Chapter 3

Experimental Setup

This chapter describes the experimental apparatus that was built as part of this project, in order to combine the cold ion technology with the nanomechanical setup, towards the implementation of the hybrid system device. The simulation and fabrication of the miniaturized wafer trap, the vacuum chamber along with the individual components, the radiofrequency (RF) resonator that supplied the radiofrequency drive of the trap and the imaging and laser setup for the ultracold ion are described in details. Moreover, it is described the mechanical, electrical and optical components of the nanomehcanical control and readout of the nanowire are described.

3.1 Design considerations

The apparatus was designed and built in order to perform experiments covering precise quantum control of the ultracold ion, quantum engineering schemes for the ion quantum states via the mechanical drive of the nanowire and potentially quantum sensing or quantum logic experiments by combining both species. The design of this device was based on a scalable approach towards quantum technology and quantum computation experiments [105, 126], where shuttling, splitting and combination of different atomic and molecular ions is required. A miniaturized segmented layer ion trap with a combination of a conductive nanowire may provide those possibilities by shaping precisely the trapping potentials and creating dedicated experimental zones. A crucial consideration of this device was to preserve the harmonicity of the trapping potential while performing coherent quantum experiments with the charged nanowire

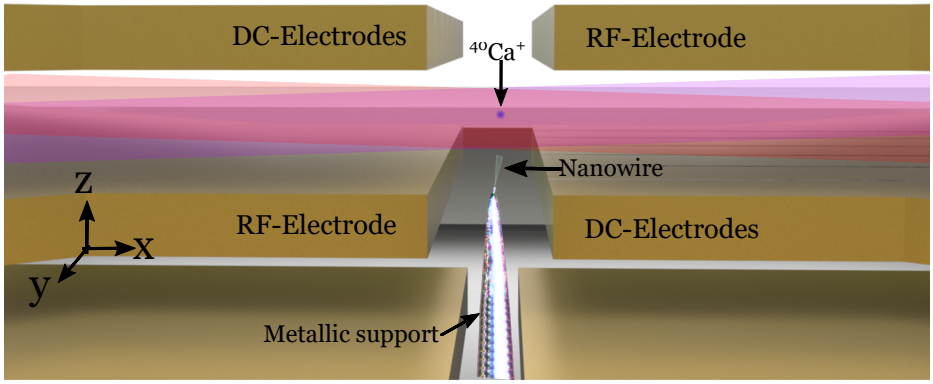

Figure 3.1: Schematic representation of the trapping region showing the cooling laser beams for the ion, an ultracold $^{40}Ca^+$ ion, the RF and DC electrodes and the conductive nanowire on a metallic support. The x and z are the radial directions and y is the symmetry axis of the trap.

inside the trapping region. Although surface ion traps are easier to fabricate and to scale, they offer a relatively shallow trapping potential with stronger anharmonicities [104] as opposed to miniaturized linear traps [127, 128]. Also, the perturbation from the charged nanowire requires to mitigate the ion micromotion, therefore an additional compensation electrode was placed above the trapping region. Because of the large mass mismatch between the two coupled oscillators, only the ion will be displaced while the nanowire acts as a phonon tank in this case. However, with some modifications this trap design could be implemented at cryogenic temperatures, at which the nanowire thermal excitations are weaker and sympathetic cooling of the nanowire from an ultracold ion or a Coulomb crystal can be investigated. This design allows for multiple upgrades at later stages without big changes in the main construction design. Details for the individual components of the ion trap and nanowire assembly are discussed throughout this chapter.

3.2 Trap Design

Trap wafers The design of the miniaturized ion trap was inspired by Ref. [129]. A schematic of the experimental region of interest is presented in Fig. 3.1 which shows a view of the transverse (x,z) plane of the trap. The direction y vertical to the image view is the direction that spreads along the symmetry axis of the trap. The trap consists of a stack of gold-coated aluminum wafers clamped together on top of

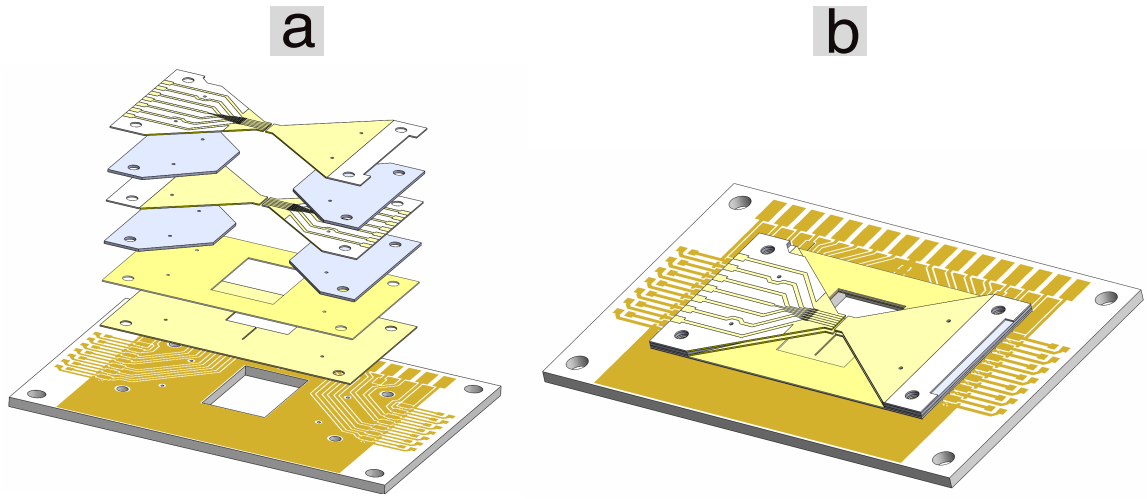

Figure 3.2: Drawing of the full trap stack. An exploded view is shown in (a) with the different layers of the trap. From top to bottom: top RF and DC wafers, spacers, bottom RF and DC wafers, spacers, big spacer, mask wafer and PCB (printed circuit board). The big spacer was omitted from the actual trap, as it didn't offer any mechanical advantage and in order to reduce the height for easier wire-bonding process. The fully assembled trap on the PCB is shown in (b), where one can see the holes for alignment and screws for clamping, and the gold tracks on the PCB for the connections to the feedthroughs.

a PCB as is shown in Fig. 3.2. The trap consists of two RF and two DC electrodes Fig. 3.3, and the latter have seven segments each. The RF electrodes were used to generate time-varying electric fields for the dynamical confinement of the ion in the transverse directions. The DC electrodes fulfill multiple roles as with the static electric potentials that they generate they are responsible for the ion confinement along the trap symmetry axis y, for tilting the principal axes of the trap, for compensating the excess micromotion and for shaping the trapping potential. Larger number of DC electrodes ensures more precise control over the motional degrees of freedom of the ion, and offer the possibility to create multiple experimental zones for multiple purposes, for example a zone where the ions are loaded and then they are shuttled towards the experimental zone where they overlap with tightly focused laser beams for their quantum state readout. The targeted dimensions of the trap were 400 μm tip-to-tip distance in the x and z directions. The aim was to create a trapping potential as harmonic as possible, while having a relatively large trap depth, such that the ion stays confined after the nanowire perturbation to the trap. Each wafer has 200 μm thickness. Based on the material choice (details are discussed in a later section) we had to ensure that the thickness of the wafers is small enough in order for the laser

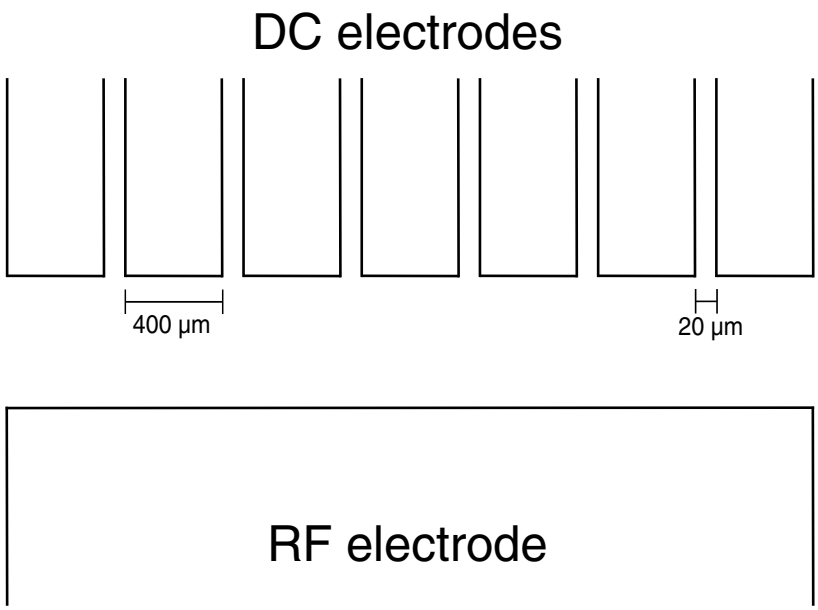

Figure 3.3: Top view of one of the trap layers showing the RF electrode opposed to a segmented DC electrode with 400 μm finger width and 20 μm gap between the fingers.

cutter to penetrate the volume of the material end-to-end, and at the same same time to be thick enough in order to be as resilient as possible during mechanical work. A drawing of the top DC wafer is shown in Fig. 3.4 with all the dimensions. Each DC wafer consists of 7 parts for the individual DC channels each one having 400 μm width and are separated with each other with a 20 μm gap. On the top part of the wafer there are two holes of 1.7 mm diameter that allow for screws to go in for clamping together the hole stack of the trap. The two smaller holes of 0.5 mm diameter, present in all of the trap wafers are made for aligning the wafers. The final alignment of the trap assembly is very crucial, because even small misalignments can cause various problems during ion confinement such as displacement of the trap center, heating and dephasing of the ion due to stronger anharmonic effects and micromotion. The heating rates though can be reduced effectively with cooling ion-traps [130, 131] and cleaning electrode surfaces [132, 133]. However, as experience has shown already, there are large fluctuations of heating rates for different ion traps and during the design process it is difficult to estimate them, since they do not follow any particular law [134]. The small opening on the right side as is shown in Fig. 3.4 was made to ensure access to the RF wafer that was located right under that DC wafer. Those two wafers were separated from a smaller spacer wafer of 400 μm thickness (Fig. 3.5).

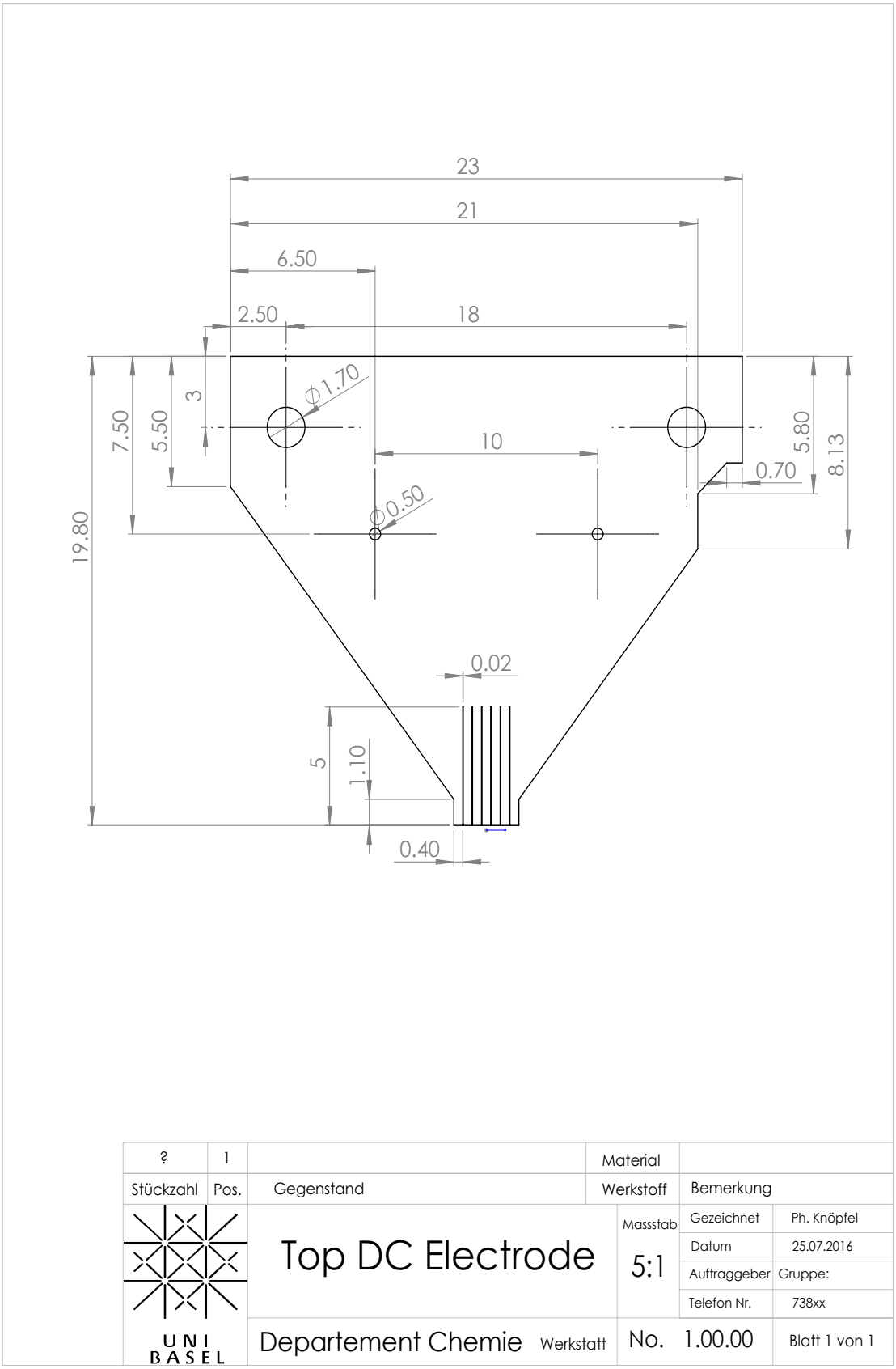

Figure 3.4: DC wafer detailed drawing.

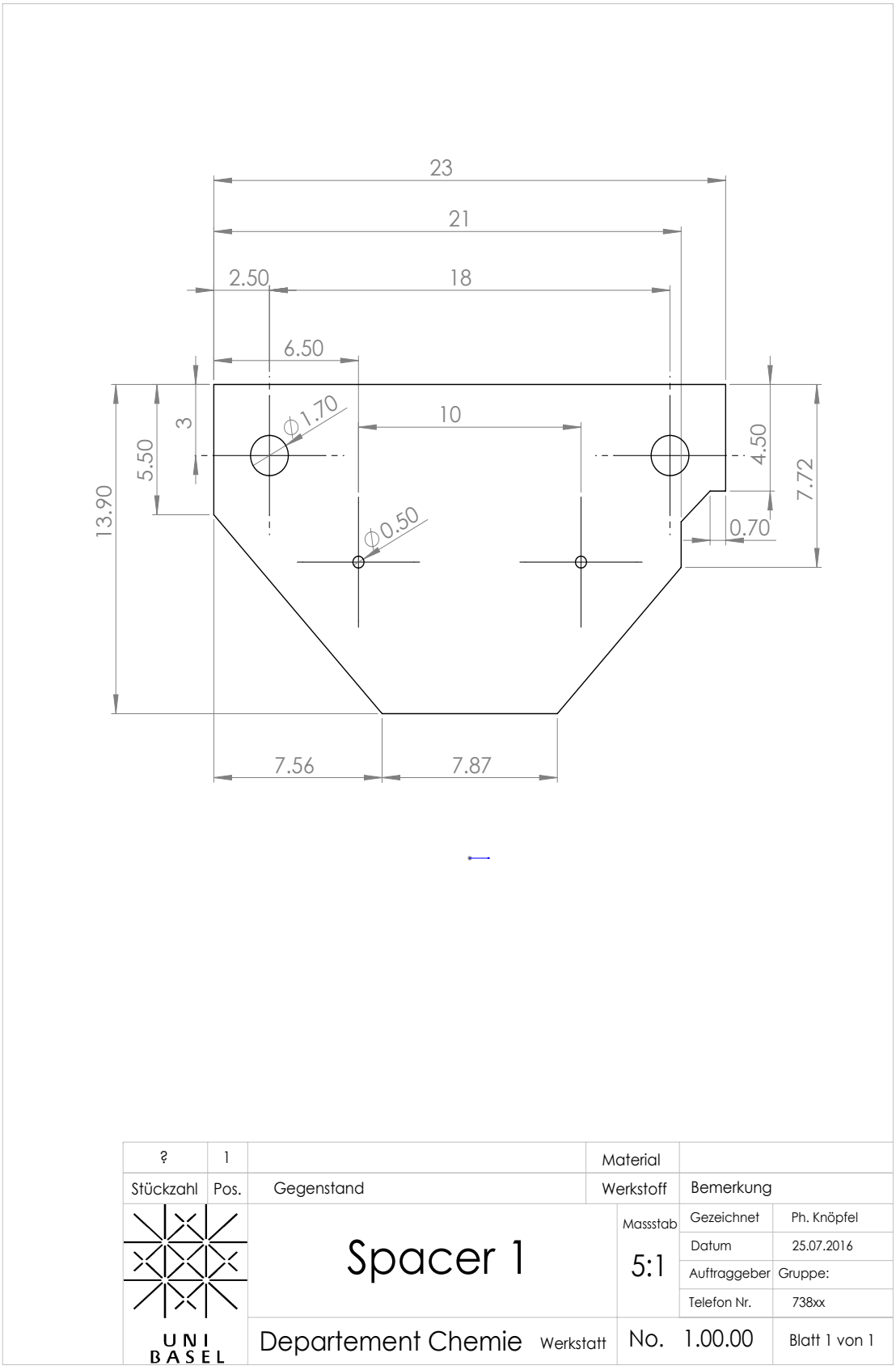

Figure 3.5: Spacer wafer detailed drawing.

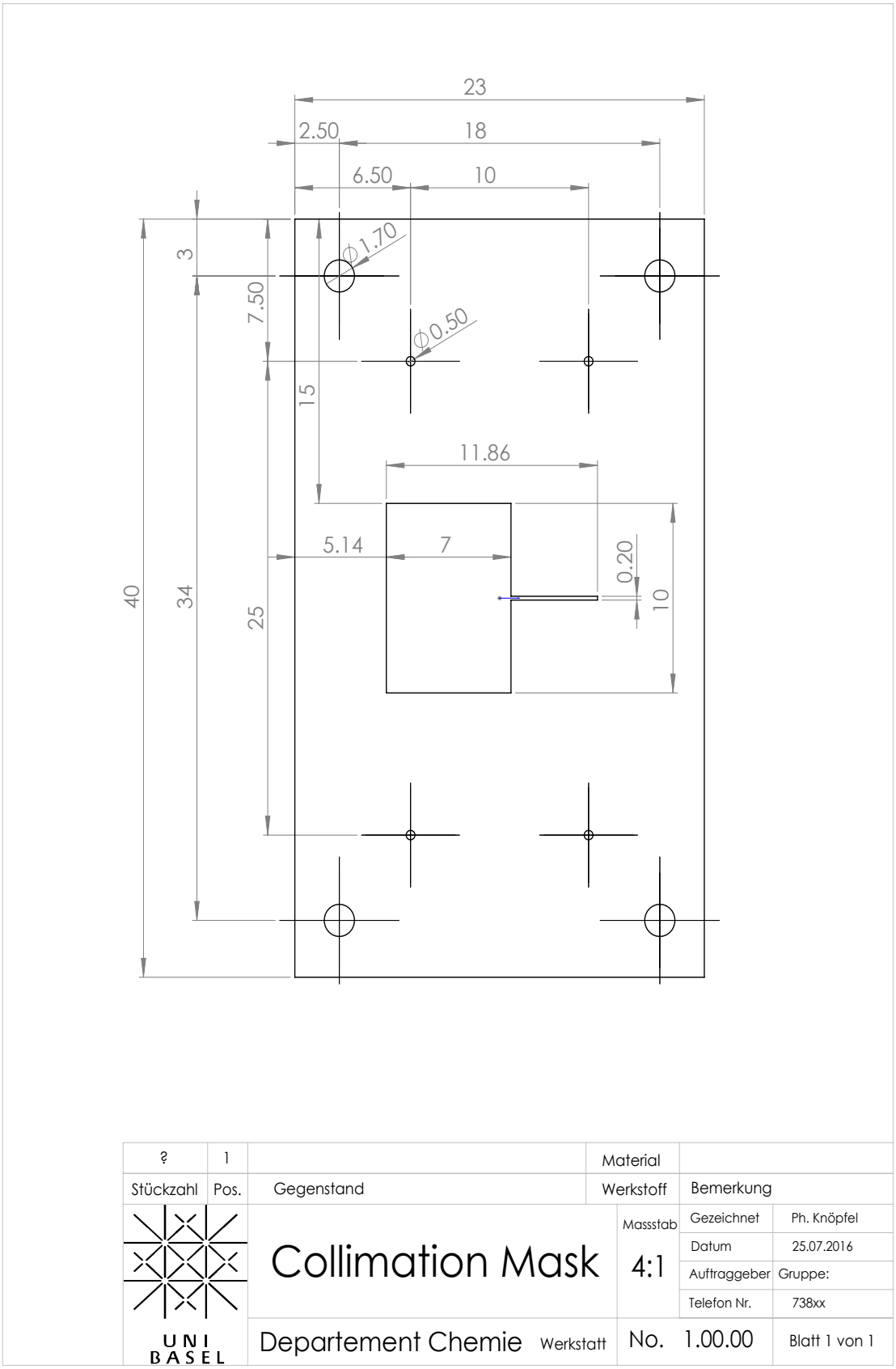

Figure 3.6: Mask wafer detailed drawing.

Mask Wafer In order to prevent Ca deposition on the trap electrodes from the atomic oven source during loading, an additional mask wafer was designed as shown in Fig. 3.6. This wafer is a 40 × 23 mm rectangle with a 10 × 7 mm opening in the middle with a small slit that extends from the edge of the opening for 4.86 mm along the trap symmetry axis. The narrow slit has an opening of 200 μm as opposed to 400 μm which is the distance between the electrodes of the trap. In this way the mask wafer is blocking out all of the calcium atoms that might hit the trap electrodes. Additionally, during the alignment stage the slit acted as a reference for the two individual sets of electrodes along the x-axis, since the slit is perfectly centered.

3.3 Trap Simulation

The electric potentials generated by the trap electrodes were calculated by solving numerically the Laplace equation for a three-dimensional electrostatic model [135] of the trap using FEM (Finite Elements Methods) calculations, that are implemented in the COMSOL Muliphysics software [136]. For calculating the trap depth, the ion motional frequencies and the nanowire perturbation to the trap, the adiabatic approximation was used. Within this approximation the total effective trapping potential Φ_{tot} is given as a sum of a time-independent pseudopotential Φ_{RF} and a static potential Φ_{DC}

$$\Phi_{tot} = \Phi_{RF} + \Phi_{DC} = \frac{V_{RF}^2 Q^2}{4M\Omega_{RF}^2} \, ||\nabla \Phi_{RF}||^2 + Q \sum_i^n V_i \Phi_{DC,i}. \tag{3.1}$$

Here, M and Q are the mass and charge of the $^{40}Ca^+$ ion, respectively, V_{RF} and Ω_{RF} denote the RF amplitude and frequency, respectively, and Φ_{RF} and Φ_{DC} stand for the RF and DC basis functions, respectively, which are the solutions of the Laplace equations obtained by applying unit voltage to the RF and the ith DC electrode. The voltage applied to the ith DC electrode is denoted as V_i. Each time the basis function of an electrode was calculated the rest of the electrodes were set to ground. The aforementioned trap dimensions and the trap operating parameters were chosen such that the trapping potential is preserved under an electric potential of 100 mV applied to the nanowire. The parameters chosen here in order to fulfill the requirements of the

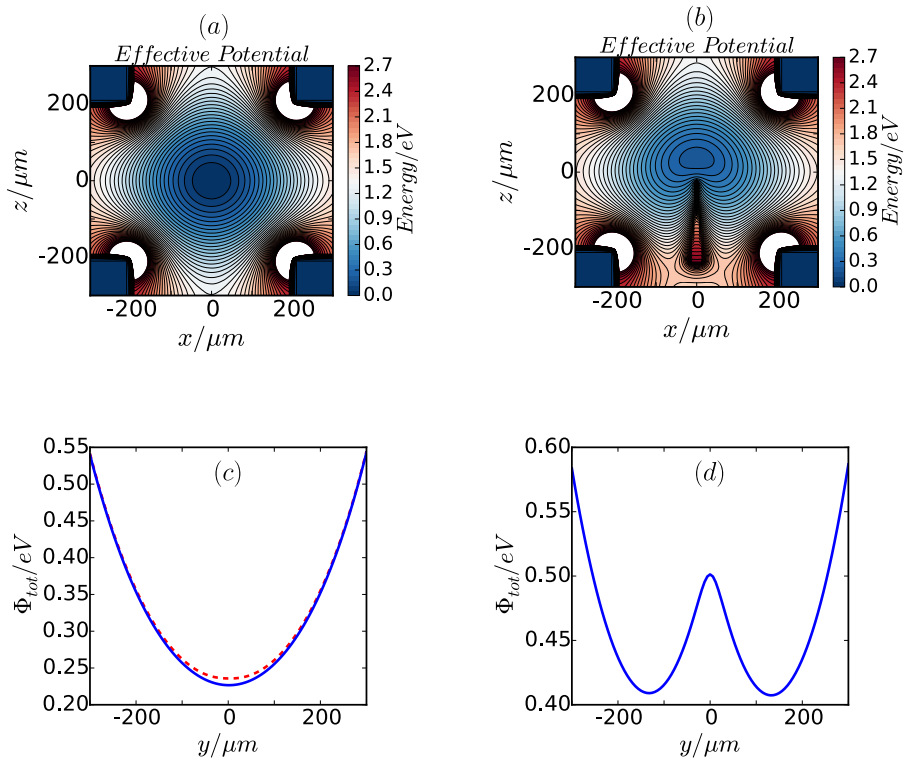

Figure 3.7: Two dimensional cuts of the total effective potential Φ_{tot} in the radial (xz) plane for (a) the unperturbed (without nanowire) and (b) perturbed (with nanowire) cases. The (c) and (d) plots are one dimensional cuts of the total trapping potential along the longitudinal (y) direction through the center of the trap. The (c) plot represents the unperturbed (without nanowire, blue solid line) and the perturbed (with nanowire at 100 mV, red dashed line) trapping potentials. Plot (d) shows the perturbed trapping potential when a voltage of 1.5 V is applied on the nanowire.

hybrid experiment were $V_{RF} = 150$ V, $\Omega_{RF}/2\pi = 35$ MHz and $V_i = \{ V_1, V_2,...,V_{14} \} = \{10, 8.43, 0, 0, 0, 8.43, 10, 10, 8.43, 0, 0, 0, 8.43, 10\}$ V.

Figure 3.7 shows the result of the FEM calculations. In Fig. 3.7a and 3.7b two dimensional cuts of the 3D calculations are shown in the xz-radial plane for the unperturbed and perturbed trapping potential respectively. The perturbation presented in 3.7b assumes a voltage of 1.5 Volts applied to the nanowire, and the equilibrium point of the trap is shifted upwards along the z-axis. Experimentally, this shift of the ion z-position can be mitigated by an additional DC electrode which resides approximately 1 mm above the top electrode of the trap, which is shown later in this chapter in Fig. 3.16. This compensation electrode applies an electric field downwards along the z-direction and can push the minimum of the trap back to the initial position. However, the applied bias voltage of 1 V is an exaggeration according to the actual experimental parameters, where only approximately 100 mV

bias nanowire voltage are sufficient, and the purpose of this is to present and extra degree of freedom for shaping trapping potentials or compensating for possible issues with the traping fields. With a nanowire bias voltage of 100 mV the 2D-cut of the trapping potential on the xz-plane looks almost identical to the unperturbed case, because the perturbation to the trapping potential is very weak and the harmonicity is basically preserved. The effect of the biased nanowire is more clearly visible in the 1D-cuts of the trapping potential along the symmetry y-axis as can be seen in Fig. 3.7c, where the blue solid line represents the total trapping potential along the y-axis with the aforementioned DC configuration and the red dashed line shows the effect from the biased nanowire. Nevertheless, this effect is very weak and the harmonicity of the trapping potential along the y-axis is preserved. Although a biased nanowire of 1.5 V does not offer anything relevant for the hybrid dynamics of the system, it gives the ability to shape the trapping potential along y-axis into a double-well Fig. 3.7d. Double well potentials have been engineered in segmented-layer microtraps before by applying appropriate negative voltages in the central electrodes [129]. Nevertheless, the DC voltages that can be applied on the trapping electrodes are limited due to the output of DAC cards which is typically on the order of ± 10 V and the distance between the electrodes which doesn't allow very high voltages. This usually makes the barrier of the double well relatively low, giving additional ways for the ion to escape each well. On the other hand, a biased nanowire can be very finely positioned in every direction inside the trapping region, and the barrier of a double-well potential can be shaped more accurately on-the-fly by varying the position and the bias voltage of the nanowire. In this way one can create deeper trapping wells adjacent to the barrier and it may open the possibility of multispecies trapped ion experiments towards higher excitations and coherence times.

In order to calculate the Mathieu stability parameters and subsequently the secular frequencies of the principal axes of oscillation of the ion, a multidimensional

generalization of the Mathieu parameters was performed, where the Hessian matrix was calculated at the center of the trap, according to the following expressions

$$A_{ij} = \frac{4Q}{M\Omega_{RF}^2} \begin{pmatrix} \frac{\partial^2}{\partial x^2} & \frac{\partial^2}{\partial x \partial y} & \frac{\partial^2}{\partial x \partial z} \\ \frac{\partial^2}{\partial y \partial x} & \frac{\partial^2}{\partial y^2} & \frac{\partial^2}{\partial y \partial z} \\ \frac{\partial^2}{\partial z \partial x} & \frac{\partial^2}{\partial z \partial y} & \frac{\partial^2}{\partial z^2} \end{pmatrix} \Phi_{DC} \tag{3.2}$$

$$Q_{ij} = \frac{2Q}{M\Omega_{RF}^2} \begin{pmatrix} \frac{\partial^2}{\partial x^2} & \frac{\partial^2}{\partial x \partial y} & \frac{\partial^2}{\partial x \partial z} \\ \frac{\partial^2}{\partial y \partial x} & \frac{\partial^2}{\partial y^2} & \frac{\partial^2}{\partial y \partial z} \\ \frac{\partial^2}{\partial z \partial x} & \frac{\partial^2}{\partial z \partial y} & \frac{\partial^2}{\partial z^2} \end{pmatrix} \Phi_{RF}, \tag{3.3}$$

where the Φ_{RF} and Φ_{DC} are the RF and DC potentials respectively. For an RF frequency $\Omega_{RF} = 35$ MHz and amplitude $V_{RF} = 150$ V the values of the diagonal elements of the A- and Q-matrices are shown in table 3.1. Typically, stable conditions

	Q_{xx}	Q_{yy}	Q_{zz}	A_{xx}	A_{yy}	A_{zz}
$^{40}Ca^+$	0.1465	0	-0.1465	-5.0 $\times 10^{-4}$	12 $\times 10^{-4}$	-7.0 $\times 10^{-4}$

Table 3.1: Values of the diagonal elements of A- and Q-matrices for the calcium ion.

for trapping ions are achieved when $0 < Q_{ii} < 1$ and $A_{ii} \approx 0$. The negative values of the A_{xx} and A_{zz} imply that the static voltages effectively reduce the force that the ion experience in the radial plane. The RF peak amplitude and frequency were chosen such that the Q_{xx} and Q_{zz} values are close to 0.1. Typically, in linear Paul traps values below 0.5 are used, but with $Q_{ii} \approx 0.1$ coupling of the micromotion with the secular motion is small and this reduces the heating due to micromotion, which makes the cooling process easier.

3.4 Fabrication

The uniqueness of this experiment, which is the simultaneous implementation of a nano-optomechanical setup with ion-trapping technology, required the fabrication of several custom pieces, including the ion trap. The fabrication process was based on Refs. [129, 137]. The trap is made of a stack of alumina wafers (Al_2O_3) which were laser machined in order to define various slits for the trapping region and holes for clearance and alignment. Following this step, the wafers were then coated with gold,

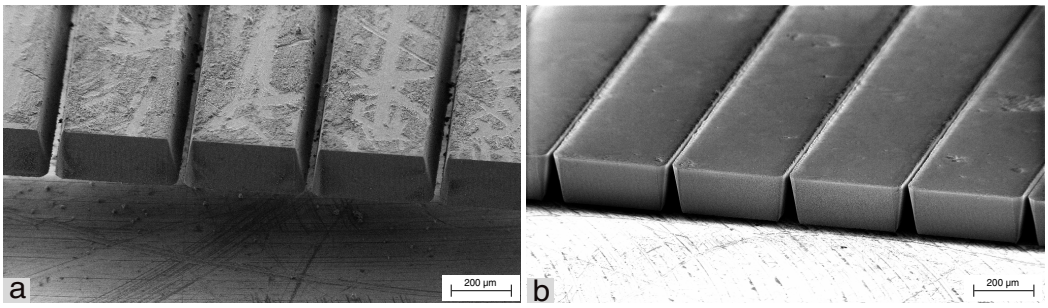

Figure 3.8: SEM images of the laser-machined DC electrode wafers (a) before and (b) after the cleaning with Piranha solution. During the machining process an air sucker was used in order to remove the fumes and most of the finely cut material. The remaining material on the initial wafers was aggressively removed with a thorough Piranha cleaning.

in order to define the electrodes and the contacting tracks. As a first step this was done with thermal evaporation of gold followed by electrolytic deposition. Finally, all the wafers were assembled on top of a PCB, and the contacts between the PCB and the wafers were performed with wire-bonding. The laser machining of the wafers was done by Beat Lüscher from Fachhochschule Nordwestschweiz [1], and all other fabrication steps were performed at the University of Basel [2].

Substrate The substrate material for the wafers is poly-crystalline aluminum oxide 99.6 %(Al_2O_3) [3]. All the wafers, i.e. the electrode wafers, the spacers, the masks for gold patterns and the trap mask to prevent contamination from the oven, were made from the same alumina material. Both facets of the wafers were polished, which is essential for the gold deposition. This material was chosen for the excellent surface properties for gold deposition, for the low dielectric loss (0.0001 at 1 MHz), for the relatively good thermal conductivity in order to dissipate heat from resistive losses in the trap and because it is relatively inexpensive compared to sapphire or similar materials. However, it has some drawbacks. It has very low elasticity, which makes it very brittle, especially for thicknesses below 200 μm. This makes the assembly and alignment process more challenging, especially for our ion trap , where each electrode belongs to a different wafer as opposed to [129, 137]. Moreover, if one needs to perform experiments at cryogenic temperatures it might be advantageous to use a

[1] Fachhochschule Nordwestschweiz, http://www.fhnw.ch/technik/ippe/dienstleistung
[2] https://www.unibas.ch/
[3] CoorsTek, material: Superstrate 996

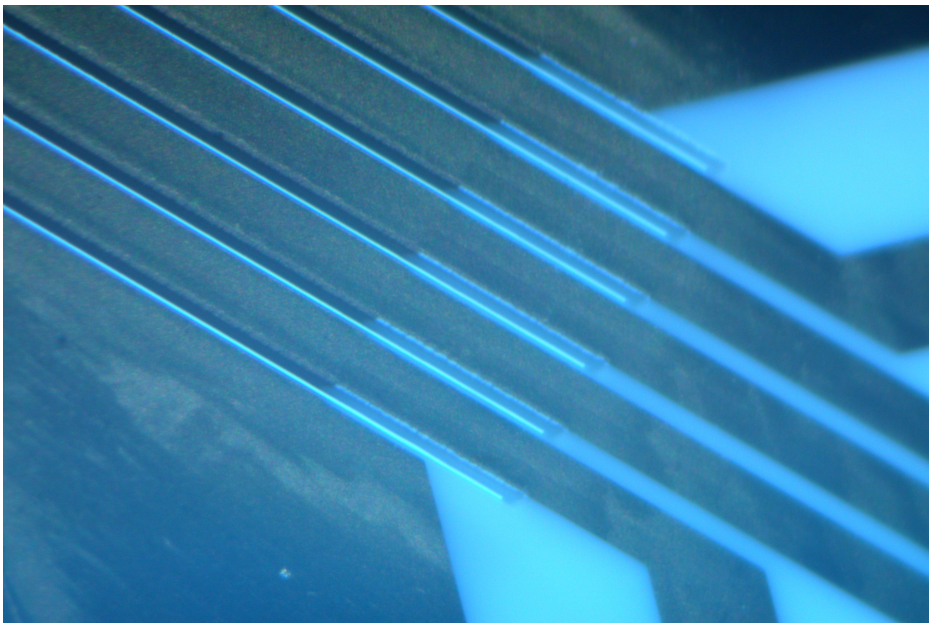

Figure 3.9: Microscopy image of a DC wafer after thermal gold deposition. With a tilting angle of 21° during the multistep deposition, the gold layer penetrated completely into the narrow gaps covering most of the surface along the length of each finger. In this way we prevented exposed dielectric material, which would have accumulated charges and therefore would have caused issues for the ion motion.

material which offers better thermal conductivity. For instance, the Superstrate 996 has a thermal conductivity of 26.9 W/mK.

Laser Machining To define the structural features of the wafers a picosecond laser at 355 nm was used during the laser-machining process. After optimization, the holes, openings and slits of each wafer and the gaps between the DC electrodes were engineered accurately. The width of each of the fingers are 400 μm. The funnel shape of the gaps shows the orientation of the laser cutter from the wider side towards the narrower. The narrower gaps are the ones in the line-of-sight of the ions and they were cut at 20 μm, leaving the wider part of each gap at 50-60 μm. Those slits extend for 5 mm towards the holes of the wafer, which makes the fingers extremely brittle, and consequently imposes greater challenges during the alignment and the electric circuit tests of the trap.

Cleaning After laser machining a rigorous cleaning procedure was applied to the wafers. First, they were fully submerged into a piranha solution (sulfuric acid 95-98 % and hydrogen peroxide 30 %, 3:1) for 1 hour at 90 °C in order to clean both surfaces.

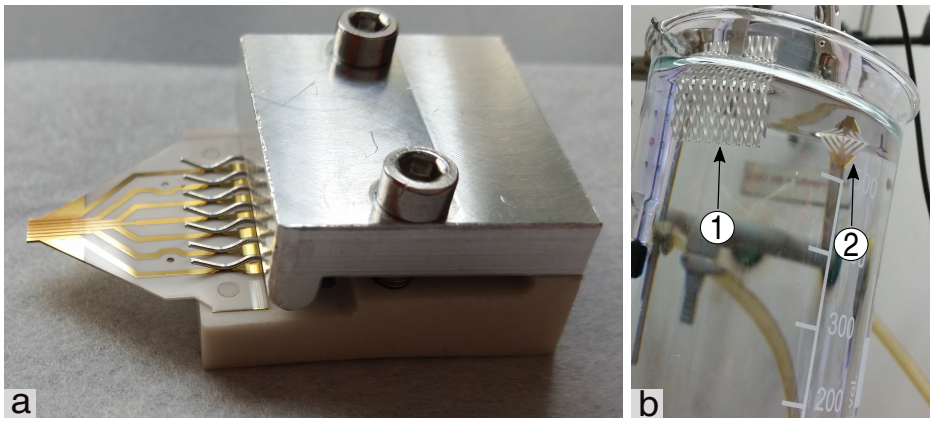

Figure 3.10: Electroplating setup. In (a) a custom-made holder is shown. The bottom part of the holder was made out of PEEK. The stainless steel plate from above is pressing with the screws upon the thin metallic wires, which ensure good electrical connection with each of the individual DC channels for the electroplating. Image (b) shows the (1) platinum plate (anode) and (2) the DC wafer (cathode) dived into the gold solution during the electroplating process.

Since the wafers were so brittle, and in order to avoid damage, only a small magnetic stir was used during the cleaning. Afterwards, the wafers were rinsed sequentially with ultrapure water, Acetone, Isopropanol and again ultrapure water. The first rinsing with water is essential, as it removes Piranha residuals, which might cause a violent reaction with Acetone.

Thermal Evaporation The deposition of gold was done with an electron beam evaporation machine. The procedure required a 3D evaporation to cover both sides of the wafer and the sides of the fingers in between the narrow gaps. The device did not have a rotational stage inside, and each step of the process was dedicated to individually coat each side of the wafer sequentially with the corresponding metallic layers. The wafers were mounted at a 21° angle with respect to the direction of the atomic beam. Prior to gold deposition, a 20 nm titanium layer was deposited on each wafer side in order to create strong adhesion forces and help the gold layer to stick better on the surface. Then, a 200 nm gold film was deposited on the titanium covered surface. Using the electron beam evaporation machine in the Physics department of University of Basel, the rate of deposition of the titanium layer was 0.07 nm/s and that of gold was 0.08 nm/s. This slow deposition ensures a homogeneous and smooth gold surface. This is crucial, especially for the surface parts near in the line-of-sight of the ion, since roughness can cause anharmonicities, distorted potentials and ion

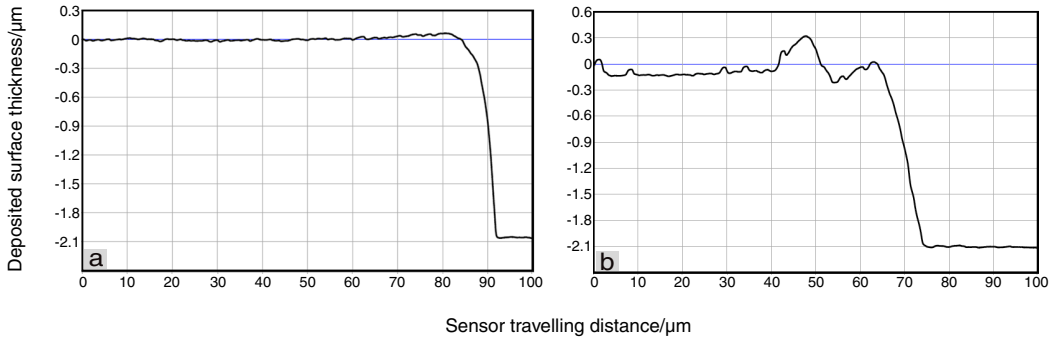

Figure 3.11: Electroplating: The graphs in (a) and (b) show the thickness of the surface that was achieved after the electroplating for two different wafers. The measurements were performed by a needle sensor by measuring the height of the tip of the sensor as a function of the scanning region. The thickness after the thermal evaporation was 200 nm, and we see that with the electroplating we achieved the target thickness value. This shows the controlled process for each individual gold plating procedure using the parameters described in the text.

heating. The electrodes and connection patterns on the wafers were fabricated during the deposition by using shadow masks. The shadow masks were laser machined from the same wafer material and cleaned as described above. They were aligned on every side of the wafers, before every deposition step by using an optical microscope. In this fashion, there were no outgasing sources in the chamber that could oxidise the titanium layer, which it would lead to bad adhesion of the gold layer (e.g. blisters) and to very long pumping times in order to counter this effect. The tilting angle during the multistep deposition allowed the gold to penetrate all-the-way into each gap and create very good contact with the sides of the fingers, avoiding in this way exposed dielectric parts as can be seen in Fig. 3.9.

	Rate (nm/s)	Thickness (nm)
Ti	0.07	20
Au	0.08	200

Table 3.2: Values for the deposition rate and thickness of gold during electron beam evaporation.

Electroplating To thicken the gold surface and close possible gaps, electroplating was used. This was performed in a home-made plating setup depicted in Fig. 3.10. A single wafer was first mounted on an adapter with stainless steel wires, which ensure electrical contact for each electrode channel. Before the wafer was put into the gold solution it was biased with a small negative voltage of 0.01 V [137]. Then,

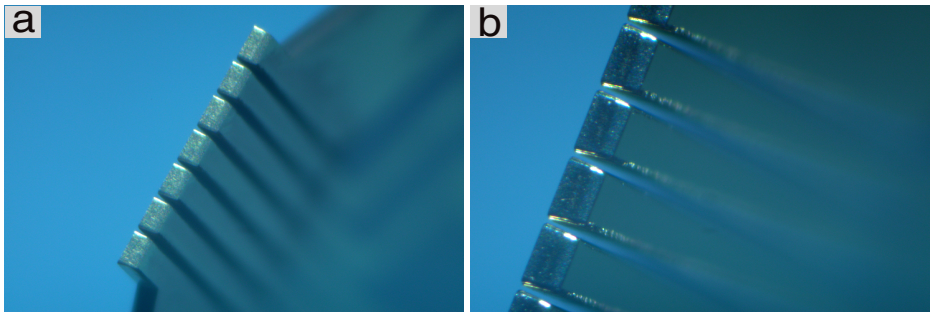

Figure 3.12: Ion trap electrodes: Microscopy images after (a) thermal deposition and (b) electroplating.

the wafer was submerged into the non-cyanide Metakem SF [4] gold solution. One liter of this solution was heated to 60 °C and slowly agitated with a magnetic stir bar. Hand-held agitation was avoided to prevent breaking the fingers of the wafer. The platinum plate acted as the anode and the gold surface of the wafer as the cathode. The desired surface texture and thickness was achieved by applying 3 mA current for 8.5 minutes. This results in a surface thickness of around 2 μm as can be seen in Fig. 3.11. The electrocatalytic plating process is very sensitive to the state of the plating solution. Thus, the pH value of the solution was monitored both before and during the electrolytic deposition. The pH value of the solution sometimes changed due to evaporation of ammonia and water during heating and due to the reduction of the gold sulfate during plating. Both effects lower the pH of the solution, leading to formation of gold grains. If this occurs, the solution needs to be filtered before each use. When needed, the pH was adjusted to the value of approximately 8 pH. Figure 3.12 shows the same gold coated wafer after the thermal evaporation and after the electroplating.

Printed Circuit Board The PCB board has many purposes. It serves as mechanical carrier of the trap wafers and it bridges the electrical connections between the PCB and the electrodes of the wafers to the vacuum feedthtoughs. Furthermore, it has low-pass RC filters which are soldered on every DC line and provide a first stage of filtering RF noise that is coupled to the DC electrodes. The substrate of the PCB is a rectangular polyimide plate with dimensions 40 × 60 mm and 1.55 mm thickness, with gold tracks and pads to ensure electrical connections and capacitor placement.

[4] Metakem,http://www.metakem.de/

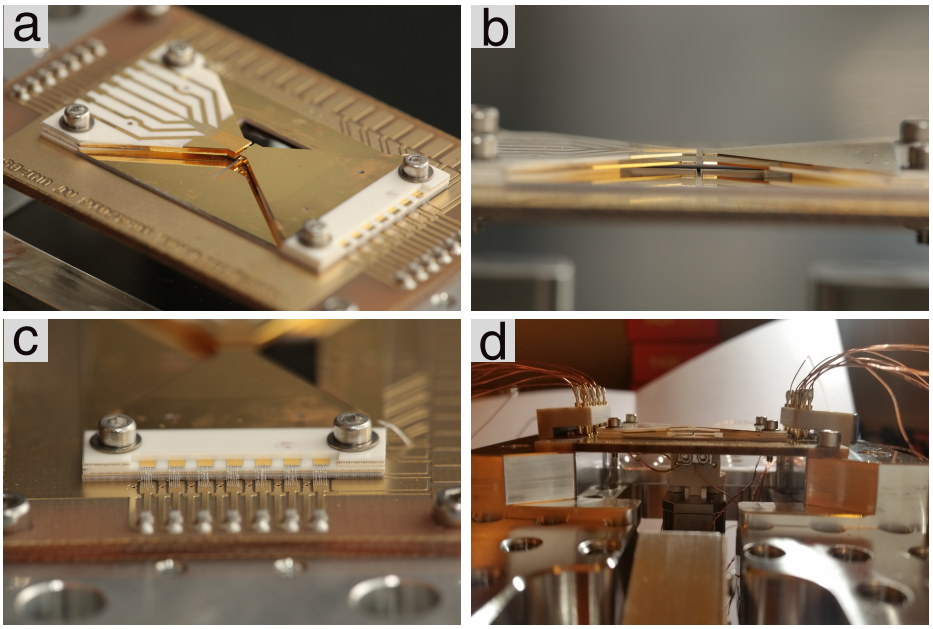

Figure 3.13: Ion trap: The fully assembled ion-trap is shown in (a), clamped with screws on top of the PCB, while (b) shows the trapping region from the side. The aluminium wire bonds (20 μm in diameter each wire) and the RC-filters for the DC channels are shown in (c). Each DC and RF electrode consists of 6-7 wire bonds. Spring-loaded metallic pins were clamped in a PEEK adapter from each side of the trap along the x-axis as shown in (d). Kapton-coated copper wires were soldered on top of each pin for the connections with the feedthroughs.

There is also a gold plate on the bottom of the PCB for grounding the connections. The capacitors[5] that were chosen have a value of 1000 pF and were soldered with a UHV-solder on the PCB prior to the wafer assembly. The resistors of the RC circuit were installed outside the chamber, on the feedthroughs connectors of each DC channel. They had 10 kΩ resistance, which gives a 100 kHz corner frequency for the 1000 pF capacitance.

Trap Assembly As a first step during the assembly of the trap, all the wafers were placed in their specific order on top of the PCB board. Each wafer was placed one at a time with the help of very thin pins through the alignment holes. Afterwards, the screws and nuts were installed to clamp together the stack loosely. The left and right hand side of the trap, with respect to the side of the zy-plane, were aligned independently. The narrow slit from the mask wafer was the reference point of the alignment, as it was placed almost perfectly in the center of the construction. The

[5]Walsin Technology, Ceramic multilayer chip capacitors with SMD ceramic cap, Size: 0603, Nominal voltage: 50 V, capacitance: 1000pF, Tolerance: +/−5%, Dielectric: COG/NPO

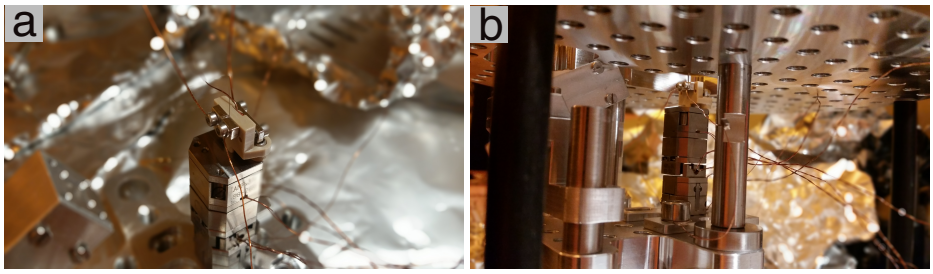

Figure 3.14: Nanowire assembly: (a) The PEEK adapter lies on top of the stack of the nanopositioners. A thin metallic plate presses the nanowire from the front against the PEEK adapter while holding the electrical connections for biasing, filtering and grounding the nanowire. From the back side, the PEEK holder has a groove housing the piezo disk used to drive the nanomechanical motion. (b) The stack of nanopositioners is mounted on a small breadboard, which in turn is mounted below the big breadboard with stainless steel pillars.

alignment of the trap wafers was performed manually by hands under an optical microscope. After the screws were tightened and kept the whole structure stable, wire bonds were attached to connect the conductive parts of each channel of the PCB with the wafers of the trap. Initially, a gold wire-bonding technique was used, as the same material would stick better with itself. Nevertheless, the gold wire-bonding machine had limited working distance along the z-axis of the trap, and the electrode channels were too high for this device to create the bonds with the PCB. An aluminum wire-bonding device was used instead that offered more motional flexibility. The aluminium bonds connected the channels of each wafer with the PCB as shown in Fig. 3.13c. For each RF and DC channel, 6 to 7 wire-bonds were created. Two PEEK adapters with spring loaded pin connectors were installed above the capacitors from both sides of the trap. Those connectors established the connections for the the DC electrodes to the feedthroughs with Kapton coated wires, that were soldered directly on each pin. Then, a 0.2 mm diameter stainless-steel wire was placed on top of one side of the trap, which acted as the compensation electrode for the ion micromotion and ion positioning along the z-axis of the trap.

3.5 Nanomechanical Setup

Nanopositioners To position the nanowire in all three dimensions, a stack of piezo motors was used as can be seen in Fig. 3.14. The stack was mounted on a metallic adapter plate with slits on the bottom side in order to move the whole stack along

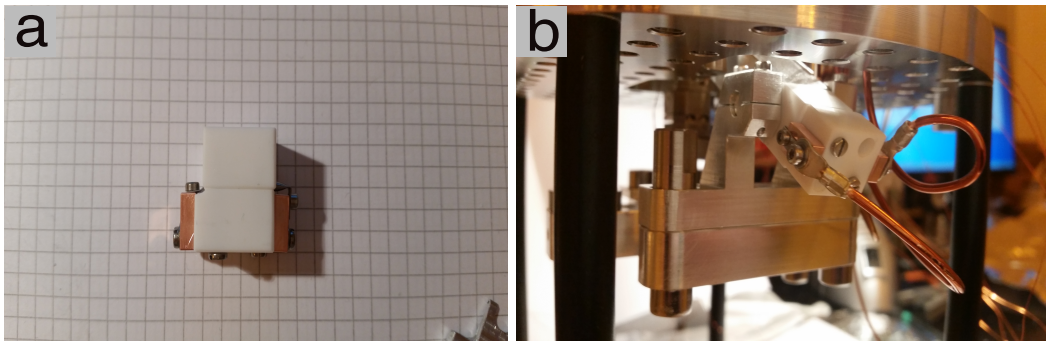

Figure 3.15: Ca oven assembly: (a) Two MACOR pieces are clamped together, holding in between the source of atomic calcium. The copper parts that are mounted on each side ensure the electrical connections for each end of the oven source, while offering at the same time mechanical stability. (b) The oven-Macor structure can be disassembled independently from the back of the metallic cannon, offering an easy way to change atomic sources without changing the alignment of the whole assembly.

the x-direction during the first coarse alignment with respect to the trap center. The stack consists of two ANPx51 and one ANPz51 linear positioners (steppers) and one ANSxy50 scanner from Attocube[6]. The two ANPx50 steppers are mounted 90° with respect to each other to position the nanowire in the xy-plane. Each ANPx51 linear positioner is made out of titanium and has 15 mm × 15 mm × 9.2 mm dimensions. The travelling range of the steppers is 3 mm with 3.5 μm linear positioning range at 300 K and sub-nanometer resolution. The ANPz51 stepper for positioning the nanowire along the z-direction has a travelling range of 2.5 mm and was placed at the bottom of the stack. The ANSxy50 scanner provided a scanning region of the nanowire in the xy-plane of 30 μm × 30 μm at 300 K temperature.

PEEK holder On the top part of the linear positioners stack, a PEEK holder was mounted. On the back side of the holder a groove was fabricated, into which a 5 mm diameter piezo disk was inserted. On the front side, the nanowire was mounted by being pressed upon the PEEK part with a very small metallic plate. With this configuration, we were able to make the ground electrical connection and to apply the bias voltage on the nanowire. The conductive nanowire that was used in this work is a cylindrical shape Ag_2Ga with 200 nm diameter and 20 μm length. The nanowire was already mounted on a cylindrical tungsten wire of 100 μm diameter. The piezo disk was connected with one of the outputs of the lock-in amplifier, and by applying

[6]https://www.attocube.com/

a sinusoidal waveform of specific frequency and amplitude we were able to drive the nanowire motion.

3.6 Atomic oven source

To provide calcium atoms to the trapping region an atomic oven source was build. A custom made metallic tube with a sealed slit was connected from both sides with 1 mm Kapton coated wires for providing current. During this process, initially an indium seal is melting to open up the slit to allow calcium emission. Then, the supplied current is increased which heats up the metallic tube and at a specific temperature calcium atoms are evaporating from the source. The oven was mounted between two MACOR pieces on copper plates. The copper plates provide mechanical stability for the oven and good thermal conductivity, as the current wires were mounted on the copper plates. This MACOR oven assembly was mounted on the back of a stainless steel renctangular shape collimation piece. Along this metallic collimation piece was an opening that allows the calcium atoms to travel ballisticaly towards an exit hole of 2 mm diameter. The oven source was shielded from the MACOR piece and the atoms inside the metallic piece were shielded by a metallic plate on the side of it. The whole structure was mounted on an adapter which allowed us to move it along the z-direction and changing the angle of the oven for alignment with respect to the center of the trap. The alignment was performed by using a 423 nm laser on the back side of the assembly, before the MACOR-oven piece was mounted. With the small aperture of the collimation piece and in combination with the narrow slit of the mask wafer of the trap, we were preventing contamination of the electrodes, especially the DC electrodes, where big amounts of deposited calcium could create short circuits.

3.7 UHV-Chamber and components

The chamber of this experiment was a 10-inch-diameter spherical octagon[7] with eight CF40 ports. In one of those ports, an adapter flange was installed with five CF40 ports, one of which had feedthroughs for half of the DC electrodes of the trap and for

[7]Kimball Physics: MCF1000-SphOct-H2C8

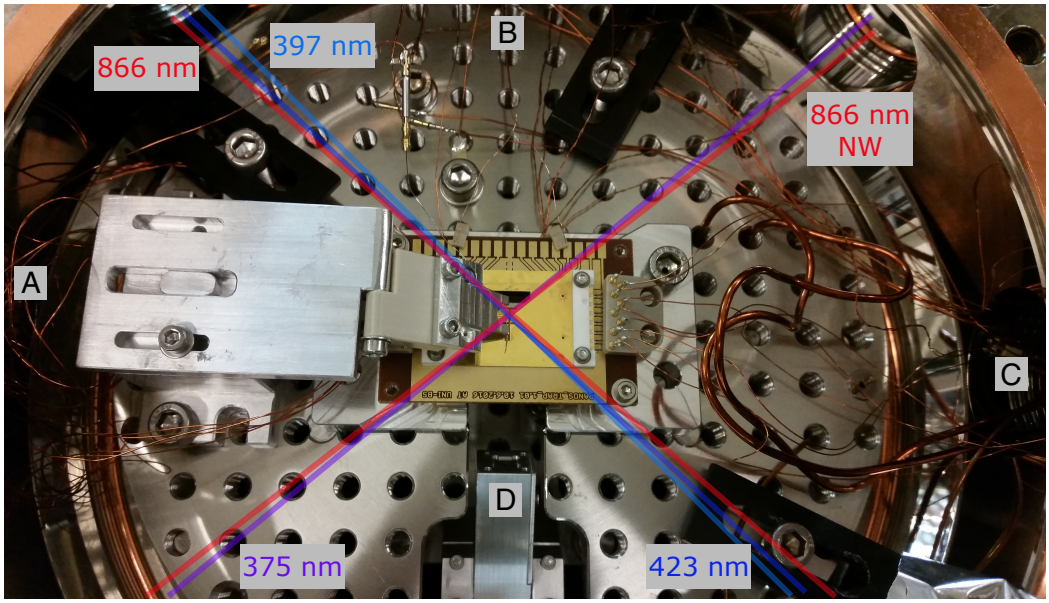

Figure 3.16: Top view of the fully constructed experiment inside the chamber with the ion and nanowire laser beams. The view-port A consisted of a feedthrough port where half of the DC channels of the trap the nanowire electronics were connected. The view-port C ends in T-shape flanges for the electrical connections of the other half of the trap DC channels, of the thermocouple, of the oven and of the nanopositioners. View-ports C and D have windows for additional laser beams that are going to be used in future stages of the experiment.

the nanopositioners connections, and the rest were used for the pressure gauge, atomic source oven and thermocouple connections. On the diametrically opposite port the feedthroughs for the rest of the DC electrodes and the nanowire were installed. On another port, an adapter was installed with a view port and a T-shaped flange with feedthroughs for the RF-resonator. With the combination of a turbopump[8] and a modular pumping station[9], a pressure of 5×10^{-8} mbar was reached. Typically, for trapped-ion experiments pressures below 10^{-9} mbar are required. The remaining gas in the chamber is usually H_2O which sticks easily to the walls of the chamber and is generated by various components that outgas. For this reason, the whole chamber was heated to 180 ° Celcius for 9 days continuously. One must be cautious during heating of the chamber, because the nanopositioners should reach 150° Celcius maximum temperatures for being operational. After this heating procedure we reached pressures far below 5×10^{-10} mbar.

[8]Oerlikon: MAG W600
[9]Pfeiffer: HiCube Classic

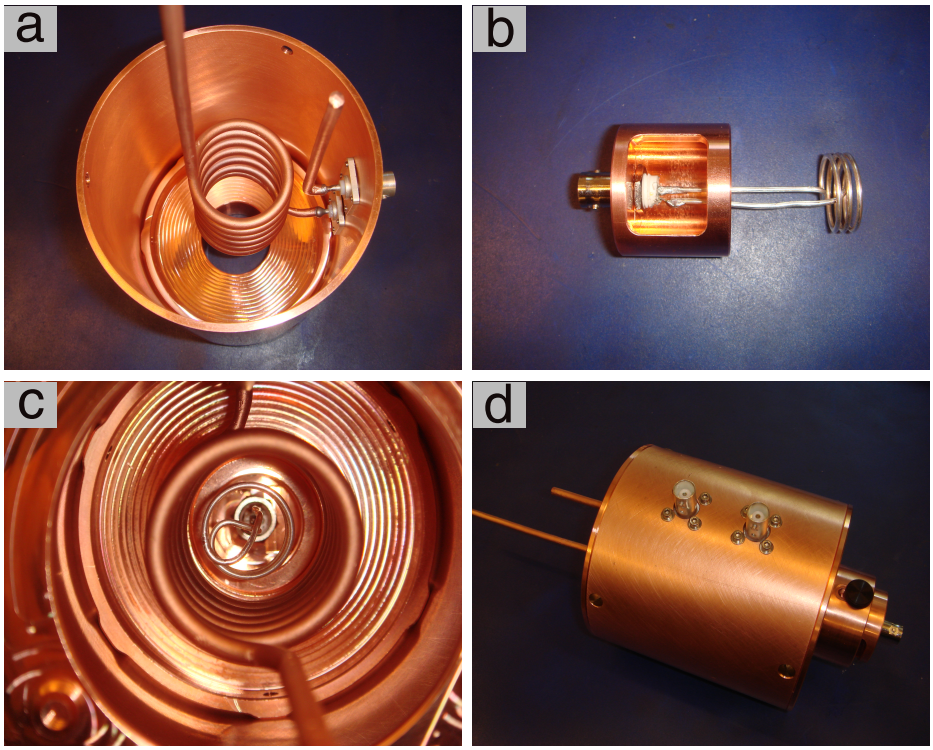

Figure 3.17: Images of the RF resonator. In (a) the 100 mm diameter cylindrical copper shield is shown along with the inner coil of 6 turns and 34 mm diameter. (b) The antenna is soldered on the movable stage for the coarse frequency matching. The assembled resonator from (c) the inside and (d) the outside is shown.

3.8 RF resonator

A common approach to reach relatively high RF amplitudes for the radial confinement of the ions is the amplification of an RF signal with a helical resonator. There are guidelines for designing such resonators described in [138, 139]. Following these approaches, it is possible to build a helical resonator with desired quality factor Q and resonance frequency Ω_0. The challenging part, though, is that the resonance frequency is not known beforehand and it is not easy to estimate the shift, after the resonator is attached to the actual trap. The capacitative load of the trap, along with the wires and the feedthroughs shift the resonance frequency towards smaller values than the expected ones. In our experiment, during the design of the resonator we estimated a load capacitance of around 20 pF, which leads to an estimation of the resonance frequency of 35 MHz. The measured capacitance of the actual load, though, was measured to be 45 pF, which resulted in a resonance frequency of 22.8 MHz. We were able at this frequency to have perfect match of the resonator with less than 2% reflection. According to the equations presented in [139] the estimated Q-factor

should be approximately 120. The measured value was 20. The reason behind this effect is due to the geometry and dimensions of this trap. The electrodes are almost perfect parallel plates with 400 μm distance between them, which leads to a strong capacitative coupling between the RF and DC electrodes. This phenomenon is not so strong in typical linear Paul traps with cylindrical shape electrodes. The strong capacitative coupling pulled out most of the energy that was fed into the trap resulting in a maximum peak voltage of approximately 160 V. Nevertheless, the maximum RF amplitude provided by this resonator was much higher than the one needed for strong radial confinement according to the stability parameters.

3.9 Laser setup

3.9.1 Lasers and imaging system for the ion

397 nm laser The 397 nm laser is the primary laser for Doppler cooling which addresses the $^2S_{1/2}$ to $^2P_{1/2}$ transition of the $^{40}Ca^+$ ion. This laser is a home-built diode laser with external current and temperature controllers[10]. Figure 3.18 shows the 397 nm laser setup implemented from this laser source until the last coupling to a polarization maintenance (PM) fiber before its delivery to the experiment. Initially, the beam is split with a 90:10 splitter, and the low power part is coupled into a wavemeter[11] in order to determine and lock the wavelength. A fiber switch allowed sequential reading of the wavelenth with a total cycle update rate of ≈ 5 Hz, and the wavelength was stabilized via a proportional-integral-derivative (PID) feedback loop within ± 2 fm, between the read-out from the wavemeter and the voltage applied to the piezoelectric element of the laser. After a series of optical elements that clean the polarization and reduce the beam spot size, the 397 nm beam goes through the main feature of this laser setup which is an Acousto-Optic Modulator (AOM). This AOM unit was custom-designed[12] for our experiment and its purpose is to diffract the light, creating in this way various orders with different frequencies. In this way, one can scan the 397 nm laser frequency, by tuning the frequency of the acoustic wave, establish fast pulses and switch the laser on and off. A double-pass configuration was

[10] Thorlabs: ITC4001
[11] HighFinesse: WSU-30
[12] Brimrose: TEM-110-6-397, Span: 66MHz, Rise time: 85 ns, Diffraction efficiency: 80%

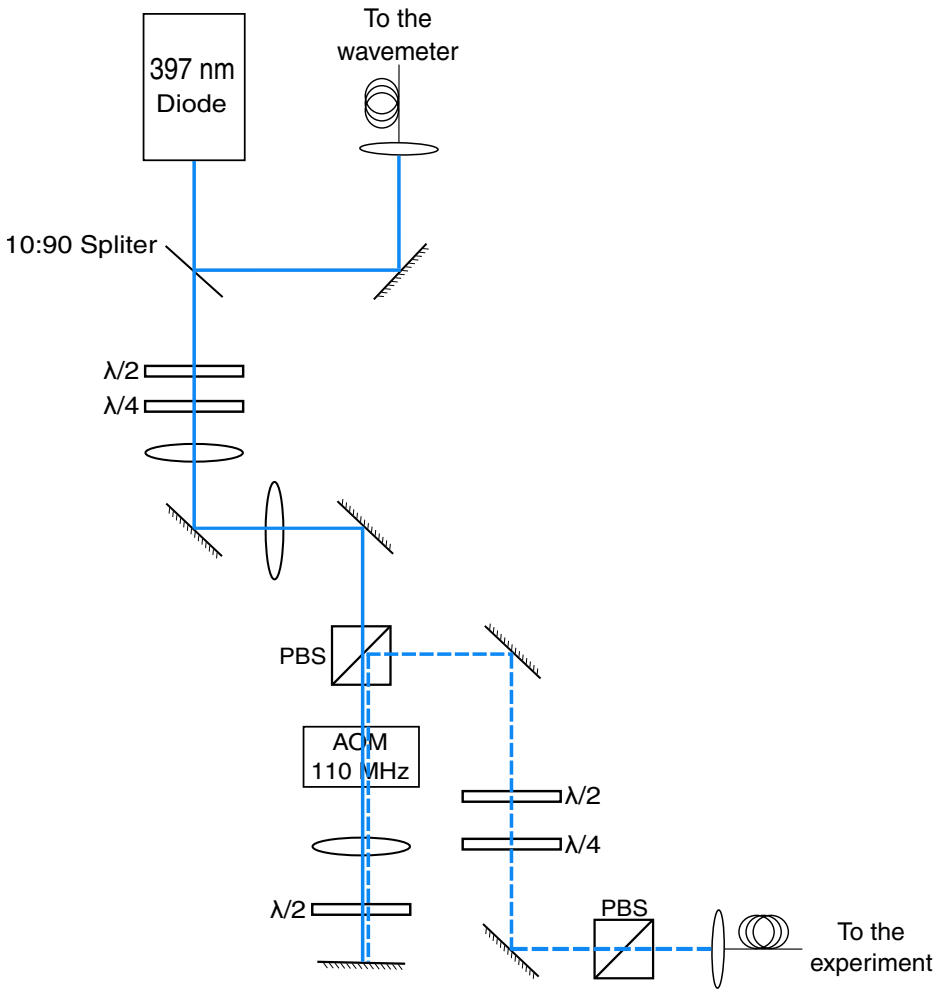

Figure 3.18: Schematic of the optical components of the 397 nm laser beam setup before the beam is delivered to the experiment.

implemented before coupling the beam to the PM-fiber which gives some advantages. Firstly, the frequency shift is doubled which enables us to scan a wider frequency range of the laser. Secondly, laser beam alignment problems can be effectively eliminated by compensating for beam deflections. On the second pass through the AOM, the beam with its polarization rotated by 90° is deflected back, such that it counter-propagates the incident laser beam and it is separated from the input laser beam with a polarizing beam splitter (PBS). Right before the PM-fiber, we placed another PBS in order to finally match the incoming beam to be coupled with the fast or slow axis of the fiber.

Repumpers For repumping population from the $^2D_{3/2}$ state while addressing the main cooling transition we used light at 866 nm. The optical setup of this laser beam before delivery to the experiment can be seen in Fig. 3.19. The 866 nm laser beam[13]

[13]Toptica photonics: DL100

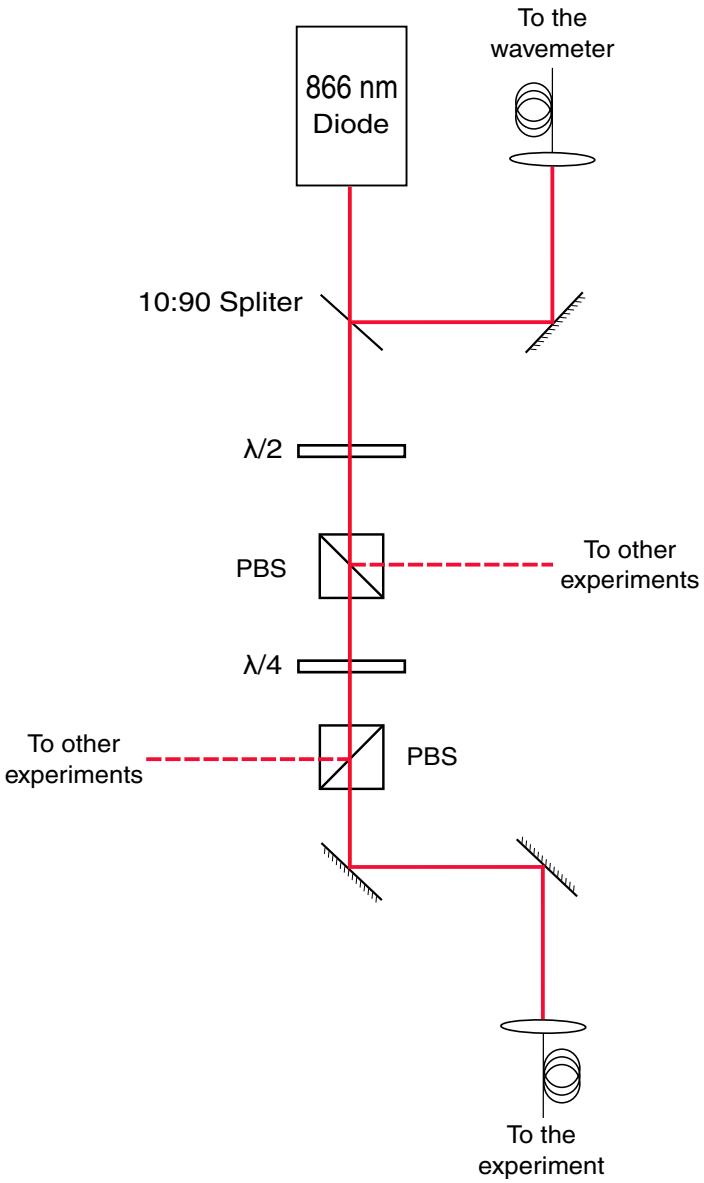

Figure 3.19: Schematic of the 866 nm laser beam beam setup before its delivery to the experiment.

was chosen to run continuously for the purpose of initial experiments, so we avoided installing additional optical elements for switching the beam. The second repumper that was going to be used was a 854 nm laser, which is responsible for repumping population from the $^2D_{5/2}$ state. The path and the optics for this beam were designed but not installed, since it was beyond the scope of the current stage of the experiment.

Photoionization The laser setup for the ionization of the neutral calcium atoms was built for the two photon process as demonstrated [140, 141]. For this, a custom made 423 nm diode laser was used for the first excitation of the atoms, followed by

a 375 nm free-running diode laser for the excitation to a state close to the ionization threshold. The absolute wavelength of the 423 nm laser was found by observing fluorescence from the calcium atoms, and it is Doppler shifted under an angle $\approx 35°$ with respect to the atomic beam from the oven. Its wavelength was monitored with the wavemeter and no further steps for stabilization were taken. The laser setup for the photoionization lasers is similar to the 866 nm laser setup, consequently schematics were omitted.

Imaging System For imaging the fluorescence of Ca^+, a microscope and a charge-couple-device (CCD) camera were installed above the viewport of the top flange of the chamber in order to collect the light scattered during the cooling process of the calcium ions with spatial resolution. The microscope has a magnification of 11.5× and the CCD camera has a nominal resolution of ≈ 2 μm. The numerical aperture (NA) and working distance of the objective lens were 0.13 and 64 mm respectively. An optical bandpass filter[14] was placed between the microscope and the camera in order to supress stray light reflected from the surface of the electrodes.

3.9.2 Laser and imaging system for the nanowire

As seen in Figure 3.20 the 866 nm beam is split at a first PBS. One part was used as the ion repumper and the other was used for the optomechanical readout of the nanowire. The nanowire readout setup was inspired by [74], where the transmitted signal after the nanowire was collected by a photodetector and analyzed with a lock-in measurement. In our experiment, we could not achieve such tight beam focus as in [74] (e.g. 550 nm beam waist), due to the distances of the free space optics and the fact that no in-vacuum lenses were used closer to the trap. The focus that we achieved on the nanowire was approximately 10 μm in diameter. Despite that big difference in focus at which we managed to read the driven motion motion of the nanowire. The choice of the laser towards the red side of the spectrum is attributed to the fact that we wanted to avoid strong absorption from lower wavelength lasers that could lead to heating of the nanowire and possible geometrical and mechanical deformations. With such free space optical configuration, and such large beam spot

[14]Semrock: 400/12 nm BrightLine® single-band bandpass filter

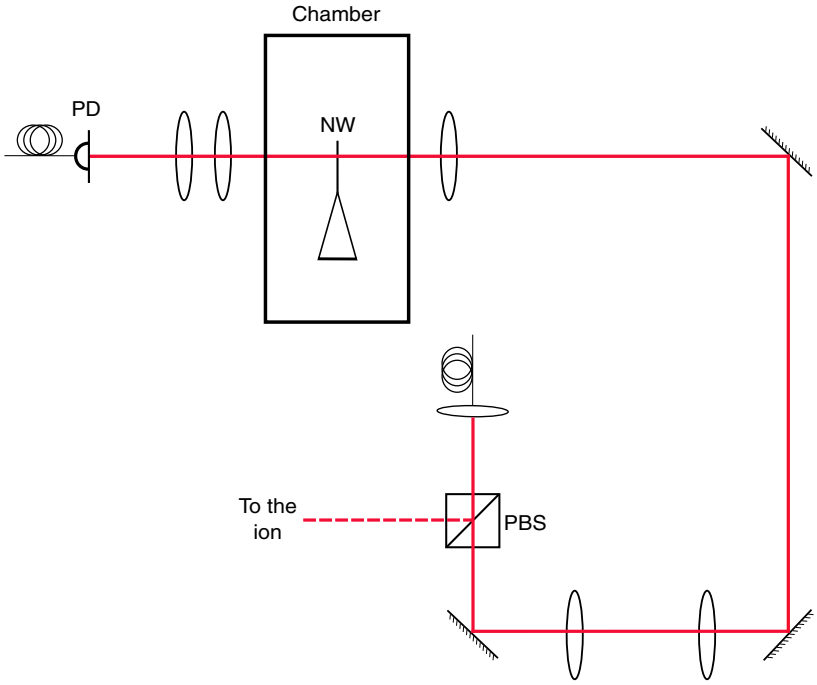

Figure 3.20: Schematic of the 866 nm laser beam that was used for the nanowire read-out. The beam was shared between the ion and the nanowire with a 50:50 PBS. A series of optical components focus the beam down to 10 μm diameter on the nanowire, and afterwards the transmitted light was collected with additional lenses on a quadrant photodiode.

size, is still possible to detect the nanomechanical motion with even less than 50 μW of laser power. Finally, the transmitted light from the nanowire was collected after a series of lenses on a Si PIN quadrant photodiode[15].

[15]Hamamatsu: S4204

Chapter 4

Theoretical results

This chapter presents the theory that describes the ion-nanowire interaction in the classical and quantum regime, when such an experiment is performed at room and cryogenic temperatures, respectively. Based on the characterized perturbation of the ion trapping potential from the FEM calculations, the parameters that describe the dynamics of the direct mechanical drive of the trapped ultracold ion from the charged nanowire were determined. By manipulating the drive of the nanowire and the effects of the trapping potential anharmonicities various ion quantum states can be generated. The computational model of the ion-nanowire interaction will be introduced in the first section 4.1. The classical calculations of the hybrid system will be introduced in section 4.2, where the force fields that were used in the calculations are described. The next section 4.3 presents the engineering of the ion quantum states when the ion motion is quantized and the nanowire motion is described as a classical oscillating field. Section 4.4 shows the ion-nanowire interaction when the nanowire motion can be described quantum mechanically (e.g. at extreme cryogenic temperatures).

4.1 Computational model

The direct mechanical coupling between the ion motion and the charged nanowire, which is considered at room temperature, occurs due to their mutual Coulomb interaction near resonance. The nanowire drive was chosen to interact with the ion motion only along the trap symmetry axis. The benefits of driving the nanowire along the longitudinal axis are manifold. The ion motional frequency along this axis

can be matched easily, as opposed to the radial modes, by appropriately choosing the applied voltages to the DC electrodes of the trap. As it will be shown later, the charged nanowire will induce frequency shifts on the motion of the ion, that can be compensated with the DC electrodes. Also, the axial ion frequency can be well decoupled from the radial modes by choosing the RF parameters such that the ion frequencies in the radial plane are much higher than the axial frequency. In this way, even if the nanowire is geometrically not perfectly aligned with respect to the symmetry axis of the trap and driven along one of the two radial directions, the effect on the radial modes is negligible. Moreover, the RF field of the trap is not expected to significantly affect the motion of the nanowire due to the large difference between the RF frequency and the natural frequency of the nanowire. The RF pickup by the nanowire is suppressed by a filter capacitor. The nanowire biased voltage might cause a spatial shift of the ion equilibrium position and might induce micromotion, as it is placed a bit further from the RF null line. This effect mitigated by an additional compensation electrode that pushes the ion back to the RF null line. The results presented here are only considering the dynamics of the ion along the trap symmetry axis, which are unaffected by small radial displacements. Also, when the nanowire is not mechanically driven, it thermally oscillates with an amplitude of ≈ 1 nm at room temperature. It was found numerically that with typical applied voltages of the order of 100 mV on the nanowire, the thermal motion is too small and it does not induce significant dynamics on the ion. Furthermore, when the nanowire is grounded, the leading terms of its interaction with the ion vanish and it merely acts as an additional grounded electrode.

From a Maxwell-Boltzmann distribution a nanowire at 300 K temperature has around 15 million phonons. The nanowire is technically a phonon tank for the ion and the nanowire motion cannot be described with the ladder operators. The approximated effect of the nanowire was taken to be as the one of a classical oscillating electric field generated by a spherically charged particle at its tip acting on the motion of the ion corresponding to the leading term in the electrostatic interaction between the two charge distributions. Thus, the interaction potential in three dimensions reads

$$U_c = \frac{k_c Q_1 Q_2}{\sqrt{x^2 + (y - Y(t))^2 + (z + d)^2}}, \tag{4.1}$$

where k_c is the Coulomb constant, Q_1 and Q_2 are the charges of the ion and the nanowire, respectively, x, y, z are the coordinates of the ion, d is the relative distance between the ion and the nanowire, and $Y(t) = A\ \cos(\omega_{nw} t)$ describes the driving field generated by the nanowire with a specific amplitude A and frequency of oscillation ω_{nw}. The point of origin of the coordinate system is taken to be at the equilibrium position of the ion.

4.2 Classical dynamics

Initially, the ion-nanowire interaction was modeled in the classical regime by molecular dynamics (MD) simulations using the ProtoMol software [142]. A realistic force model that describes properly the ion motion must take into account various forces that are experienced in an RF trap. The main forces are the trapping forces of the electrostatic and dynamic fields in the trap and the laser cooling force responsible for lowering the temperature of the ion. In addition to these, there are mechanisms that are responsible for increasing the ion temperature and counteract the cooling process. There are multiple sources for these heating mechanisms like: heating due to elastic collisions of the ion with molecules of the background gas, heating due to ion interaction with the laser fields and heating due to experimental imperfections, like geometrical asymmetries on the trapping electrodes especially in a line-of-sight from the ion, electronic noise or patch potentials. An additional force field was implemented in ProtoMol in order to describe the ion interaction with the drive of the charged nanowire.

The force model that was used here and includes all of the above interactions reads

$$\mathbf{F}_i = -\nabla U(x, y, z, t) + \mathbf{F}_{cooling} + \mathbf{F}_{heating} + \mathbf{F}_{nw}, \tag{4.2}$$

where $U(x, y, z, t)$ is the time-dependent trapping potential, $\mathbf{F}_{cooling}$ represents the ion cooling force from the laser field, $\mathbf{F}_{heating}$ is the term representing the elastic

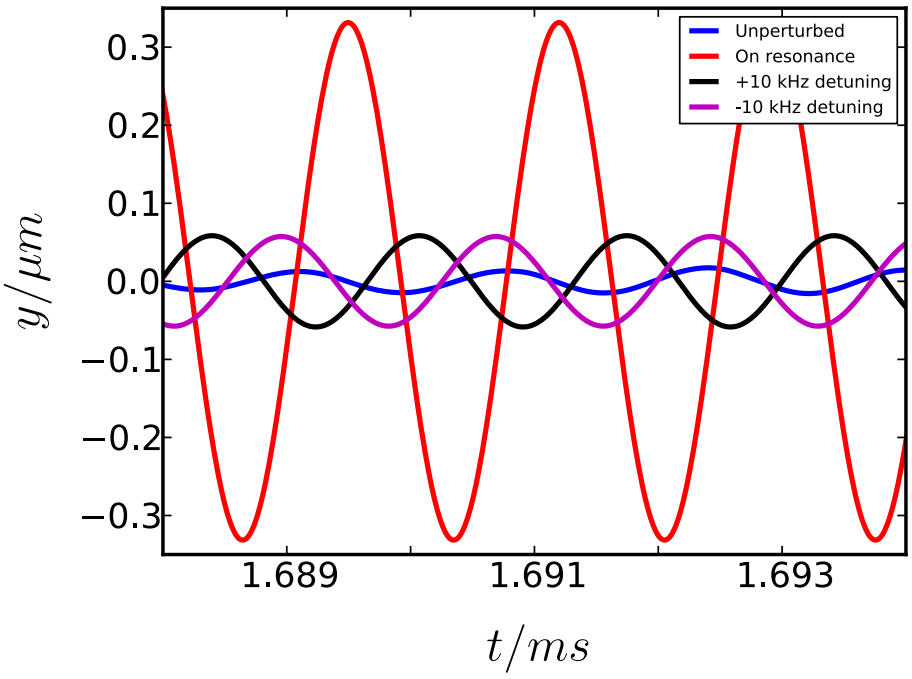

Figure 4.1: Trajectory of a trapped $^{40}Ca^{+}$ ion: unperturbed (blue solid line), driven by an oscillating nanowire on resonance (red solid line) and with the nanowire frequency detuned by 10 kHz (black and magenta solid lines, respectively) above and below the resonance frequency.

background collision, trap imperfections and laser field heating and $\mathbf{F}_{nw}$ represents the nanowire interaction on the trapped ion. The cooling force acting on the ion is implemented as a friction force field and it included general stochastic random momentum kicks that simulate the aforementioned heating mechanisms. The Newtonian equations of motion were solved numerically using the Leapfrog integrator, which is implemented in ProtoMol. The nanowire was driven along the y-axis resonant with the axial frequency of the ion at $\omega_y/2\pi = 600$ kHz with an amplitude of oscillation of 100 nm. The charge of the biased nanowire used for both the classical and quantum calculations is $Q = 1.6 \times 10^{-18}$ C. This value was chosen such that the trapping potential preserves its harmonicity. After setting initial positions and velocities of the $^{40}Ca^{+}$ ion, the MD simulations were initiated with the trapping and friction force fields. The initial temperature of the ion is 40 μK and the nanowire drive is operative during the whole simulation time. Figure 4.1 shows a snapshot of the MD simulations representing the ion axial trajectory for the resonant case as well as with the nanooscillator frequency detuned 10 kHz above and below the resonance frequency.

In the simulation, the drive of the nanowire was continuous while Doppler laser cooling of the ion was maintained. At the time shown, the system has reached a steady state. The blue line represents the unperturbed motion of the ion, the red line represents the ion motion after the nanowire resonant drive and the rest of the lines show the ion motion when it is detuned. The unperturbed motion of the ion corresponds to an oscillation with an amplitude of 10 nm. As expected, a resonant drive of the ion by the nanowire couples energy into the ion motion which reaches amplitudes up to 300 nm in the present case. The efficiency of the coupling, however, reduces quickly with increasing mismatch between the ion and nanowire oscillation frequencies. In this snapshot the random momentum kicks are disabled in order to demonstrate more clearly the interaction strength in this regime. The random momentum kicks would just show an amplitude fluctuation of the trajectory of the ion, which is irrelevant for explaining the coupling behaviour.

4.3 Semi-classical dynamics

To model the quantum dynamics of the ion under the action of the nanowire, the ion-nanowire interaction potential was expanded in a Taylor series, as also discussed in [88], up to second order for small excursions of the ion around its equilibrium position:

$$\begin{aligned} U_c = &\frac{\epsilon}{d} - \frac{\epsilon}{d^2}\, z - \frac{\epsilon}{2d^3}\, x^2 - \frac{\epsilon}{2d^3}\, y^2 + \frac{\epsilon}{d^3}\, z^2 \\ &+ \frac{\epsilon A}{d^3}\, y\, \cos(\omega_{nw} t) - \frac{\epsilon A^2}{2d^3}\, \cos^2(\omega_{nw} t), \end{aligned} \tag{4.3}$$

where $\epsilon = k_c Q_1 Q_2$. The first and last terms are energy offsets which do not affect the dynamics of the system. The degrees of freedom along the y-axis are decoupled from x and z so that the driven dynamics can be described in one dimension. The Hamiltonian is quantized by replacing the position coordinates with the position operators

in the Fock basis. The total Hamiltonian including the trapping potential is written as

$$\begin{aligned}\hat{\mathcal{H}}_{tot} = \hbar\omega(\hat{a}^\dagger\hat{a} + \frac{1}{2}) - \frac{\epsilon}{2d^3}\ \frac{\hbar}{2m\omega}\ (\hat{a}^\dagger + \hat{a})^2 \\ + \frac{\epsilon A}{d^3}\ \sqrt{\frac{\hbar}{2m\omega}}\ (\hat{a}^\dagger + \hat{a})\ \cos(\omega_{nw}t),\end{aligned} \tag{4.4}$$

where $\hat{y} = (\hbar/2m\omega)^{1/2}\ (\hat{a}^\dagger + \hat{a})$ and the factor $(\hbar/2m\omega)^{1/2}$ corresponds to the zero point fluctuations. $\omega \equiv \omega_y$ and $\hat{a}$, $\hat{a}^\dagger$ are the annihilation and creation operators of the motional degrees of freedom of the ion in the harmonic trap.

Re-expressing this Hamiltonian in frequency units we get

$$\hat{\mathcal{H}}_{tot} = \omega(\hat{a}^\dagger\hat{a} + \frac{1}{2}) - s(\hat{a}^\dagger + \hat{a})^2 + g(\hat{a}^\dagger + \hat{a})\ \cos(\omega_{nw}t), \tag{4.5}$$

where $s = \epsilon/(4m\omega d^3)$ and $g = [\epsilon A/(\hbar d^3)][\hbar/(2m\omega)]^{1/2}$. The first term is the energy of a quantum harmonic oscillator which describes the unperturbed motion of the ion in the trap. The other two terms are the contributions of the effect of the nanowire on the motion of the ion. The second term, which is quadratic in the sum of the ladder operators, gives a shift to the ion vibrational levels and also introduces squeezing. The last term incorporates the coupling to the driving field and also introduces displacement of the ion.

One of the most common ways to study the dynamics of such an open quantum system is with the Kossokowski-Lindblad equation or master equation in Lindblad form [143]. This equation describes the non-unitary evolution of the density matrix that is trace preserving and completely positive for any initial condition. Dissipation of the quantum system is implemented via the construction of collapse operators or superoperators. The Lindblad master equation for an N-dimensional system's reduced density matrix can be written:

$$\frac{d\hat{\rho}}{dt} = -\frac{i}{\hbar}\ [\hat{\mathcal{H}}_{tot}, \hat{\rho}] + \hat{\mathcal{L}}\hat{\rho}, \tag{4.6}$$

with

$$\hat{\mathcal{L}}[\hat{C}]\hat{\rho} = \sum_{i=1}^{N^2-1} \gamma_i(\hat{C}_i\ \hat{\rho}\ \hat{C}_i^\dagger - \frac{1}{2}\{\hat{C}_i^\dagger\ \hat{C}_i, \hat{\rho}\}), \tag{4.7}$$

where $\hat{\rho}$ is the density matrix of the system and $\hat{\mathcal{L}}$ is the Lindblad superoperator which describes the decoherence of the corresponding degrees of freedom [143]. In the case of our hybrid system, the nanowire interacts directly with the electric monopole of the ion, affecting only the ion vibrational levels. The spin degrees of freedom in this interaction are decoupled and they are not included in the numerical calculation of the Lindblad master equation. For a derivation and more extensive discussion for the Lindblad master equation see the Refs [144, 145].

Another technique that is used for simulating open quantum systems is the quantum jump method, also known as Monte Carlo wave function method [146]. The quantum jump method is much like the master-equation treatment except that it operates on the wave function rather than using a density matrix. In this method one evolves system's wave function in time, where at each time step a quantum jump (discontinuous change) may take place with some probability. The calculated system state as a function of time is known as a quantum trajectory, and the desired density matrix as a function of time may be calculated by averaging over many simulated trajectories. For a Hilbert space with dimensions N, the number of wave function components is equal to N while the number of density matrix components is equal to N^2. Consequently, for certain problems the quantum jump method offers a performance advantage over direct master-equation approaches. More specifically, where as the density matrix describes the ensemble average over many identical realizations of a quantum system, the QMC (Quantum Monte-Carlo) approach to wave function evolution allows for simulating an individual realization of the system dynamics. Here, the environment is continuously monitored, resulting in a series of quantum jumps in the system wave function, conditioned on the increase of information gained about the state of the system via the environmental measurements. In general, this evolution is governed by the Schrödinger equation with a non-Hermitian effective Hamiltonian

$$\hat{\mathcal{H}}_{eff} = \hat{\mathcal{H}}_{sys} - \frac{i\hbar}{2}\sum_i \hat{C}_n^+ \hat{C}_n \tag{4.8}$$

where $\hat{C}_n^+$ and $\hat{C}_n$ are collapse operators, each corresponding to a separate irreversible process with rate γ_n. Here the strictly negative non-Hermitian portion of Eq. 4.8

gives rise to a reduction in the norm of the wave function, that to first-order in a small time δt is given by

$$\langle\psi(t+\delta t)|\psi(t+\delta t)\rangle = 1 - \delta p \tag{4.9}$$

where

$$\delta p = \delta t \sum_n \langle\psi(t)|\hat{C}_n^+ \hat{C}_n|\psi(t)\rangle, \tag{4.10}$$

and δt is such that $\delta p \ll 1$. With a probability of remaining in the state $|\psi(t+\delta t)\rangle$ given by 1 - δp, the corresponding quantum jump probability is thus Eq. 4.10. If the environmental measurements register a quantum jump, say via the emission of a photon into the environment, or a change on the spin of the ultracold ion, the wave function undergoes a jump into a state defined by projecting $|\psi(t)\rangle$ using the collapse operator $\hat{C}_n$ corresponding to the measurement

$$|\psi(t+\delta t)\rangle = \frac{\hat{C}_n|\psi(t)\rangle}{\sqrt{\langle\psi(t)|\hat{C}_n^+\hat{C}_n|\psi(t)\rangle}}. \tag{4.11}$$

If more than one collapse operator is present in Eq. 4.8, the probability of collapse due to the ith-operator $\hat{C}_i$ is given by

$$P_i(t) = \frac{\langle\psi(t)|\hat{C}_n^+\hat{C}_n|\psi(t)\rangle}{\delta p}. \tag{4.12}$$

When decoherence effects were not studied, the corresponding Schrödinger equation was solved numerically in the interaction picture. The time-independent part of the Hamiltonian ($\hat{H}_c$) is diagonal in the Fock basis $\{|i\rangle\}$, so it is straightforward to calculate the eigenvalues and eigenvectors . Since the eigenfunctions satisfy $\hat{H}|i\rangle = E_i|i\rangle$, we can propose the time-dependent basis

$$|i\rangle = e^{-iE_it/\hbar}|i\rangle. \tag{4.13}$$

Any wavefunction in this basis can be expressed as

$$|\psi(t)\rangle = \sum_i \psi_i(t)|i(t)\rangle = \sum_i \psi_i(t)e^{-iE_it/\hbar}|i\rangle, \tag{4.14}$$

and the time-dependent Schrödinger equation for the expansion coefficients $\psi_i(t)$ in the interaction picture is

$$\begin{aligned} i\hbar\dot{\psi}_i(t) &= \sum_j \psi_j(t)e^{-i(E_j-E_i)t/\hbar}\ cos(\Omega t)\langle i|\hat{H}_c|j\rangle = \\ &= \frac{1}{2}\sum_j \psi_j(t)[e^{-i(\frac{E_j-E_i}{\hbar}-\Omega)t} + e^{-i(\frac{E_i-E_j}{\hbar}-\Omega)t}]\ T_{ij}, \end{aligned} \tag{4.15}$$

where we have replaced $cos(\Omega t) = \frac{1}{2}e^{i\omega t} + \frac{1}{2}e^{-i\omega t}$ and defined

$$T_{ij} = \langle i|\hat{H}_c|j\rangle = \langle i|\frac{A\epsilon}{d^3}\ \hat{y}|j\rangle, \tag{4.16}$$

and

$$\hat{y} = \sqrt{\frac{\hbar}{m\omega_y}}\ \frac{(a^\dagger + a)}{\sqrt{2}}. \tag{4.17}$$

The time-independent matrix elements T_{ij} of the perturbation Hamiltonian are called transition matrix elements and describe how the populations of the ion vibrational levels (which are the eigenstates of the time-independent Hamiltonian) are coupled via the oscillating field that is generated by the nanowire drive.

The decoherence rate γ of the ion was assumed to be on the order of 4-10 Hz, which is the decoherence rate range of a typical Paul trap with a $^{40}Ca^+$ experiment. We also performed various calculations by assuming different ion decoherence rates from 20 to 60 Hz, which are values that are experimentally reasonable. We found that decoherence rates of this magnitude are small compared to the stronger driven dynamics of the system and barely have any effect on the present results. During the entire period covered in the calculations, we assume that the laser cooling of the ion is switched off and a constant drive is applied on the nanowire with a specific frequency and amplitude of oscillation.

As initial conditions in our calculations, we assume a $^{40}Ca^+$ ion cooled to the motional ground state of a trap with $\omega_y/2\pi = 600$ kHz axial frequency. The nanowire

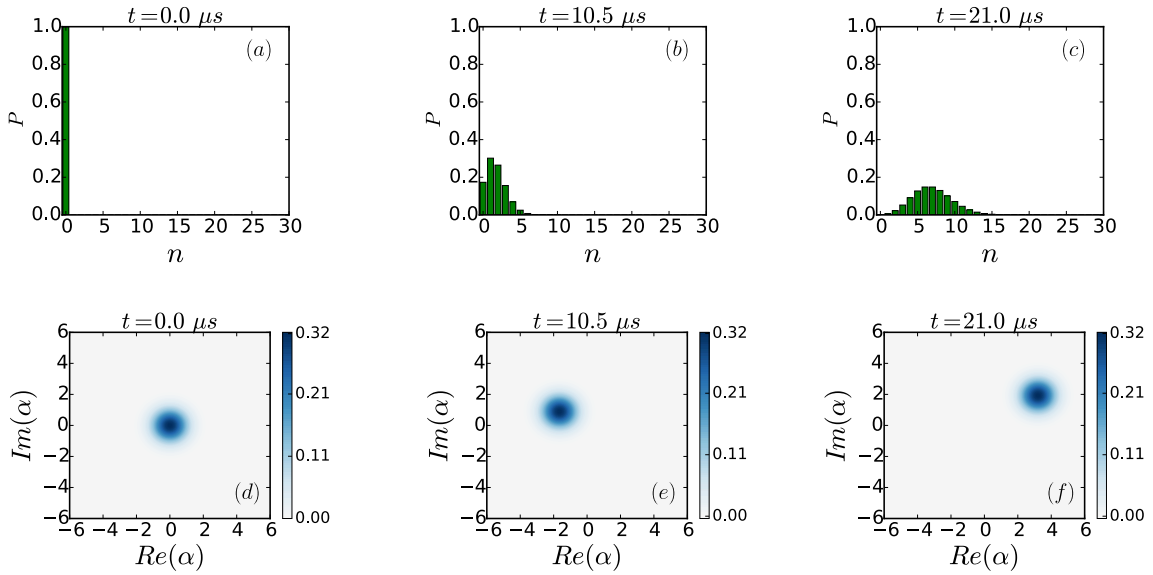

Figure 4.2: Evolution of ion vacuum state and creation of coherent state after the nanowire drive. The first row shows the sequential coupling of the ion Fock levels described by a Poisson distribution. The second row shows the quasi-probability phase-space representation (Wigner function) which illustrates the displacement of the ion vacuum state due to the motional coupling with the driven nanowire.

was fixed at a position 50 μm away from the ion along the z-axis and driven at 100 nm amplitude at $\omega_{nw}/2\pi = 600$ kHz. A voltage of 100 mV was applied. Figure 4.2 shows snapshots of the dynamics within the first 30 vibrational levels of the trap. Figures 4.2(a), 4.2(b) and 4.2(c) show the populations and figures 4.2(d), 4.2(e) and 4.2(f) show the Wigner functions at 0, 10.5 and 21 μs into the dynamics. The Wigner function (a phase-space quasi-probability distribution) is defined for an arbitrary density operator $\hat{\rho}$ as [147].

$$W(q,p) = \frac{1}{2\pi\hbar} \int_{-\infty}^{\infty} \langle q + \frac{1}{2}x \mid \hat{\rho} \mid q - \frac{1}{2}x \rangle \; e^{-ipx/\hbar} dx. \tag{4.18}$$

Given a density matrix in the Fock basis

$$\hat{\rho} = \sum_{n,m=0}^{\infty} \hat{\rho}_{n,m} |n\rangle\langle m|, \tag{4.19}$$

then the Wigner funciton can be written as

$$W(q,p) = \sum_{n,m=0}^{\infty} \hat{\rho}_{nm} \Omega_{nm}(q,p). \tag{4.20}$$

If we write $\alpha = \frac{q-ip}{\sqrt{2}}$ then Ω_{nm} is

$$\Omega_{nm} = \frac{(-1)^n}{\pi}\sqrt{\frac{n}{m}}(2\alpha)^{m-n}L_n^{m-n}(4|\alpha|^2)e^{-2|\alpha|^2}, \tag{4.21}$$

where the $L_n^{m-n}(z)$ are the generalized Laguerre polynomials.

In fig. 4.2 can be seen the evolution of the ground-state cooled ion vacuum state into a coherent state with increasing amplitude for longer time steps. For each snapshot, one sees the evolution of the coherent state represented in a Fock-basis distribution fig. 4.2(a),4.2(b),4.2(c) and in a quasi-phase-space representation (Wigner function) 4.2(d),4.2(e),4.2(f) at 0, 10.5 and 21 μs. The truncated Hilbert space consists of the first 30 vibrational levels of the ion, which are sufficient to describe the dynamics of the system for this time interval. While the nanowire mechanical drive is in effect, subsequent ion Fock levels are coupled and they form a superposition that can be described by a Poisson distribution which is one of the characteristic properties of coherent states. We see how the nanowire effect displaced the ion initial vacuum state by creating a coherent state with a mean phonon number $\bar{n} = 6.5$ within the first 21 μs, while the uncertainties of the created state are preserved to minimum values like in the initial vacuum state. Physically this means that the coherent motion of the driven nanowire is mapped onto the ion, which indicates that one can use the ion as an accurate probe for the nanomechanical motion.

Figure 4.3 shows the time evolution of the occupation probability of the first five ion vibrational levels due to the resonant coupling with the driven nanowire. The small oscillations appear due to the 6 kHz frequency missmatch between the two coupled systems, due to the small perturbation that the nanowire imposes on the ion harmonic potential based on the above parameters.

The coherent states are of significant importance due to many appealing properties (described below) that they have towards explanation of different quantum phenomena, like quantum coherence and quantum phase. It is easier to understand the properties of coherent states following the quantum theory of the electromagnetic field [147–149]. The time-dependent electric field operator reads

$$\hat{E}_x(t) = \mathcal{E}_0(\hat{a}e^{-i\omega t} + \hat{a}^\dagger e^{i\omega t})\sin(kz) \tag{4.22}$$

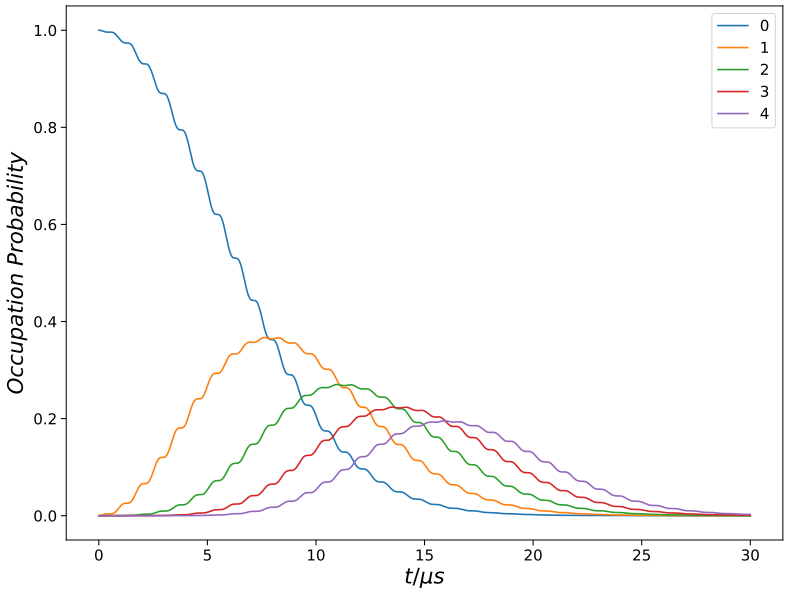

Figure 4.3: Occupation probability of the first five ion vibrational levels as a function of time. During the nanowire drive sequential ion Fock levels are coupled together leading to higher phonon excitation. The small oscillations appearing here are due to a small ion frequency shift after interacting with the nanowire.

where x is the polarization of the electromagnetic radiation and z is the direction of the travelling wave. The number state $|n\rangle$ is a state of well-defined energy but it is not a state of well-defined electric field since

$$\langle n|\hat{E}_x(z,t)|n\rangle = \mathcal{E}_0 \sin(kz)[\langle n|\hat{a}|n\rangle + \langle n|\hat{a}^\dagger|n\rangle] = 0. \tag{4.23}$$

This means that the mean field is zero. But the mean of the square of this field, which contributes to the energy density, is not zero:

$$\begin{aligned}\langle n|\hat{E}_x^2(z,t)|n\rangle &= \mathcal{E}_0^2 \sin^2(kz)\langle n|(\hat{a}^\dagger)^2 + \hat{a}^2 + \hat{a}^\dagger\hat{a} + \hat{a}\hat{a}^\dagger|n\rangle \\ &= \mathcal{E}_0^2 \sin^2(kz)\langle n|(\hat{a}^\dagger)^2 + \hat{a}^2 + 2\hat{a}^\dagger\hat{a} + 1|n\rangle \\ &= 2\mathcal{E}_0^2 \sin^2(kz)\left(n + \frac{1}{2}\right).\end{aligned} \tag{4.24}$$

The fluctuations in the electric field can be characterized by the variance

$$\langle(\Delta\hat{E}_x(z,t))^2\rangle = \langle\hat{E}_x^2(z,t)\rangle - \langle\hat{E}_x(z,t)\rangle^2 \tag{4.25}$$

or by the standard deviation

$$\Delta E_x = \langle (\Delta E_x(z,t))^2 \rangle^{1/2} \tag{4.26}$$

which is sometimes referred to as the uncertainty of the field. For the number state $|n\rangle$ we have

$$\Delta E_x = \sqrt{2\mathcal{E}_0}\ \sin(kz)\left(n+\frac{1}{2}\right)^{1/2} \tag{4.27}$$

Introducing the quadrature operators

$$\hat{X} = \frac{1}{2}(\hat{a}+\hat{a}^\dagger) \tag{4.28}$$

$$\hat{P} = \frac{1}{2i}(\hat{a}-\hat{a}^\dagger) \tag{4.29}$$

which represent the position and momentum quadrature operators in dimensionless form that is derived from their expression with the help of the creation and annihilation operators

$$\hat{a} = \frac{1}{\sqrt{2\hbar\omega}}(\omega\hat{q}+i\hat{p}) \tag{4.30}$$

$$\hat{a}^\dagger = \frac{1}{\sqrt{2\hbar\omega}}(\omega\hat{q}-i\hat{p}). \tag{4.31}$$

Thus the electric field operator from above can be recast with the help of the quadrature operators as

$$\hat{E}_x(t) = 2\mathcal{E}_0 sin(kz)[\hat{X}cos(\omega t)+\hat{P}sin(\omega t)]. \tag{4.32}$$

The position and momentum operators satisfy the commutation relation

$$[\hat{X},\hat{P}] = \frac{i}{2} \tag{4.33}$$

from which it follows that

$$\langle(\Delta\hat{X})^2\rangle\langle(\Delta\hat{P})^2\rangle \geq \frac{1}{16}. \tag{4.34}$$

For the number states we have $\langle n|\hat{X}|n\rangle = \langle n|\hat{P}|n\rangle = 0$ but

$$\begin{aligned}\langle n|\hat{X}|n\rangle &= \frac{1}{4}\langle n|\hat{a}^2 + (\hat{a}^\dagger)^2 + \hat{a}^\dagger\hat{a} + \hat{a}\hat{a}^\dagger|n\rangle \\ &= \frac{1}{4}\langle n|\hat{a}^2 + (\hat{a}^\dagger)^2 + 2\hat{a}^\dagger\hat{a} + 1|n\rangle \\ &= \frac{1}{4}(2n+1)\end{aligned} \tag{4.35}$$

and similarly

$$\langle n|\hat{P}^2|n\rangle = \frac{1}{4}(2n+1). \tag{4.36}$$

Thus for a given number state the uncertainties in both quadratures are the same and the vacuum state ($n = 0$) minimizes the uncertainty product since

$$\langle(\Delta\hat{X})^2\rangle_{vac} = \langle(\Delta\hat{P})^2\rangle_{vac} = \frac{1}{4}. \tag{4.37}$$

The number states $|n\rangle$ have a uniform phase distribution over the range 0 to 2π, which means that there is no well-defined phase for those states (including the vacuum state) and also the expectation value for the field operator for a number state vanishes. The classical limit of the quantized field has been suggested to be where the number of photons (or phonons) becomes very large such that the number operator becomes a continuous variable. However, the expectation value of the electric field operator in the mean field is zero, no matter how large is the number of photons. The coherent states give rise to a reasonable classical limit and that is the reason that these states are often referred as quasi-classical states of the quantum harmonic oscillator. For the rest of the chapter we will mention only the phonons since they are relevant to the ion-nanowire interaction, and the treatment is equivalent to that of photons for the quantized electromagnetic field.

In order to have non-zero expectation value of the electric field operator the requirement is to have a superposition of number states that only differ by ± 1, for example

$$|\psi\rangle = C_n|n\rangle + C_{n+1}|n \pm 1\rangle, \tag{4.38}$$

they have the property that the expectation value of the annihilation operator will not vanish and they are eigenstates of the annihilation operator. The states that

fulfill those requirements are the coherent states and if we denote them with $|\alpha\rangle$ the normalized expression of the coherent states is

$$|\alpha\rangle = \exp(\frac{1}{2}|\alpha|^2) \sum_{n=0}^{\infty} \frac{\alpha^n}{\sqrt{n!}} |n,\rangle \tag{4.39}$$

where α is a complex parameter and $|\alpha|$ is related to the amplitude of the field. The expectation value of the phonon number operator is

$$\bar{n} = \langle\alpha|\hat{n}|\alpha\rangle = |\alpha|^2 \tag{4.40}$$

and thus $|\alpha|^2$ is just the average phonon number of the field. The fluctuations of the phonon number is

$$\Delta n = \sqrt{\langle\hat{n}^2\rangle - \langle\hat{n}\rangle^2} = \bar{n}^{1/2} \tag{4.41}$$

which is characteristic of a Poisson process and the probability of detecting n phonons is

$$P_n = |\langle n|\alpha\rangle|^2 = e^{-|\alpha|^2} \frac{|\alpha|^{2n}}{n!} \tag{4.42}$$

which is a Poisson distribution with a mean of $\bar{n}$. The fractional uncertainty in the phonon number is

$$\frac{\Delta n}{\bar{n}} = \frac{1}{\sqrt{\bar{n}}} \tag{4.43}$$

which decreases with increasing $\bar{n}$.

For a coherent state $|\alpha\rangle$, with $\alpha = |\alpha|e^{i\theta}$ in polar form, the corresponding phase distribution is

$$\begin{aligned} \mathcal{P}(\phi) &= \frac{1}{2\pi}|\langle\phi|\alpha\rangle|^2 \\ &= \frac{1}{2\pi} e^{-|\alpha|^2} \left| \sum_{n=0}^{\infty} e^{in(\phi-\theta)} \frac{|\alpha|^n}{\sqrt{n!}} \right|^2 . \end{aligned} \tag{4.44}$$

For large $|\alpha|^2$, the Poisson distribution may be approximated as a Gaussian

$$e^{|\alpha|^2/2} \frac{|\alpha|^{2\pi}}{n!} \approx (2\pi|\alpha|^2)^{-\frac{1}{2}} \exp\left[\frac{(n-|\alpha|^2)^2}{2|\alpha|^2}\right] \tag{4.45}$$

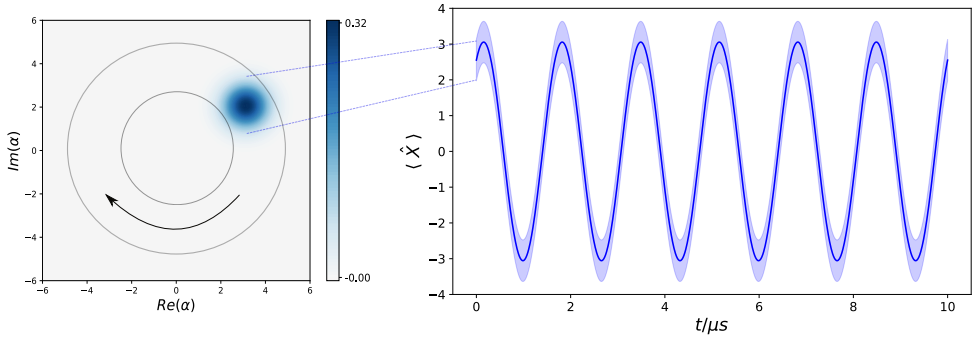

Figure 4.4: Left: Unitary evolution of an ion coherent state with mean phonon number $\bar{n} = 6.5$ a harmonic well of 600 kHz frequency. Right: Expectation value of the position quadrature (blue solid line) of the unitary evolution of the coherent state and the variance (blue shade) due to quantum uncertainties from the vacuum fluctuations within the first 10 μs.

so that the sum in Eq. 4.44 may be evaluated to obtain an approximate form for the phase distribution as

$$\mathcal{P}(\phi) = \left(\frac{2|\alpha|^2}{\pi}^{1/2}\right) \exp[-2|\alpha|^2(\phi - \theta)^2]. \tag{4.46}$$

One can see that this Gaussian is peaked at $\phi = \theta$ and that the peak becomes narrower with increasing $\bar{n} = |\alpha|^2$. All of those attributes of the coherent states summarize the reason that they are similar to the classical ones because (i) the expectation value of the electric field has the form of the classical expression, (ii) the fluctuations in the electric field variables are the same as for the vacuum, (iii) the fluctuations in the fractional uncertainty for the phonon number decrease with the increasing average phonon number, and (iv) the states become well localized in phase with increasing average phonon number.

Despite of the classical features that the coherent states have they are still quantum states, because they have uncertainties in both quadratures in their phase-space representation. For clarity, Figure 4.4 represents the coherent state generated from the nanowire drive as was seen in Figure 4.2 (c) at 21 μs. Then it is assumed that at this time step the drive of the nanowire is switched-off and the created coherent state with $\bar{n} = 6.5$ evolves in the same trapping harmonic potential without any other external field present.

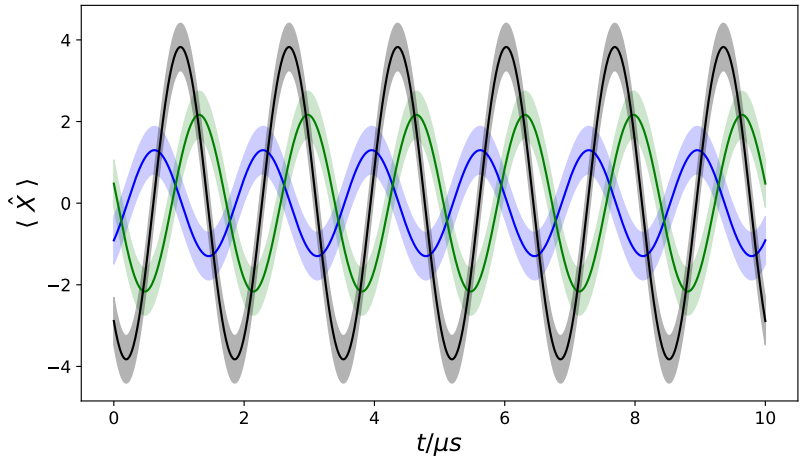

Figure 4.5: Expectation value of the position quadrature of three different coherent states during their unitary evolution in a harmonic well of 600 kHz frequency. The figure shows the coherent states that were created by switching-off the nanowire at 9 μs (blue solid line), 15 μs (green solid line) and 27 μs (black solid line) with $\bar{n} = 1.2$ (blue), $\bar{n} = 2.5$ (green), $\bar{n} = 10$ (black) and their corresponding quantum uncertainties. Coherent states of higher amplitude have smaller quantum uncertainties.

When a coherent state undergoes such unitary evolution in the harmonic potential, the centroid of this Gaussian wavepacket is moving clockwise in a circular fashion with constant amplitude, exactly as a point particle of a classical harmonic oscillator, as can be seen in Figure 4.4 (left) from the representation of the Wigner function. As we expect from the classical analog, the expectation value of the position quadrature Figure 4.4 (right) is a sinusoidal form and its frequency is the frequency of the ion trapping potential. Nevertheless, the uncertainties due to the vacuum fluctuations are present and they are represented as the blue shaded region in Figure 4.5, which is the variance around the motion of the centroid for the $\hat{X}$ quadrature. By driving the nanowire for longer time periods the ion coherent state is displaced further in the phase space picture with increasing amplitude. Figure 4.5 shows the unitary evolution of the $\hat{X}$ quadrature for three different coherent excitations with $\bar{n} = 1.2$ (blue solid line), $\bar{n} = 2.5$ (green solid line) and $\bar{n} = 10$ (black solid line), that were generated when the nanowire drive is switched-off after 9 μs, 15 μs and 27 μs.

As expected, the amplitude for the time-evolved position quadrature is higher for the more displaced coherent states, but also one can see that the uncertainties from the vacuum fluctuations are decreasing with increasing coherent excitations, and they start vanishing while the coherent states approach the continuum, where the coherent

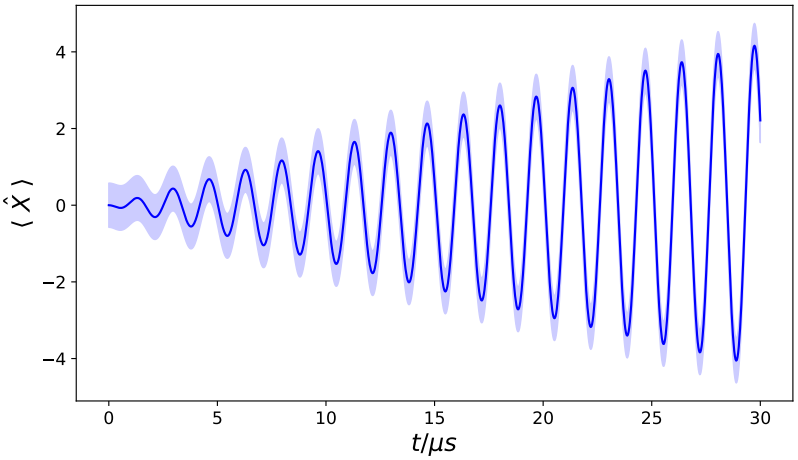

Figure 4.6: Expectation value of the position quadrature of the ion gaussian wavepacket as a function of time, during which the nanowire drive is constantly on. For longer excitation times higher amplitude coherent states are created while reducing their quantum uncertainties.

states resemble more to the classical ones. This potentially shows how one could explore classical to quantum transition phenomenae by mapping the coherent motion of the classical nanowire on the atomic ion. Moreover, the pure ion number states are not able to give phase information. By creating coherent states one can address a quantum phase as can be seen from the phase-space evolution in Figure 4.4, which is non-trivial and challenging from the experimental point of view. Figure 4.6 shows the time evolution of the expectation value and the corresponding variance of the position quadrature with continuous nanowire drive, that corresponds to gradually larger displacement and higher excitation of the initial vacuum state for the first 30 μs of the interaction. Again one clearly sees that with higher excitation the uncertainties due to vacuum fluctuations are decreasing.

When the frequencies of those two oscillators are not very close to each other, the nanowire cannot induce highly excited vibrational transitions on the ion. That is, even within the time interval as presented in Figure 4.2 and with only the first 30 vibrational levels considered, when the ion is detuned 50 kHz below the nanowire frequency the coupling is present only up to the 4th vibrational level. In that case the vacuum state is not displaced so much as can be seen by 4.7 where the evolution of the expectation value of the position operator is presented.

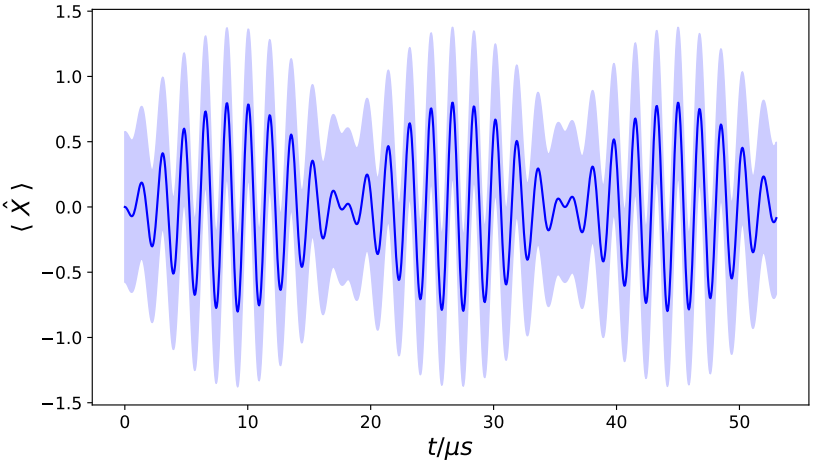

Figure 4.7: Expectation value of the position quadrature of the ion gaussian wavepacket when the ion frequency is 50 khz below the driving frequency of the nanowire. In this way weak pulses are created on the ion after the off-resonant nanowire drive with higher quantum uncertainties.

What is interesting is that when the ion is interacting off-resonantly with the nanowire it undergoes excitation and de-excitation, which resembles the pushing and pulling mechanism of a classical oscillator, and this is attributed to the in-phase and out-of-phase motion between the two oscillators. Those off-resonant dynamics show that even though the excitation is small one can alternatively create excitation pulses on the ion, which can be tuned according to the ion detuning. However, due to this frequency missmatch the tuning of the excitation pulses are limited to a few tens of kilohertz and the phase-space variance is increased which introduces larger quantum uncertainties.

Experimentally, the readout of the engineered quantum state of the ion can be performed with well-established techniques as reported in, e.g., [28, 30]. A two-state pseudo-spin system can be realized by addressing the $(4s)\ ^2S_{1/2} \rightarrow (3d)\ ^2D_{5/2}$ quadrupole transition in Ca^+ with a 729 nm laser. The blue sideband Hamiltonian for this transition reads [150]

$$\hat{H}_{bsb} = \frac{\hbar}{2}\,\Omega_0\eta(\hat{a}^\dagger\hat{\sigma}_+ + \hat{a}\hat{\sigma}_-), \tag{4.47}$$

where Ω_0 is the Rabi frequency, η is the Lamb-Dicke parameter, and $\hat{\sigma}_+$ and $\hat{\sigma}_-$ are the spin ladder operators. This Hamiltonian couples the motional and spin degrees of freedom of the ion. The experimental signal, i.e., the population in the lower spin

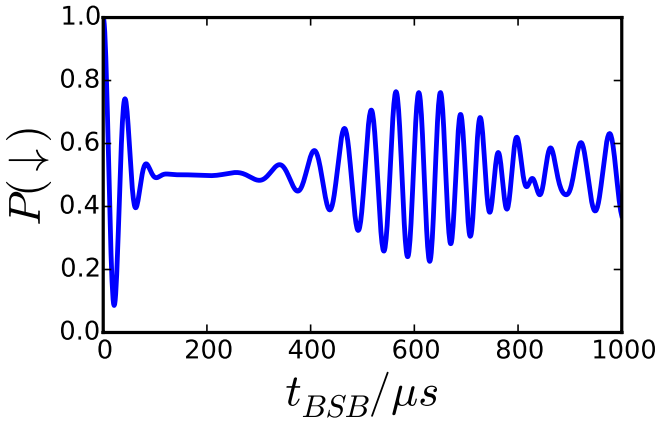

Figure 4.8: Blue sideband signal (population $P(\downarrow)$ of the laser spin state as a function of the blue sideband pulse duration t_{BSB}) produced by the $^{40}Ca^{+}$ coherent state corresponding to Figure 4.2(c).

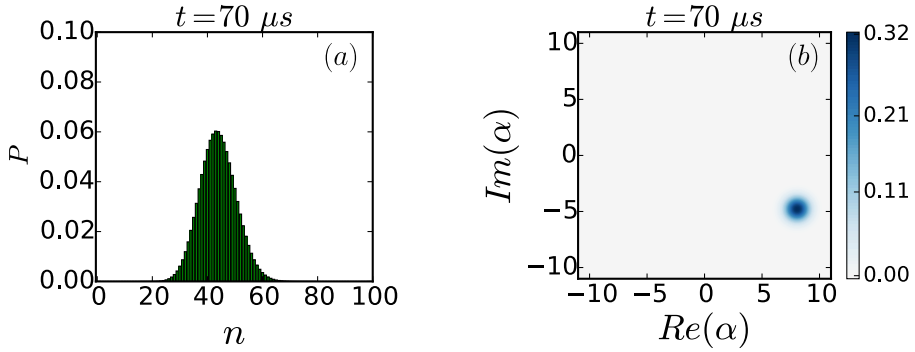

Figure 4.9: (a) Fock distribution and (b) Wigner function of a large coherent with $\bar{n}$=45 after 70 μs of mechanical drive on the ion.

state $P(\downarrow)$ produced by this interaction is shown in figure 4.8 where we assume a Rabi frequency of $\Omega_0/2\pi = 70$ kHz for the blue sideband oscillation.

This way of generating ion coherent states is similar to the one reported in [28], where an oscillating electric field was applied to one of the trap electrodes. In comparison, the case considered here of a static field applied to a nano-resonator may offer some advantages. One can tune the quantum state engineering dynamics on-the-fly by varying the position or voltage of the nanowire. Another advantage of this scheme is that the generation of ion quantum states is independent of laser of magnetic field fluctuations, since the nanowire interacts directly with the ion motional degrees of freedom, in contrast to the generation of coherent states with a laser field where the ion motional and spin degrees of freedom are coupled. A disadvantage of the optical field is that it interacts with an electric dipole or quadrupole moment of the atomic

ion and the oscillator states engineered in this way are typically limited to excitations of <20 quanta. The charged nanowire, on the other hand, acts directly on the electric monopole and therefore large-amplitude coherent states can be enginnered without the need of electronics for fast switching trapping potentials [151] as seen in Figure 4.9.

So far we have seen how one can map the nanowire coherent motion onto the ion at room temperature experimental conditions, with a near resonant drive and engineer Gaussian coherent states with only positive Wigner values. Nevertheless, non-Gaussian ion quantum states with negative Wigner values can be engineered with the same nanowire drive by employing trapping unharmonicities. In this case the Hamiltonian of equation 4.5 can be augmented with an additional anharmonic term and reads

$$\hat{\mathcal{H}}_{tot} = \omega(\hat{a}^\dagger\hat{a} + \frac{1}{2}) - s(\hat{a}^\dagger + \hat{a})^2 + g(\hat{a}^\dagger + \hat{a})\ \cos(\omega_{nw}t) + D(\hat{a}^\dagger + \hat{a})^4, \tag{4.48}$$

where D is the anharmonic Duffing term of the axial trapping potential. This term was introduced arbitrarily in the semi-classical treatment, in order to investigate the possibility of encoding quantum information from the nanowire to the ion, with negative Wigner values, applying the same nanowire drive.

Such anharmonicities may arise from different sources in an ion trap, like patch potentials or geometric asymmetries of the electrodes close to the trapping region. Additionally, one can engineer anharmonicities and consequently the Duffing term in Eq. (4.48) by varying the voltages on the DC electrodes [104]. As an example, figures 4.10(a) and 4.10(d) show the populations and figures 4.10(b) and 4.10(e) the Wigner functions of non-Gaussian states generated with a detuning of 10 and 30 kHz of the nanowire to the ion motional frequency, respectively, and introducing an anharmonicity of $D = 8$ kHz that corresponds to a DC voltage configuration $V_i = \{$ V_1, V_2,...,V_{14} $\} = \{10, 9, 0, 1.58, 0, 9, 10, 10, 9, 0, 1.58, 0, 9, 10\}$ V. The first row of figure 4.10, i.e. 4.10(a), 4.10(b) and 4.10(c), corresponds to the $^{40}Ca^+$ ion at 10 kHz axial detuning and the second row, i.e. 4.10(d), 4.10(e) and 4.10(f), corresponds to the $^{40}Ca^+$ ion at 30 kHz detuning. All of these figures show snapshots of the dynamics at the same time step of 18 μs. Figures 4.10(c) and 4.10(f) show the corresponding blue-sideband signal of the non-Gaussian states. Under these conditions, we see that

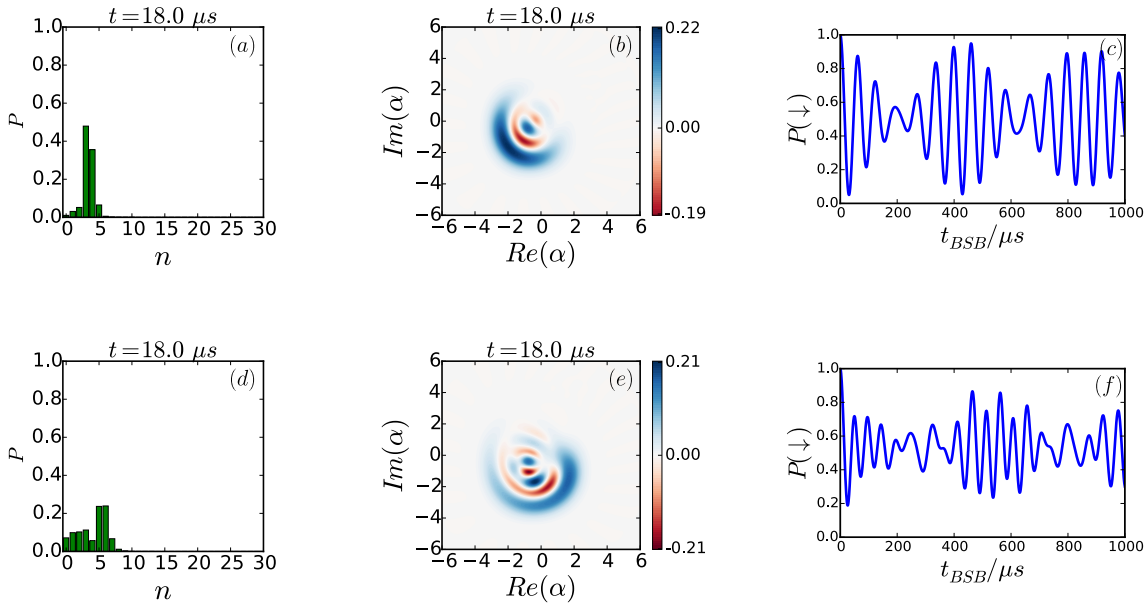

Figure 4.10: Fock distribution, Wigner function and blue sideband signal of the laser spin state under the effect of the anharmonic Duffing term with ion's frequency detuned by 10 kHz: (a), (b), (c) and by 30 kHz: (d), (e), (f).

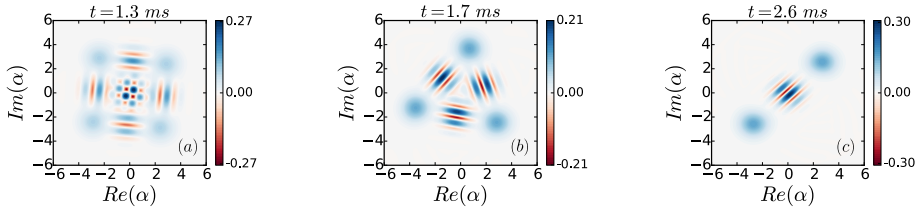

Figure 4.11: Wigner function of the unitary evolution of a coherent state under the effect of an anharmonicity term of strength $D = 100$ Hz. The initial wave-packet splits into (a) four, (b) three and (c) two parts (Schrödinger cat-type states).

the initial vacuum state is diffused and the appearance of the negative regions in the Wigner function is a signature of genuine quantum states, as compared to the quasi-classical Gaussian ones of figure 4.2.

Another way to create non-Gaussian quantum states is via their unitary evolution under anharmonic effects. Specifically, according to Figure 4.2c we assume that after 21 μs the nanowire voltage is switched-off and that there is an anharmonic term of the ion trapping potential with strength $D = 100$ Hz. Thus, the engineered coherent state evolves freely in the trapping potential under the anharmonic effect of 100 Hz. Figure 4.11 shows the unitary evolution of the initial coherent state under the aforementioned anharmonic effects. One can see that the initial Gaussian wavepacket splits into four, three and two parts generating those intermittent Schrödinger cat-states with

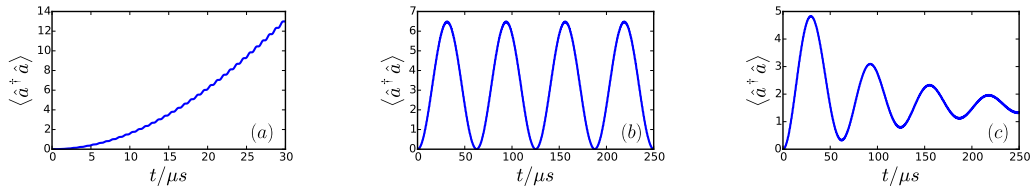

Figure 4.12: Phonon dynamics for (a) on-resonance, (b) with a 10 kHz detuning between the ion motional and nanowire frequency including the nanowire continuous drive and (c) the same as (b), but with nanowire dissipation.

the corresponding interference between the Gaussian parts. However, the Fock-state distribution of those intermittent states is the same as with the initial coherent state as in Figure 4.2 (c). This effect makes those states experimentally undetectable with a blue sideband pulse which is directly connected to the Fock-state distribution but not to the phases of the quantum states. An experimentally feasible detection mechanism would require quantum state tomography [152] and complete reconstruction of the density matrix of the states for each corresponding time-step. Those quantum states have attracted a lot of attention for quantum entanglement and quantum information processing experiments [29, 30, 153–158].

Concluding the dynamics of the system with a nanowire at room temperature, we investigated the ion phonon dynamics under the action of the oscillating nanowire detuned from resonance for a continuous drive and taking into account the nanoresonator dissipation. In figures 4.12 (a), (b) and (c), the mean phonon number for (a) a resonant drive, (b) a detuning of 10 kHz between the ion and the nanowire frequencies under a continuous drive, and (c) a detuning of 10 kHz and including the attenuation of the nanowire are shown. The attenuation of the nanowire is included as an exponential decay of its amplitude with a rate of 10 kHz. With this detuning, not more than 20 phonons of the ion can be excited, and a good description is achieved by including the first 30 vibrational levels in the Hilbert space. On resonance, the excitation is so strong that the nanowire excites more and more phonons. For the off-resonant case, we observe that the ion experiences excitation and de-excitation, which is due to alternating in-phase and out-of-phase motion between the ion and the nanowire. This shows that even at room temperature, one can use the ion as a probe for the nanowire's motion and experimentally study phase shifts and dissipation mechanisms of mesoscopic systems.

4.4 Quantum dynamics

When both oscillators operate in the quantum regime, as would be the case in a cryogenic experiment in which the nanowire is cooled close to the quantum-mechanical ground state of one or several of its modes, different dynamics are taking place. At cryogenic temperatures, we can describe the nanowire's motion with ladder operators in the Fock space and now the fully quantized Hamiltonian for the coupling between the nanowire and the ultracold ion reads

$$\begin{aligned} \hat{\mathcal{H}}_{coupling} &= g(\hat{a}^\dagger + \hat{a})(\hat{b}^\dagger + b), \\ \text{with } g &= \frac{\hbar\epsilon}{2d^3}\frac{1}{\sqrt{mM}}\frac{1}{\sqrt{\omega\ \omega_{nw}}}. \end{aligned} \tag{4.49}$$

Here, g is the coupling strength, $\epsilon = k_c Q_1 Q_2$ and d is the relative distance between the tip of the nanowire and the ion. m, ω and M, ω_{nw} are the mass and the oscillation frequency of the ion and the nanowire, respectively. We see that the coupling strength is inversely proportional to the product of the masses of those two systems. Conventional metallic nanowires exhibit very high masses ($M \approx 10^{-14}$ kg) compared to single ions which renders the coupling between the two systems very small. This can be mitigated by using carbon nanotubes instead ($M \approx 10^{-20} - 10^{-23}$ kg), which are very good conductors in specific configurations [159, 160]. The second dominant limitation towards achieving strong coupling is the mechanical decoherence rate of the nanowire caused by its coupling to the bath. A nanowire with a mechanical Q-factor of 300'000 and an oscillation frequency of $\omega_{nw}/2\pi = 600$ kHz has about 10^5 motional quanta of thermal excitation when it is coupled to a bath with a temperature of 4.2 K. The thermal decoherence rate of the nanowire is given by $\gamma_{nw} N_{nw} = k_b T/\hbar Q_{nw}$ where k_B is the Boltzmann constant and T is the bath temperature. The mechanical quality factor is given by $Q_{nw} = \omega_{nw}/\gamma_{nw}$ where γ_{nw} is the mechanical decoherence rate of the nanowire due to its coupling with the bath. This corresponds to a thermal decoherence rate of around 300 kHz for the nanowire. With these assumptions, the Lindblad master equation of the coupled system

$$\begin{aligned} \frac{d\hat{\rho}}{dt} = &-\frac{i}{\hbar}\,[\hat{\mathcal{H}}_{eff}, \hat{\rho}] + \gamma_{ion}^{heating}\ \hat{\mathcal{L}}[\hat{a}^\dagger]\hat{\rho} + \gamma_{ion}^{cooling}\ \hat{\mathcal{L}}[\hat{a}]\hat{\rho} \\ &+ \gamma_{nw}(N_{nw}+1)\ \hat{\mathcal{L}}[\hat{b}]\hat{\rho} + \gamma_{nw} N_{nw}\ \hat{\mathcal{L}}[\hat{b}^\dagger]\hat{\rho} \end{aligned} \tag{4.50}$$

was solved numerically. Here, $\gamma_{ion}^{heating}$ is the heating rate of the ion in a trap, $\gamma_{ion}^{cooling}$ is the cooling rate of the ion from the interaction with the cooling laser. The total effective Hamiltonian of the system is

$$\hat{\mathcal{H}}_{eff} = \hbar\omega(\hat{a}^\dagger\hat{a} + \frac{1}{2}) + \hbar\omega_{nw}(\hat{b}^\dagger\hat{b} + \frac{1}{2}) + g(\hat{a}^\dagger + \hat{a})(\hat{b}^\dagger + \hat{b}). \tag{4.51}$$

Choosing the parameters $m = 6.6 \times 10^{-26}$ kg, a conservative value of $M = 6.6 \times 10^{-20}$ kg, $\omega/2\pi = \omega_{nw}/2\pi = 600$ kHz, $d = 50$ μm and a voltage of $V_{nw} = 100$ mV on the nanowire, the coupling strength between the ion and the nanowire is $g/2\pi = 37$ Hz. The mass ratio between the ion and the nanowire should be at most $m/M = 10^{-6}$ for a coupling between the two systems to be feasible at this magnitude. The frequency shift of the nanowire caused by the ion is negligible and was omitted from the calculations. The frequency shift of the ion caused by the nanowire at the chosen parameters is 6 kHz. Thus, a 6 kHz detuning was assumed for the ion in order to match the frequencies of the two oscillators in order to study the resonant case. An intriguing possibility in this regime is the sympathetic cooling of the nanowire by the ion. The cooperativity parameter, given by $C = 4g^2/\gamma_{ion}\gamma_{nw}$, should be $C > 1$ in order for sympathetic cooling of the nanowire to be feasible [161]. For a bath temperature of $T = 4.2$ K which can be achieved with standard cryostats and $g/2\pi = 37$ Hz, $\gamma_{ion}/2\pi = 4$ Hz, $\gamma_{nw}/2\pi = 300$ kHz, one calculates $C = 0.0047$. Consequently, at 4.2 K bath temperature and such a big mass mismatch, the coupling is very weak, and neither coherent dynamics nor sympathetic cooling of the nanowire should be observable under these conditions. Coherent dynamics can only be observed at much lower temperatures. Indeed, we found that when the temperature is above 500 μK, the nanowire essentially behaves like a classical object vis-a-vis the ion.

This behaviour changes at very low temperatures of the nanowire. Figures 4.13(a) and (b) show the coherent phonon dynamics of the hybrid system with and without continuous sideband cooling of the ion, respectively, at a nanowire bath temperature of $T = 100$ μK and all other parameters kept the same as before. It should be noted that such a bath temperature is close to the current state of the art at 150 μK [162], but will be extremely challenging to achieve as it is about two orders of magnitude lower than what can be achieved in commercially available dilution refrigerators.

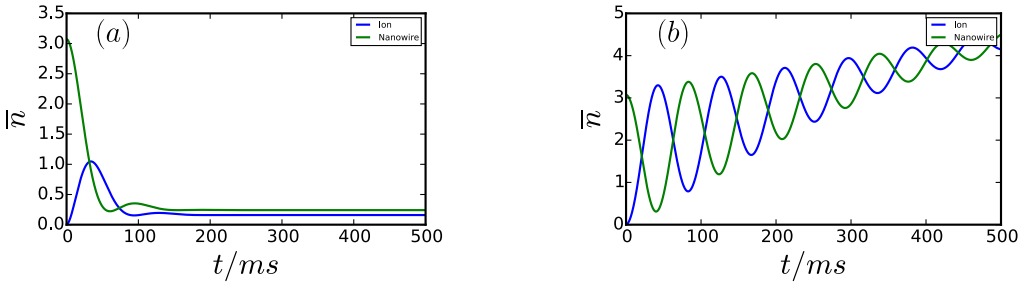

Figure 4.13: Phonon dynamics for (a) an ion-nanowire system with continuous cooling of the ion and (b) the same with no ion cooling in the quantum regime. See text for details.

It can be seen from figure 4.13(a) that the nanowire is sympathetically cooled from a single ultracold $^{40}Ca^{+}$ within the first 60 ms with a cooling rate of 0.05 quanta/ms. Figure 4.13(b) shows the energy swap between the nanowire and the ion. In the absence of an ion cooling mechanism, the coherent phonon dynamics is more clearly manifested. Eventually both systems equilibrate with the bath reaching an average of approximately 4 phonons each.

Moreover, every time that the system undergoes an energy swap as shown in figure 4.13(b), there is a transfer of the quantum state between the ion and the nanowire as is shown in figure 4.14. Figures 4.14(a) and (b) show the initial Wigner functions of an ultracold ion and a nanowire in the zeroth and fourth Fock states, respectively. Figures 4.14(c) and (d) show the relevant Wigner function after 41 ms of interaction time, after which one cycle of energy swap has occurred according to figure 4.13(b). It can be seen that the states of the ion and the nanowire have essentially been exchanged. The different intensities of the Wigner functions and the slightly larger spread of the vacuum state of the nanowire compared to the initial states are attributed to the thermal decoherence of the hybrid system. We expect to see the same type of behavior for various initial quantum states for both of the systems including Fock, coherent, squeezed and thermal states. Therefore, this interaction allows us to create a specific quantum state in one of these two systems and read it out from the other. In this fashion one can encode the quantum information from one system to the other, or alternatively to reconstruct the quantum information passed in one of the two systems. This might be an interesting approach for studying decoherence

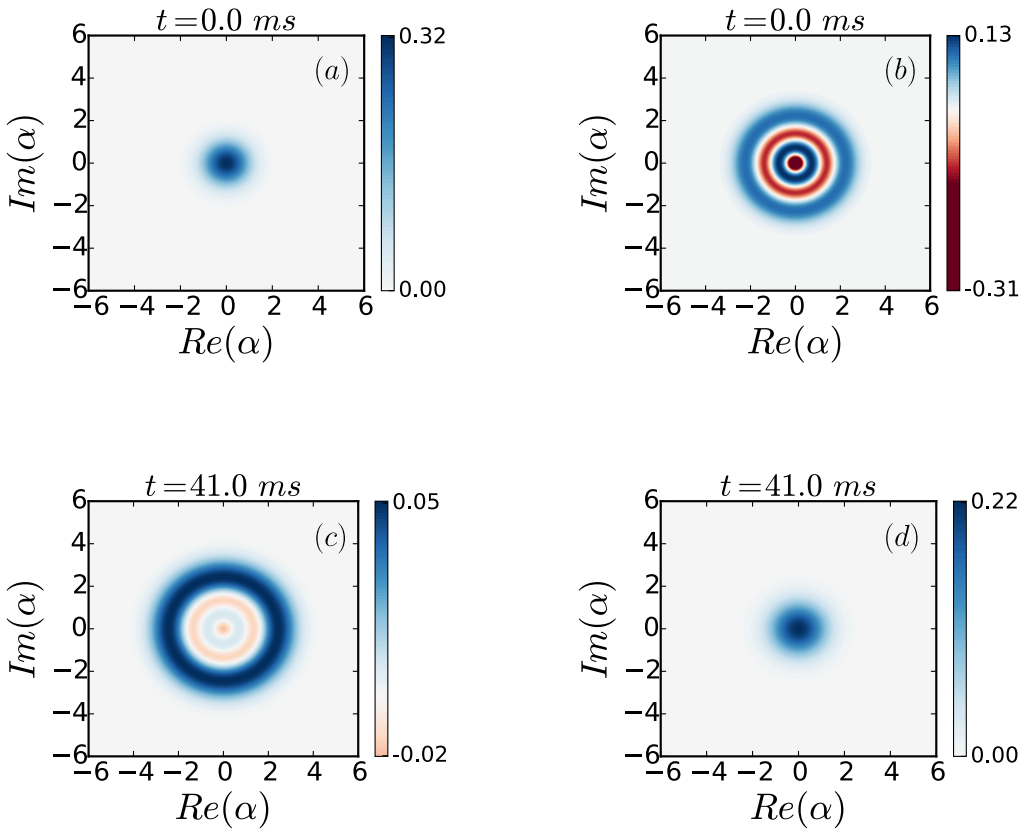

Figure 4.14: (a), (b): Wigner functions of the initial states of a ground-state cooled ion, i.e., $n = 0$, and a nanowire in the fourth Fock state $n = 3$, respectively. (c), (d): Wigner functions of the swapped states of the ion and the nanowire respectively after 41 ms of interaction at 100 μK bath temperature and 37 Hz coupling strength. The two systems have swapped their initial quantum states at this point in time.

mechanisms or creating quantum gates between solid-state and ionic systems, and quantum information interfaces, opening up possibilities for new quantum devices.

Chapter 5

Experimental Techniques and Characterization Measurements

Every force microscopy application that involves mechanical resonators primarily relies on the detection of the motion of the resonator. In conventional scanning probe setups, the displacement readout is mainly carried out either optically or electrically. In the first case, the deflection of a laser beam that is reflected by the backside of an AFM cantilever is detected [163], while in the second the piezoelectric signal that is produced by a resonating quartz tuning fork is measured [164, 165].

With the advancement of fabrication techniques, nano-mechanical resonators, like nanowires and nanotubes, were implemented and a variety of new techniques has risen for single and doubly clamped beams. In the latter case, doubly clamped resonators were integrated in electronic circuits, so that their mechanical displacement was measured as a modulation in the frequency of a microwave cavity [166, 167] or the AC-current flowing through the resonator [75, 168].

In general, the displacement of a nano-resonator can be probed via the recording of the modulation of a focused laser beam which interacts with the resonator. There are mainly three techniques that stand out in this fashion: measurement of the free electrons using scanning electron microscopy [169, 170], by measurements in which either the transmitted [171, 172] or the reflected part [74] of the laser is collected and by fiber-optic interferometry [1, 73, 173, 174]. Although fiber-optic interferometry is more compact and mechanically robust, while still providing high sensitivity, we chose to record the transmitted laser light after its interaction with the resonator,

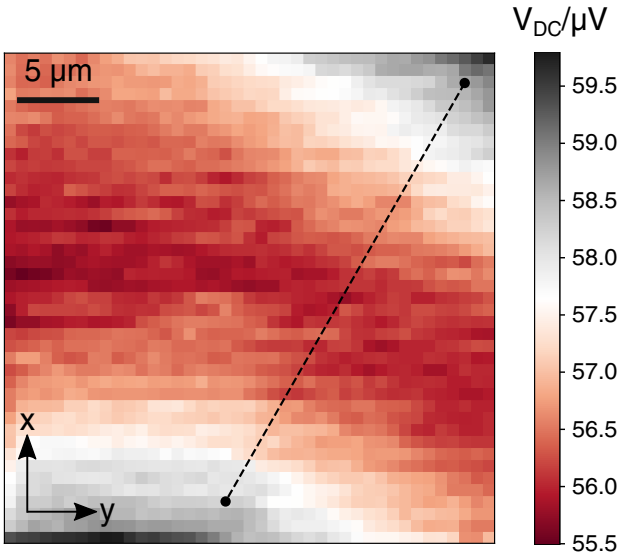

Figure 5.1: Measured 2D map of the aggregated transmitted 866 nm light intensity as a function of the nanowire position in the beam waist, with an incident power of 50 μW. The black dashed line is a cut across the laser beam, vertical to the direction of propagation, where we fitted a Gaussian function in order to estimate the 866 nm beam diameter, as shown in Fig. 5.2

due to our free-space optical setup and the large distances between the nanowire and the objectives for focusing and collecting the light. That imposed limitations on the readout of the nanowire, but as we will see in this chapter it was still possible to detect its driven motion.

5.1 Nanowire-Laser Alignment

As a first step for the optomechanical detection of the nanowire motion, we focused the 866 nm laser beam and aligned it on the nanowire itself. Typically, on a nanowire-sensing experiment the beam diameter on the nanowire varies between 550 nm and 2μm. In our experiment the focusing and collecting objective lenses were located outside the chamber at a distance approximately 20 cm from the nanowire. The estimated beam diameter on the nanowire, based on Gaussian beam optics, was approximately 12 μm. In order to have a more accurate description of the beam waist that is focused on the nanowire and of the nanowire position with respect to the beam waist, a technique similar to confocal microscopy was used. With our configuration the aggregated (SUM) and differential (DIFF) signal of the laser beam, transmitted

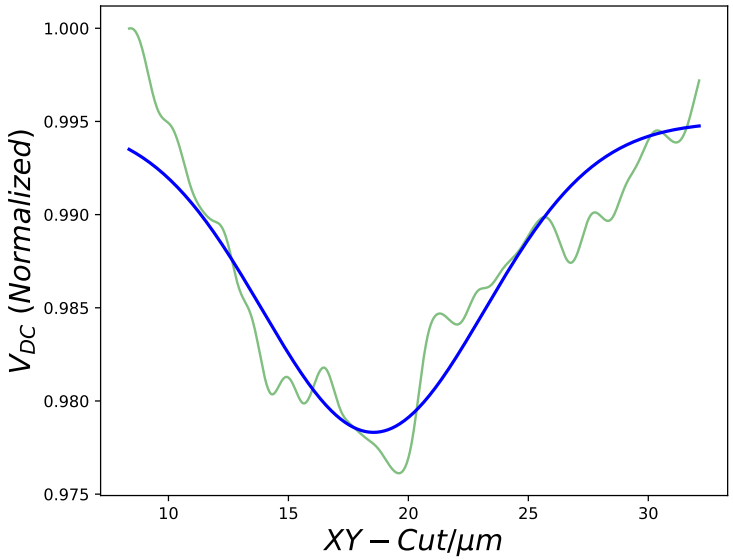

Figure 5.2: One-dimensional cut of the 2D intensity map. The normalized data of the DC voltage as a function of the distance in xy-plane are shown in green and the Gaussian fit to the data is shown in blue.

from the nanowire and detected from a segmented photodiode, was obtained. All of the following data were collected by recording only the SUM signal of the photodiode. More specifically, the nanowire was scanned in the beam waist region in the xy-plane and the DC component of the transmitted signal was recorded with the quadrant photodiode. Thus, the intensity map of Fig. 5.1 was generated, showing the 866 nm laser beam waist on a 30 $\times$ 30 μm window.

The y-direction is the symmetry axis of our trap and the x-direction is one of the two radials. this 2D-map shows that the incident beam was at approximately 35° with respect to the the symmetry axis of our trap. A Gaussian function was fitted to the data of a 1D-cut that was taken vertically across the direction of the beam as shown in Fig. 5.1 with the black dashed line connecting the two black points. Fig. 5.2 represents the 1D-cut from the 2D intensity map along with the Gaussian fit of the normalized DC signal giving 10 $\pm$ 0.25 μm beam diameter, which is very close to the estimated one from the Gaussian beam optics calculations. With the combination of these plots the nanowire can be placed accurately at a specific position in the beam. For high-sensitivity experiments, the position of the nanowire is chosen where the slope of the Gaussian laser beam is steeper [175].

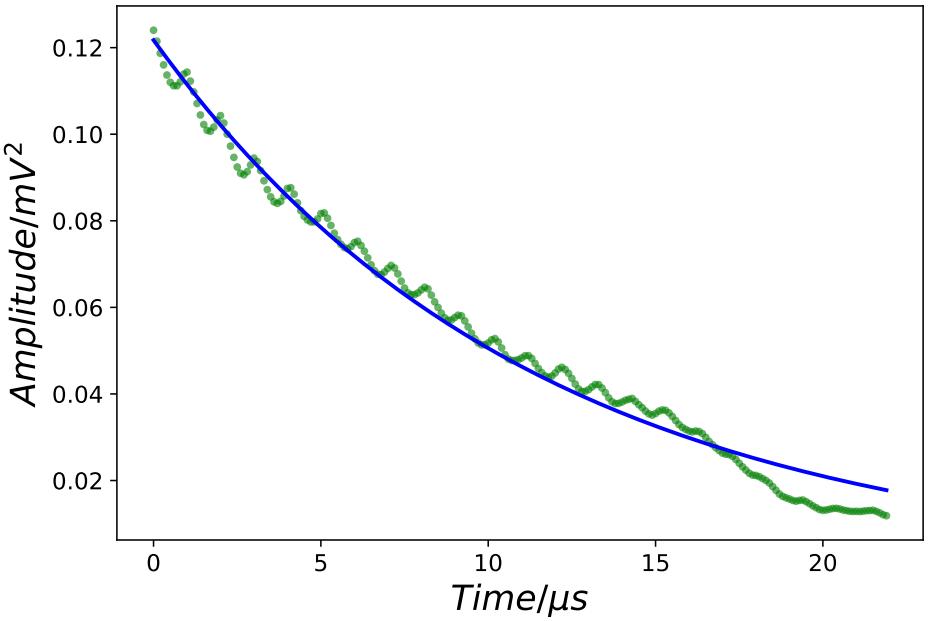

Figure 5.3: Ring-down measurement after the excitation of the nanowire at 489.4 kHz. The amplitude as a function of the decay time is represented by green dots and the exponential decay fit with the blue line.

5.2 Nanowire motional spectrum

Nanowire mechanical properties can be observed mainly and more efficiently by measuring their thermal motion. In our experiment that was not possible due to three major limitations, the bath temperature at 300 K, the relatively low quality factor of our conductive nanowires and the relative big laser diameter for readout. The Q-factor of the nanowire was measured with a ring-down technique as can be seen in Fig. 5.3, where the exponential decay of the excited nanowire at 489 kHz is shown. The two frequency response peaks of this nanowire were at 498 kHz and 615 kHz. This nanowire was destroyed later in the process, and was replaced by a similar one from the same batch. By fitting an exponential decay function to the data, we measured the decay time to be 11.38 μs. Using the Q-factor relation

$$Q = \frac{\tau\omega_0}{2}, \tag{5.1}$$

where τ is the exponential time constant and $\omega_0 = 2\pi f_0$, the calculated Q-factor was 17.5. If the measurement was performed at cryogenic temperatures, we would probably see a one order of magnitude higher quality factor. This Q-factor is considered

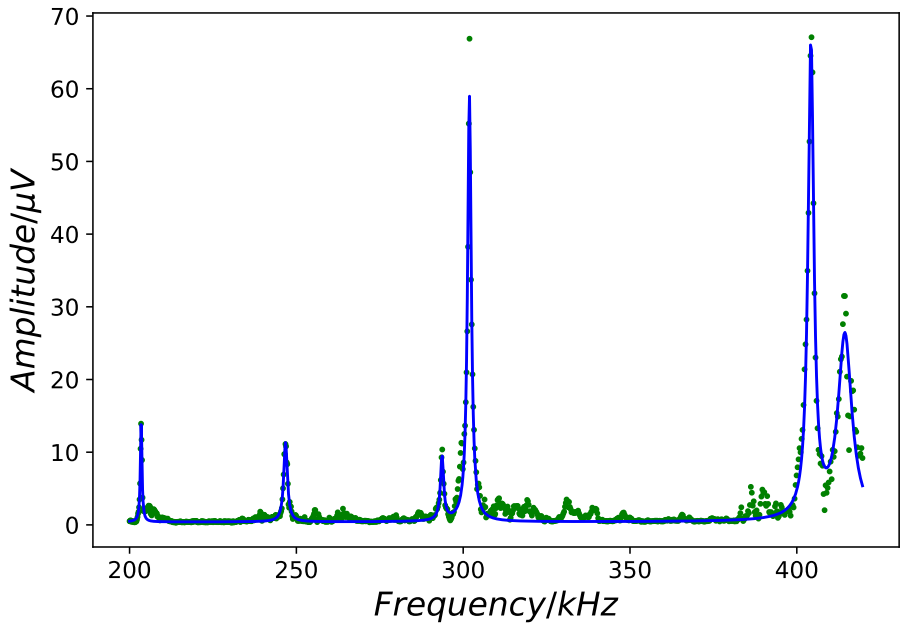

Figure 5.4: Frequency response of the driven nanowire showing six major peaks. The experimental data are represented with green dots and the Lorentzian fit is represented with blue line.

low for quantum sensing experiments, but the hybrid dynamics described in this work can still be investigated experimentally with a driven nanowire, where the Q-factor does not play a significant role. An alternative choice of a conductive nanowire that has the benefit of very low mass are carbon nanotubes, that they are expected to have much higher Q-factors. This could be an upgrade for this apparatus in the future.

Although the Q-factor was low and we could not measure the thermal motion of the nanowire, we were able to obtain information of the mechanical motion from the driven nanowire. In this setup, we used a voltage-controlled piezoelectric transducer that was attached on the same holder where the nanowire was mounted. The piezo was responsible to drive the oscillatory bending motion of the nanowire at a specific amplitude based on the voltage of the output waveform. The transmitted 866 nm laser light was modulated from the driven nanowire, collected on a quadrant photodiode and the response of the photodiode was demodulated by a lock-in amplifier[1]. The piezoelectric transducer was actuated by one of the oscillators of the same lock-in amplifier.

[1]Zurich Instruments: HF2LI 50 MHz Lock-In Amplifier, https://www.zhinst.com/

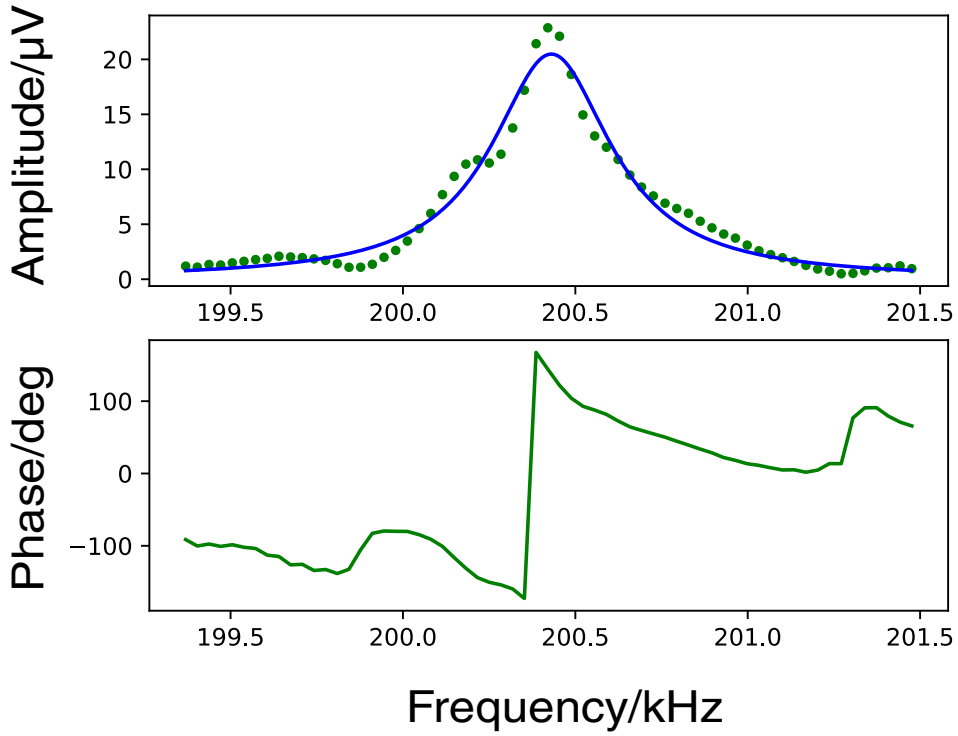

Figure 5.5: Top: Frequency peak of the driven nanowire, showing with green points the experimental data and with blue line the Lorentzian fit. Bottom: The measured phase of the same frequency response of the nanowire.

Fig. 5.4 shows the frequency response of the driven Ag_2Ga nanowire with an amplitude output waveform of 2 V, for a frequency sweep window between 200 and 410 kHz. Each point is the average of 20 measurements.

Usually, one expects two frequencies corresponding to the two modes of oscillations of the nanowire, when the two modes are not fully degenerate. Instead, we observed multiple peaks, that they are the result of various mechanical modes from the nanowire, where the smaller amplitude peaks are probably mechanical modulations on the nanowire motion that they arise either from the nanopositioners, the frame or other sources from the assembly. It is definite, though, that none of those peaks belong to the tungsten wire support of the nanowire. The tungsten wire had 100 μm diameter and its initial length was 15 mm. The Young's modulus of the tungsten is 411 GPa and the mass density is 19.3 g/cm^3. Plugging in those values in the eigenfrequency expression of the Euler-Bernoulli theory for cylindrical cantilevers 2.48 we get 1.8 MHz for the first mode of oscillation. Moreover, during the installation of the nanowire on the top part of the nanopositioners, we reduced the length

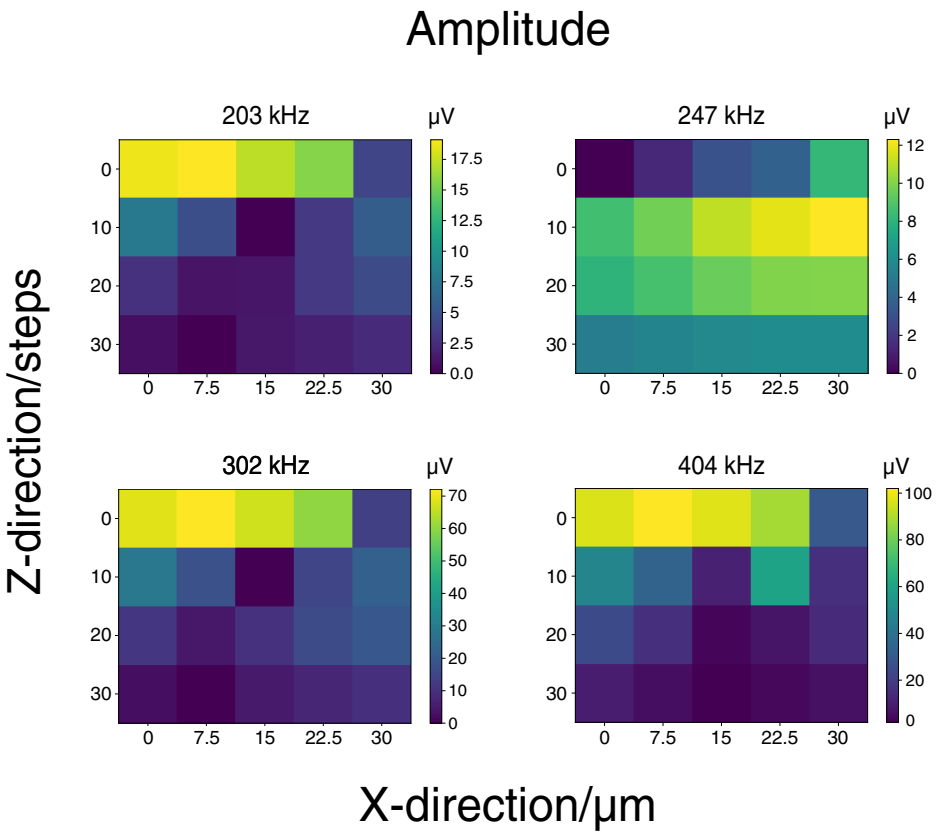

Figure 5.6: Two dimensional matrices representing the amplitudes of four peaks in Fig. 5.4 as a function of the z-position (measured in nanopositioner step) and of x-position (in μm) of the nanowire.

of the tungsten wire to approximately 8 mm. We have, also, seen under the optical microscope that the top part of the tungsten wire gets narrower down to the nanowire diameter dimensions, and this effect can be described mechanically as you reduce the load of the top part of a cantilever. Both of those effects indicate that according to the Euler-Bernoulli theory the expected eigenfrequencies of the tungsten cantilever are even higher than 1.8 MHz. Consequently, we can exclude with certainty the effect of the tungsten support from the nanowire mechanical spectrum.

The nanowire under this drive was still in the linear regime and the peaks shown in Fig. 5.4 were fitted to Lorentzian functions, in order to extract detailed information on their peak center, amplitude and width. With a lock-in measurement the phase that corresponds to a specific frequency can be measured as shown in Fig. 5.5.

One of the techniques used in this work to identify the nanowire motional peaks was to scan the nanowire in the xz-plane while measuring each individual peak in the spectrum 5.4. From the Lorentzian fits of each peak we calculated the amplitude and Q-factor as a function of the 2D-scan, which is shown in Fig. 5.6 and 5.7 respectively.

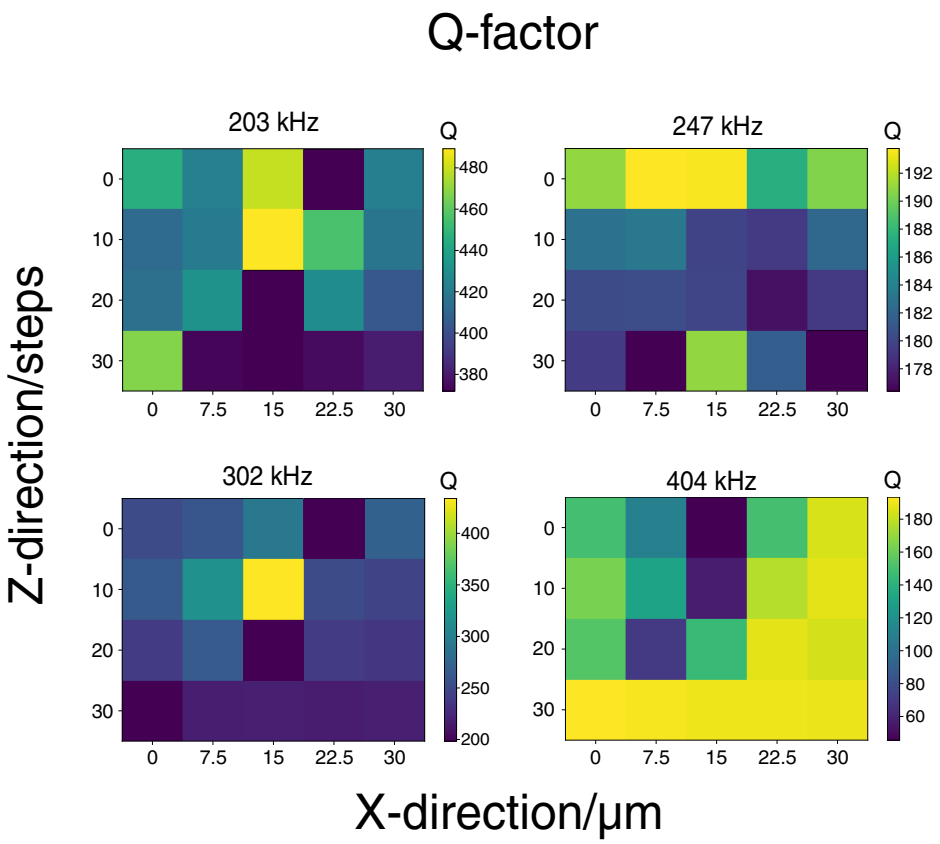

Figure 5.7: Two dimensional matrices showing the Q-factor values of four peaks in Fig. 5.4 as a function of the z-position (measured in nanopositioner step) and in x-position (in μm) of the nanowire.

From the frequency response of the nanowire we assumed that the two peaks that correspond to the two orthogonal modes of the first mode-shape are the ones at 302 and 404 khz. This assumption is based on the fact that the frequency split of the modes of the first nanowire was approximately 126 kHz, which is almost the same frequency difference between the two largest peaks of Fig. 5.4 at 302 kHz and 404 kHz. Additionally, the amplitude of those peaks indicate higher amplitude of oscillation, which means that the vibrations from the frame can be excluded as a possibility. Moreover, according to Fig. 5.6 the amplitude of the 203 kHz and 302 kHz are fully correlated. This means, in principle, that the 203 kHz frequency probably arises from a modulation on top of the nanowire motion and is coupled to the 302 kHz mode. That explains the identical spatial dependence on the amplitude of those two peaks. In this scanning window, we observe that there are regions where the amplitudes are very low or zero and others where they are relatively high. This is an expected behaviour for the nanowire modes of oscillation, as it moves to regions of the laser beam of varying

intensity and field gradient, which results in different detection sensitivity. In a typical nanowire measurement, especially when the thermal motion is measured, one expects from the two nanowire orthogonal modes one to increase in amplitude while the other is decreasing. This effect is connected to the position of the nanowire with respect to the laser beam and is observed due to the change of sensitivity according to the direction of oscillation of each mode. However, in Fig. 5.6 this is not clear between the 302 kHz and 404 kHz peaks. This is probably attributed to the fact that our beam diameter is relatively large comparing to typical nanowire experiments, which reduces the sensitivity of the measurement. As the beam moves downwards along the z-direction, away from the tip of the nanowire, one can see in Fig. 5.6 a reasonable spatial dependence on the amplitude of the 202 kHz, 302 kHz and 404 kHz peaks, but not from the one at 247 kHz. This indicates once more that probably the 302 kHz and 404 kHz peaks belong to the two orthogonal modes of the nanowire, the 202 kHz peak is a modulation that is coupled primarily to the 302 kHz mode, and the 247 kHz peak can be neglected for the analysis of the nanowire motion.

Fig. 5.7 represents the Q-factor values for the aforementioned four peaks as a function of the nanowire position of the same 2D-scanning window. The 302 kHz and 404 kHz peaks show the more stable values for the total scanning region, where the Q-factor is measured as the peak frequency over the FWHM of each peak. One can see that for the 302 kHz mode the Q-factor is approximately 250 and for the 404 khz mode is approximately 200. The 203 kHz peak show again correlation features with respect to the 302 kHz one, and it is probably a mechanical modulation as already mentioned above.

An alternative way to verify the nanowire modes is to drive it sequentially at increasing amplitude. When the excitation is high enough then the nanowire motion reaches the non-linear regime, and the frequency response peaks appear with the characteristic shark-fin shape [176]. We drove the nanowire in relatively high excitations, but he haven't observed any non-linear response.

Lastly, Fig. 5.8 shows the initial nanowire frequency response as shown in Fig. 5.4 (in grey) and the measurements that we took for the same frequency scanning region (in blue) after operating the calcium oven during the ion trap tests for some weeks. We observed a general frequency shift of the four mechanical peaks towards lower

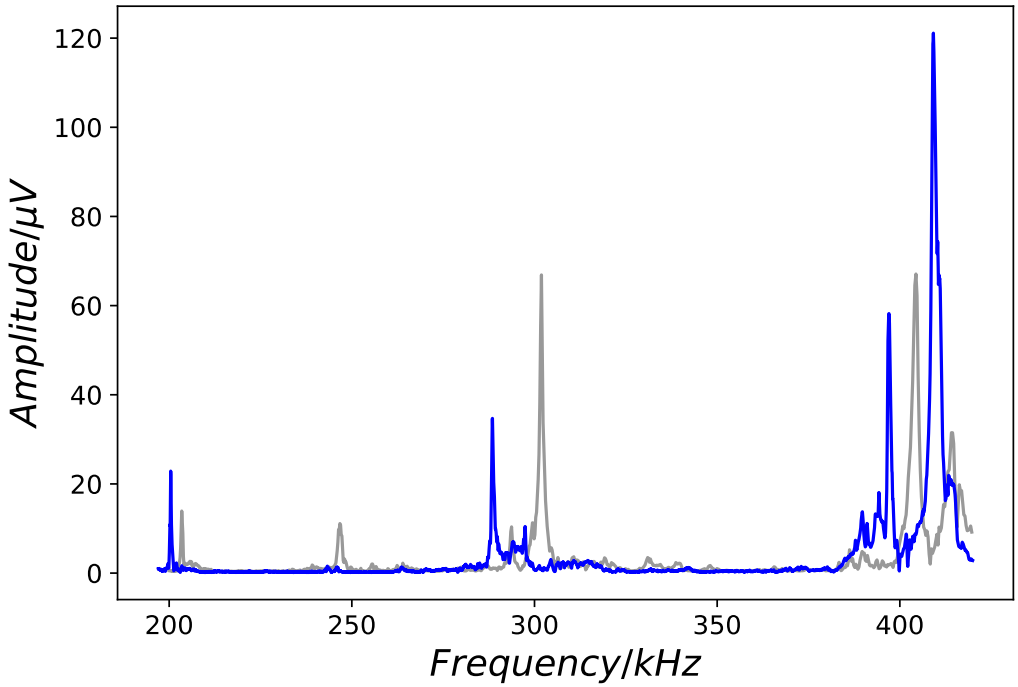

Figure 5.8: Frequency response of the driven nanowire before (grey line) and after (blue line) the calcium oven operation. Atomic calcium has been deposited on the nanowire surface and the frequency peaks have shifted towards lower values.

frequencies. This probably indicates that calcium from the oven was deposited on the nanowire. Considering the frequency shift for one of the modes, we can estimate the amount of the deposited calcium on the nanowire. Following the approximation as stated in [177,178] we consider that the spring constant and Q-factor of the nanowire after the deposition does not change significantly. Taking into account the nanowire dimensions of 20 μm in length with 100 nm diameter and a mass density of 8960 kg/m^3, we calculate its effective mass to be $M_{eff} = 5.6 \times 10^{-15}$ kg. Thus, according to the aforementioned approximation we can estimate the mass difference with respect to the frequency shift according to the equation

$$\Delta f_0 \approx -\frac{f_0}{2M_{eff}}\Delta M. \tag{5.2}$$

Considering the 7 kHz frequency shift for the 404 kHz mode and using the above value for the effective mass of the nanowire according to Eq. 5.2 the $\Delta M = 1.9 \times 10^{-16}$ kg. This is the deposited mass of the calcium on the nanowire, which corresponds to 2.8×10^9 calcium atoms according to the Avogadro's number. Following the same

approach, we observed that the frequency shift of the 302 kHz is 13.5 kHz, which leads to $\Delta M = 5.0 \times 10^{-16}$ kg corresponding to 7.5×10^9 calcium atoms. Both of those peaks give the same order of magnitude for the estimated deposited number of calcium atoms on the nanowire, which possibly means that the initial assumption for those two being the two modes of oscillation of the nanowire is correct.

Another reason that this frequency shift could be observed is temperature difference between the measurements. Those measurements were taken on different days. However, we can safely exclude this, because the diode lasers used in this experiment are more sensitive to temperature fluctuations, and the laser power was constantly monitored. The temperature in the lab and in the chamber were constant and the 866 nm laser was not fluctuating in power during the acquisition of those data. If the nanowire absorbs strongly photons from the laser this could lead to temperature difference. However, it has already been shown [74, 171] that nanowires do not absorb wavelengths larger than 600 nm, especially when the lasers are interacting with nanowires with powers less than 100 μW. In our case all of the nanowire measurements were performed with 866 nm laser at 50 μW incident beam power.

For the hybrid experiment, the calcium deposition might prove challenging in the future, as the ion axial frequency must be constantly matched to one of the nanowire modes, especially after long operation times of the calcium oven. Even a structural upgrade might not be easy to be implemented, because of the very small distances between the trapping region and the nanowire, due to the limited total travelling distance of the z-positioner that is currently used. With the choice of a z-positioner with more than 10 mm total travelling distance, calcium deposition could be reduced dramatically.

In summary, it was not feasible to identify properly the two nanowire mechanical modes, due to the aforementioned limitations. Nevertheless, we have strong evidence that the two orthogonal modes of the first mode-shape of the nanowire are the ones at 302 kHz and 404 kHz. For the hybrid experiment the nanowire can be driven at any of those frequencies, and as long as the ion frequency is matched to the nanowire's corresponding one. The hybrid dynamics can be investigated experimentally under those conditions. Moreover, the mass deposition via the nano-mechanical readout during trap loading might prove helpful for the trapped ion experiments in general,

and more precise protocols for ion loading could be established. If such an experiment is performed in cryogenic temperatures, with higher Q nanowires and with much smaller laser beam diameter, then the control would be more accurate from the thermal motion of the nanowire.

Chapter 6

Conclusions and Outlook

The main goal of this thesis was to design and build a new quantum device, which will enable the experimental studies for the hybrid system of an ultracold ion and a conductive nanowire. A new miniaturized segmented layer ion trap was fabricated within the tolerance and expectations of our design. Various custom-made components were built and assembled in the apparatus, which are crucial for the operation of the experiment. For the first time a nanowire setup has been interfaced with an ion trap. The combination of those vastly different experimental approaches lead to compromises. For instance, our nanomechanical readout setup had limitations comparing to typical nanowire experiments. Additionally, we observed many mechanical modes which modulate the nanowire at specific frequencies and which come from external factors like the frame. Unfortunately, the thermal motion of our nanowire could not be detected due to the bath temperature, the low Q-factor of the nanowire and the relatively large readout laser spot size. Thus, the characterization of the nanomechanical motion was challenging. Nevertheless, we detected the driven motion of the nanowire, which is the important one for the the first stage of the dynamics of the hybrid-system. Furthermore, with a series of nanomechanical measurements we extracted reasonable experimental aspects like the Q-factor of the nanowire, the nanowire readout laser beam diameter and the number of calcium atoms deposited on the nanowire, due to the atom oven source operation. We have concluded that the nanowire can be driven in any of the frequency responses that we observed in its spectrum for studying the hybrid dynamics. Based on those artifacts, we have realized that the nanowire might

offer versatility and better control in future trapped ion experiments, according to some limitations that they experience due to the current trapped ion technology.

Another large part of this thesis was the design of the experiment and the theoretical study of the hybrid ion-nanowire system. Thus, we have studied the classical and quantum dynamics of a trapped calcium ion under the action of an oscillating charged nanowire in the context of our experimental setup. We have explored possibilities of engineering Gaussian and non-Gaussian quantum states of the ion by a classical mechanical drive of the nanowire held at room temperature. We have presented the creation of coherent states of the ion motion by mapping the coherent motion of the nanowire, indicating that an ultracold ion could be used as a probe for a nanomechanical system. Non-Gaussian quantum states can also be created on the ion with the same drive under the influence of additional trap anharmonicities. Within a full quantum treatment of both systems, our calculations suggest the possibility of sympathetic cooling of a light nanowire, such as a carbon nanotube, by an ultracold ion if the nanowire can be precooled to the quantum regime. Additionally, it seems possible to create motional quantum states of the ion and map them onto the nanowire and vice versa. This indicates that quantum information can be encoded from one system to another. This might open new possibilities of quantum network devices, or might prove interesting in the context of quantum logic experiments of building new quantum gates. Another possibility is to create squeezed states on one of those systems and read it from the other, paving the way towards more accurate quantum sensing experiments.

Our theoretical and experimental evidences suggest that the nanowire can be used as an alternative to the quantum state engineering of atomic systems, and open up possibilities that might be challenging with the current technology. The hybrid system might prove fruitful for various applications, e.g. as a new way to shape trapping potentials and controlling trapped ion experiments, as a probe of decoherence processes of quantum and macroscopic bodies, in quantum information processing, in mass spectrometry and in quantum sensing.

Bibliography

[1] M. Montinaro, *Coupling of nanomechanical resonators to controllable quantum systems*. PhD thesis, University of Basel, 2014.

[2] M. Poot and H. S. J. van der Zaut *Physics Reports*, vol. 511, pp. 273–335, 2012.

[3] A. N. Cleland, *Foundations of nanomechanics*. Berlin and Heidelberg: Springer-Verlag, 2003.

[4] B. D. Hauer, C. Doolin, K. S. D. Beach, and J. P. Davis *Annals of Physics*, vol. 339, pp. 181–207, 2013.

[5] A. Blais, R.-S. Huang, A. Wallraff, S. M. Girvin, and R. J. Schoelkopf *Phys. Rev. A*, vol. 69, p. 062320, 2004.

[6] J. Wrachtrup and F. Jelezko *Condensed Matter*, vol. 18, p. 807, 2006.

[7] F. Waldermann, P. Olivero, J. Nunn, K. Surmacz, Z. Wang, D. Jaksch, R. Taylor, I. Walmsley, M. Draganski, P. Reichart, A. Greentree, D. Jamieson, and S. Prawer *Diamonds and Related Materials*, vol. 16, p. 1887, 2007.

[8] C. H. Bennett *Physics Today*, p. 24, 1995.

[9] N. Gisin and R. Thew *Nat. Photon.*, vol. 1, p. 165, 2007.

[10] V. Giovannetti, S. Lloyd, and L. Maccone *Phys. Rev. Lett.*, vol. 96, p. 010401, 2006.

[11] V. Giovannetti, S. Lloyd, and L. Maccone *Nat. Photon.*, vol. 5, p. 222, 2011.

[12] A. Sørensen and K. Mølmer *Phys. Rev. Lett.*, vol. 83, p. 2274, 1999.

[13] D. Meiser, J. Ye, and M. J. Holland *New J. Phys.*, vol. 10, p. 073014, 2008.

[14] C. F. Ockeloen, R. Schmied, M. F. Riedel, and P. Treutlein *Phys. Rev. Lett.*, vol. 111, p. 143001, 2013.

[15] H. J. Kimble, Y. Levin, A. B. Matsko, K. S. Thorne, and S. P. Vyatchanin *Phys. Rev. D*, vol. 65, p. 022002, 2001.

[16] K. Goda, O. Miyakawa, E. E. Mikhailov, S. Saraf, R. Adhikari, K. McKenzie, R. Ward, S. Vass, A. J. Weinstein, and N. Mavalvala *Nat. Phys.*, vol. 4, p. 472, 2008.

[17] E. L. Hahn *Phys. Rev.*, vol. 80, p. 580, 1950.

[18] W. M. Itano, D. J. Heinzen, J. J. Bollinger, and D. J. Wineland *Phys. Rev. A*, vol. 41, p. 2295, 1990.

[19] C. E. Langer, *High fidelity quantum information processing with trapped ions*. PhD thesis, University of Colorado, 2005.

[20] D. Vion, A. Aassime, A. Cottet, P. Joyez, H. Pothier, C. Urbina, D. Esteve, and M. H. Devoret *Science*, vol. 296, p. 886, 2002.

[21] J. Koch, T. M. Yu, J. Gambetta, A. A. Houck, D. I. Schuster, J. Majer, A. Blais, M. H. Devoret, G. S. M., and R. J. Schoelkopf *Phys. Rev. A*, vol. 76, p. 042319, 2007.

[22] V. Kielpinski, D.and Meyer, M. A. Rowe, C. A. Sackett, W. M. Itano, C. Monroe, and D. J. Wineland *Science*, vol. 291, p. 1013, 2001.

[23] T. Monz, K. Kim, V. A. S., P. Schindler, M. Chwalla, M. Riebe, C. F. Roos, H. Häffner, W. Hänsel, M. Hennrich, and R. Blatt *Phys. Rev. Lett.*, vol. 103, p. 200503, 2009.

[24] D. Gottesman, A. Kitaev, and J. Preskill *Phys. Rev. A*, vol. 64, p. 012310, 2001.

[25] C. Monroe, D. Meekhof, B. E. King, S. R. Jefferts, W. M. Itano, D. J. Wineland, and P. Gould *Phys. Rev. Lett.*, vol. 75, p. 4011, 1995.

[26] M. H. Anderson, J. R. Ensher, M. R. Matthews, C. E. Wieman, and E. A. Cornell *Science*, vol. 269, p. 198, 1995.

[27] K. B. Davis, M. O. Mewes, M. R. Andrews, N. J. van Druten, D. S. Durfee, D. M. Kurn, and W. Ketterle *Phys. Rev. Lett.*, vol. 75, p. 3969, 1995.

[28] D. M. Meekhof, C. Monroe, B. E. King, W. M. Itano, and D. J. Wineland *Phys. Rev. Lett.*, vol. 76, pp. 1796–1799, 1996.

[29] C. Monroe, D. M. Meekhof, B. E. King, and D. J. Wineland *Science*, vol. 272, p. 1131, 1996.

[30] D. Kienzler, H.-Y. Lo, B. Keitch, L. De Clercq, F. Leupold, F. Lindenfelser, M. Marinelli, V. Negnevitsky, and J. P. Home *Science*, vol. 347, pp. 53–56, 2015.

[31] D. Kienzler, C. Flühmann, V. Negnevitsky, H.-Y. Lo, M. Marinelli, D. Nadlinger, and J. P. Home *Phys. Rev. Lett.*, vol. 116, p. 140402, 2016.

[32] J. I. Cirac, A. S. Parkins, R. Blatt, and P. Zoller *Phys. Rev. Lett.*, vol. 70, p. 556, 1993.

[33] J. F. Poyatos, J. I. Cirac, and P. Zoller *Phys. Rev. Lett.*, vol. 77, p. 4728, 1996.

[34] D. Kienzler, H.-Y. Lo, V. Negnevitsky, C. Flühmann, M. Marinelli, and J. P. Home *Phys. Rev. Lett.*, vol. 119, p. 033602, 2017.

[35] H. Krauter, C. A. Muschik, K. Jensen, W. Wasilewski, J. M. Petersen, J. I. Cirac, and E. S. Polzik *Phys. Rev. Lett.*, vol. 107, p. 080503, 2011.

[36] Y. Lin, J. P. Gaebler, F. Reiter, T. R. Tan, R. Bowler, A. S. Sorensen, D. Leibfried, and D. J. Wineland *Nature*, vol. 504, p. 415, 2013.

[37] S. Shankar, M. Hatridge, Z. Leghtas, K. M. Sliwa, A. Narla, U. Vool, S. M. Girvin, L. Frunzio, M. Mirrahimi, and M. H. Devoret *Nature*, vol. 504, p. 419, 2013.

[38] C. Flühmann, T. L. Nguyen, M. Marinelli, V. Negnevitsky, K. Mehta, and J. P. Home *Nature*, vol. 566, p. 513, 2019.

[39] T. Ruster, C. T. Schmiegelow, H. Kaufmann, C. Warschburger, F. Schmidt-Kaler, and U. G. Poschinger *Appl. Phys. B*, vol. 122, p. 254, 2016.

[40] V. M. Schäfer, C. J. Balance, K. Thirumalai, L. J. Stephenson, T. G. Ballance, A. M. Steane, and D. M. Lucas *Nature*, vol. 555, p. 75, 2018.

[41] H. Häffner, C. F. Roos, and R. Blatt *Phys. Rep.*, vol. 469, p. 155, 2008.

[42] S. Willitsch *Int. Rev. Phys. Chem.*, vol. 31, pp. 175–199, 2012.

[43] M. Germann, X. Tong, and S. Willitsch *Nature Phys.*, vol. 10, p. 820, 2014.

[44] Y.-P. Chang, K. Dlugolecki, Küpper, D. Rösch, D. Wild, and S. Willitsch *Science*, vol. 342, p. 98, 2013.

[45] A. Kilaj, H. Gao, D. Rösch, U. Rivero, J. Küpper, and S. Willitsch *Nat. Commun.*, vol. 9, p. 2096, 2018.

[46] J. Roßnagel, S. T. Dawkins, K. N. Tolazzi, O. Abah, E. Lutz, F. Schmidt-Kaler, and K. Singer *Science*, vol. 352, pp. 325–329, 2016.

[47] T. J. Kippenberg and K. J. Vahala *Opt. Express*, vol. 15, p. 17172, 2007.

[48] T. J. Kippenberg and K. J. Vahala *Science*, vol. 321, p. 1172, 2008.

[49] F. Marquardt and S. M. Girvin *Physics*, vol. 2, p. 40, 2009.

[50] I. Favero and K. Karrai *Nat. Photon.*, vol. 3, p. 201, 2009.

[51] M. Aspelmeyer, T. J. Kippenberg, and F. Marquardt *Rev. Mod. Phys.*, vol. 86, p. 1391, 2014.

[52] J. Chan *et al. Nature*, vol. 478, pp. 89–92, 2011.

[53] S. Glöblacher, J. B. Hertzberg, M. R. Vanner, G. D. Cole, S. Gigan, K. C. Schwab, and M. Aspelmeyer *Nat. Phys.*, vol. 5, p. 485, 2009.

[54] E. Verhagen, S. Deléglise, S. Weis, A. Schliesser, and T. J. Kippenberg *Nature*, vol. 482, pp. 63–67, 2012.

[55] A. D. O'Connell *et al. Nature*, vol. 464, pp. 697–703, 2010.

[56] J. D. Teufel *et al. Nature*, vol. 475, pp. 359–363, 2011.

[57] J. D. Teufel *et al. Nature*, vol. 471, p. 204, 2011.

[58] M. Aspelmeyer, P. Meystre, and K. Schwab *Phys. Today*, vol. 65, p. 29, 2012.

[59] W. Marshall *et al. Phys. Rev. Lett.*, vol. 91, p. 130401, 2003.

[60] I. Pikovski *et al. Nat. Phys.*, vol. 8, p. 393, 2012.

[61] O. Romero-Isart *Phys. Rev. A*, vol. 84, p. 052121, 2011.

[62] O. R. Isart *et al. Phys. Rev. Lett.*, vol. 107, p. 020405, 2011.

[63] F. J. Giessibl *et al. Science*, vol. 289, p. 422, 2000.

[64] L. Gross *et al. Science*, vol. 325, p. 1110, 2009.

[65] A. K. Naik *et al. Nat. Nanotech.*, vol. 4, p. 445, 2009.

[66] A. Mehlin *et al. Nano Lett.*, vol. 15, p. 4839, 2015.

[67] B. Gross *et al. Phys. Rev. B*, vol. 93, p. 064409, 2016.

[68] A. C. Bleszynski-Jayich *et al. Science*, vol. 326, p. 272, 2009.

[69] U. Gysin *et al. Rev. Sci. Inst.*, vol. 82, p. 023705, 2011.

[70] M. Langer *et al. Nat. Mater.*, vol. 13, p. 173, 2013.

[71] D. Rugar *et al. Nature*, vol. 430, p. 329, 2004.

[72] C. L. Degen *et al. PNAS*, vol. 106, p. 1313, 2009.

[73] N. Rossi, F. R. Braakman, D. Cadeddu, D. Vasyukov, G. Tütüncüoglu, A. Fontcuberta I Morral, and M. Poggio *Nat. Nanotech.*, vol. 12, pp. 150–155, 2017.

[74] L. M. De Lépinay, B. Pigeau, B. Besga, P. Vincent, P. Poncharal, and O. Arcizet *Nat. Nanotech.*, vol. 12, pp. 156–162, 2017.

[75] J. Moser *et al. Nat. Nanotech.*, vol. 8, p. 493, 2013.

[76] S. L. de Bonis *et al. Nano Lett.*, vol. 18, p. 5324, 2018.

[77] J. Chaste *et al. Nat. Nanotech.*, vol. 7, p. 301, 2012.

[78] D. Meiser and P. Meystre *Phys. Rev. A*, vol. 73, p. 033417, 2006.

[79] C. Genes *et al. Phys. Rev. A*, vol. 77, p. 050307, 2008.

[80] H. Ian *et al. Phys. Rev. A*, vol. 78, p. 013824, 2008.

[81] Y. Chang *et al. Phys. Rev. A*, vol. 83, p. 063826, 2011.

[82] A. B. Bhattacherjee *Phys. Rev. A*, vol. 80, p. 043607, 2009.

[83] K. Zhang *et al. Phys. Rev. A*, vol. 81, p. 013802, 2010.

[84] K. Hammerer *et al. Phys. Rev. Lett.*, vol. 102, p. 020501, 2009.

[85] K. Hammerer *et al. Phys. Rev. Lett.*, vol. 103, p. 063005, 2009.

[86] M. Wallquist *et al. Phys. Rev. A*, vol. 81, p. 023816, 2010.

[87] K. Hammerer *et al. Phys. Rev. A*, vol. 82, p. 021803, 2010.

[88] D. Hunger, S. Camerer, M. Korppi, A. Jöckel, T. W. Hänsch, and P. Treutlein *C. R. Physique*, vol. 12, pp. 871–887, 2011.

[89] P. Treutlein *et al. Phys. Rev. Lett.*, vol. 99, p. 140403, 2007.

[90] D. Hunger, S. Camerer, T. W. Hänsch, D. König, J. P. Kotthaus, J. Reichel, and P. Treutlein *Phys. Rev. Lett.*, vol. 104, p. 143002, 2010.

[91] S. Camerer *et al. Phys. Rev. Lett.*, vol. 107, p. 223001, 2011.

[92] M. Korppi *et al. EPJ Web of Conferences*, vol. 57, p. 03006, 2013.

[93] B. Vogell *et al. Phys. Rev. A*, vol. 87, p. 023816, 2013.

[94] L. Tian and P. Zoller *Phys. Rev. Lett.*, vol. 93, p. 266403, 2004.

[95] W. K. Hensinger, D. W. Utami, H.-S. Goan, K. Schwab, C. Monroe, and G. J. Milburn *Phys. Rev. A*, vol. 72, p. 041405, 2005.

[96] S. Kotler, R. W. Simmonds, D. Leibfried, and D. J. Wineland *Phys. Rev. A*, vol. 95, p. 022327, 2017.

[97] C. F. Foot, *Atomic Physics*. Oxford: Oxford University Press, 2005.

[98] D. J. Berkeland, J. D. Miller, J. C. Bergquist, W. M. Itano, and D. J. Wineland *J. Appl. Phys.*, vol. 83, p. 5025, 1998.

[99] M. G. Raizen, J. M. Gilligan, J. C. Bergquist, W. M. Itano, and D. J. Wineland *Phys. Rev. A.*, vol. 45, p. 6493, 1992.

[100] F. G. Major, V. N. Gheorghe, and G. Werth, *Charged Particle Traps.* Berlin and Heidelberg: Springer, 2005.

[101] A. Drakoudis, M. Söllner, and G. Werth *Int. J. Mass Spectrom.*, vol. 252, p. 61, 2006.

[102] M. G. House *Phys. Rev. A*, vol. 78, p. 033402, 2008.

[103] F. A. Shaikh and A. Ozakin *J. Appl. Phys.*, vol. 112, p. 074904, 2012.

[104] J. P. Home, D. Hanneke, J. D. Jost, D. Leibfried, and D. J. Wineland *New J. Phys.*, vol. 13, p. 073026, 2011.

[105] D. J. Wineland, C. Monroe, W. M. Itano, D. Leibfried, B. E. King, W. M., and D. M. Meekhof *J. Res. Natl. Stand. Technol.*, vol. 103, pp. 259–328, 1998.

[106] D. Gerlich *Adv. Chem. Phys.*, vol. 81, p. 1, 1992.

[107] H. J. Metcalf and P. van der Straten, *Laser Cooling and Trapping.* New York: Springer, 1999.

[108] D. J. Wineland, J. C. Bergquist, W. M. Itano, J. J. Bollinger, and C. H. Manney *Phys. Rev. Lett.*, vol. 59, p. 2935, 1987.

[109] S. Webster, *Raman sideband cooling and coherent manipulation of trapped ions.* PhD thesis, Oxford University, 2005.

[110] J. H. Wasenberg *Phys. Rev. A*, vol. 78, p. 063410, 2008.

[111] R. Schmied *New J. Phys.*, vol. 12, p. 023038, 2010.

[112] C. B. Zhang, D. Offenberg, B. Roth, M. A. Wilson, and S. Schiller *Phys. Rev. A*, vol. 76, p. 012719, 2007.

[113] J. P. Schiffer, M. Drewsen, J. S. Hangst, and L. Hornekaer *Proc. Natl. Acad. Sci.*, vol. 97, p. 10697, 2001.

[114] J. P. Schiffer *J. Phys. B*, vol. 36, p. 511, 2003.

[115] K. Okada, M. Wada, T. Takayanagi, S. Ohtani, and H. A. Schuessler *Phys. Rev. A*, vol. 81, p. 013420, 2010.

[116] D. H. E. Dubin and T. M. O'Neil *Phys. Rev. Lett.*, vol. 60, p. 511, 1988.

[117] X. Tong, D. Wild, and S. Willitsch *Phys. Rev. A*, vol. 83, p. 023415, 2011.

[118] A. Mokhberi and S. Willitsch *New J. Phys.*, vol. 17, p. 045008, 2015.

[119] I. Rouse and S. Willitsch *Phys. Rev. A*, vol. 92, p. 053420, 2015.

[120] T. Matthey, T. Cickovski, S. S. Hampton, A. Ko, Q. Ma, M. Nyerges, T. Raeder, T. Slabach, and J. A. Izaguirre *ACM Trans. Math. Softw.*, vol. 30, p. 237, 2004.

[121] H. Kaufmann, S. Ulm, G. Jacob, U. Poschinger, H. Landa, A. Retzker, M. B. Plenio, and F. Schmidt-Kaler *Phys. Rev. Lett.*, vol. 109, p. 263003, 2012.

[122] I. Rouse, *A miniaturized hybrid ion-atom chip trap and the non-equilibrium statistical mechanics of trapped ions.* PhD thesis, University of Basel, 2018.

[123] S. Han, H. Benaroya, and T. Wei *Journal of Sound and Vibration*, vol. 225, pp. 935–938, 1999.

[124] A. A. Clerk, M. H. Devoret, S. M. Girvin, F. Marquardt, and R. J. Schoelkopf *Reviews of Modern Physics*, vol. 82, pp. 1155–1208, 2010.

[125] M. Poggio, C. L. Degen, H. J. Mamin, and D. Rugar *Phys. Rev. Lett.*, vol. 99, p. 017201, 2007.

[126] D. Kielpinski, C. Monroe, and D. J. Wineland *Nature*, vol. 417, pp. 709–711, 2002.

[127] M. D. Hughes, B. Lekitsch, J. A. Broersma, and W. K. Hensinger *Contemp. Phys.*, vol. 52, p. 52, 2011.

[128] M. Madsen, W. Hensinger, D. Stick, J. Rabchuk, and C. Monroe *Appl. Phys. B*, vol. 78, p. 639, 2004.

[129] D. Kienzler, *Quantum Harmonic Oscillator State Synthesis by Reservoir Engineering*. PhD thesis, ETH Zürich, 2015.

[130] J. Labaziewicz, Y. Ge, P. Antohi, D. Leibrandt, K. R. Brown, and I. L. Chuang *Phys. Rev. Lett.*, vol. 100, p. 013001, 2008.

[131] L. Deslauriers, S. Olmschenk, D. Stick, W. K. Hensinger, and Monroe *Phys. Rev. Lett.*, vol. 97, p. 103007, 2006.

[132] D. T. C. Allcock, L. Guidoni, T. P. Harty, C. Ballance, M. Blain, A. Steane, and D. M. Lucas *New J. Phys.*, vol. 13, p. 123023, 2011.

[133] D. A. Hite, A. C. Colombe, A. C. Wilson, K. R. Brown, U. Warring, R. Jördens, J. D. Jost, K. S. McKay, D. P. Pappas, D. Leibfried, and D. J. Wineland *Phys. Rev.A*, vol. 109, p. 103001, 2012.

[134] N. Daniilidis, S. Narayanan, S. A. Möller, R. Clark, T. E. Lee, P. J. Leek, S. Wallraff, S. Schulz, F. Schmidt-Kaler, and H. Häffner *New. J. Phys.*, vol. 13, p. 013032, 2011.

[135] K. Singer, U. Poschinger, M. Murphy, P. Ivanov, F. Ziesel, T. Calarco, and F. Schmidt-Kaler *Rev. Mod. Phys.*, vol. 872, p. 2609, 2010.

[136] *COMSOL Multiphyics*. https://www.comsol.com/.

[137] R. Blakestad, *Transport of trapped-ion qubits within a scalable quantum processor*. PhD thesis, University of Colorado, 2010.

[138] W. Macalpine and R. Schildknecht *Proceedings of the IRE*, vol. 47, p. 2099, 1959.

[139] J. D. Siverns, I. R. Simkins, S. Weidt, and W. K. Hensinger *Appl. Phys. B*, vol. 107, p. 921, 2012.

[140] S. Gulde *et al. Appl. Phys. B*, vol. 73, p. 861, 2001.

[141] D. M. Lucas *et al. Phys. Rev. A*, vol. 69, p. 012711, 2004.

[142] T. Matthey *et al. ACM Trans. Math. Softw.*, vol. 30, p. 237, 2004.

[143] G. Lindblad *Commun. Math. Phys.*, vol. 48, p. 119, 1976.

[144] S. Haroche and J.-M. Raimond, *Exploring the quantum: Atoms and cavities and photons*. Oxford: Oxford University Press, 2006.

[145] H.-P. Breuer and F. Petruccione, *The theory of open quantum systems*. Oxford: Oxford University Press, 2002.

[146] K. Mølmer, Y. Castin, and J. Dalibard *J. Opt. Soc. Amer. B*, vol. 10, p. 524, 1993.

[147] C. G. Gerry and P. L. Knight, *Introductory Quantum Optics*. Cambridge: Cambridge University Press, 2005.

[148] R. Loudon, *The quantum theory of light*. Oxford: Oxford University Press, 1973.

[149] M. Fox, *Quantum optics: An introduction*. Oxford: Oxford University Press, 1973.

[150] D. Leibfried, R. Blatt, C. Monroe, and D. J. Wineland *Rev. Mod. Phys.*, vol. 75, p. 281, 2003.

[151] J. Alonso, F. M. Leupold, Z. U. Solèr, M. Fadel, M. Marinelli, B. C. Keitch, V. Negnevitsky, and J. P. Home *Nat. Commun.*, vol. 7, p. 11243, 2016.

[152] J. F. Poyatos *et al. Phys. Rev. A*, vol. 53, p. R1966, 1996.

[153] P. C. Haljan *Phys. Rev. A*, vol. 72, p. 062316, 2005.

[154] M. J. McDonnell *et al. Phys. Rev. Lett.*, vol. 98, p. 063603, 2007.

[155] U. Poschinger *et al. Phys. Rev. Lett.*, vol. 105, p. 263602, 2010.

[156] D. J. Wineland *Rev. Mod. Phys.*, vol. 85, p. 1103, 2013.

[157] S. Haroche *Rev. Mod. Phys.*, vol. 85, p. 1083, 2013.

[158] B. Vlastakis *Science*, vol. 342, p. 607, 2013.

[159] E. Laird, F. Kuemmeth, G. Steele, K. Grove-Rasmussen, J. Nygård, K. Flensberg, and L. Kouwenhoven *Rev. Mod. Phys.*, vol. 87, p. 703, 2015.

[160] J. Charlier, X. Blase, and S. Roche *Rev. Mod. Phys.*, vol. 79, p. 677, 2007.

[161] B. Vogell, T. Kampschulte, M. Rakher, A. Faber, P. Treutlein, K. Hammerer, and P. Zoller *New J. Phys.*, vol. 17, p. 043044, 2015.

[162] M. Palma, D. Maradan, L. Casparis, T. M. Liu, F. N. M. Froning, and D. M. Zumbühl *Rev. Sci. Inst.*, vol. 88, p. 043902, 2017.

[163] G. Meyer and N. M. Amer *Appl. Phys. Lett.*, vol. 53, p. 12, 1988.

[164] K. Karrai and R. D. Grober *Appl. Phys. Lett.*, vol. 66, p. 14, 1995.

[165] K. Karrai and R. D. Grober *Appl. Phys. Lett.*, vol. 73, p. 26, 1998.

[166] C. A. Regal, J. D. Teufel, and K. W. Lehnert *Nat. Phys.*, vol. 4, pp. 555–560, 2008.

[167] T. Faust *et al. Nat. Commun.*, vol. 3, p. 728, 2012.

[168] V. Sazonova *et al. Nature*, vol. 431, pp. 284–287, 2004.

[169] V. Nigués, A. Siria, and P. Verlot *Nat. Commun.*, vol. 6, p. 7006, 2015.

[170] I. Tsioutsios *et al. Nano Lett.*, vol. 17, p. 1748, 2017.

[171] A. Gloppe *et al. Nat. Nanotech.*, vol. 9, pp. 920–926, 2014.

[172] B. Sanii and P. D. Ashby *Phys. Rev. Lett.*, vol. 104, p. 147203, 2010.

[173] D. Rugar, H. J. Mamin, and P. Guethner *Appl. Phys. Lett.*, vol. 55, p. 2588, 1989.

[174] J. M. Nichol, T. R. Naibert, E. R. Hemesath, L. J. Lauchon, and R. Budakian *Phys. Rev. X*, vol. 3, p. 031016, 2013.

[175] N. Rossi, *Force sensing with nanowires*. PhD thesis, University of Basel, 2019.

[176] D. Cadeddu, *Nanomechanics and scanning probe microscopy with nanowires*. PhD thesis, University of Basel, 2018.

[177] K. L. Ekinci *et al. J. Appl. Phys.*, vol. 95, p. 2682, 2004.

[178] A. Mehlin, *Dynamic Cantilever Magnetometry of Reversal Processes and Phase Transitions in Individual Nanomagnets.* PhD thesis, University of Basel, 2017.

List of Publications

- P. N. Fountas, M. Poggio and S. Willitsch, "Classical and quantum dynamics of a trapped ion coupled to a charged nanowire", *New Journal of Physics* **21** 013030 (2019).

- P. N. Fountas, G. A. Souliotis, M. Veselsky and A. Bonasera, "Systematic study of neutron-rich rare-isotope production in peripheral heavy-ion collisions below the Fermi energy", *Physical Review C* **90** 064613 (2014)

- G. A. Souliotis, P. N. Fountas, M. Veselsky, S. Galanopoulos, Z. Kohley, A. McIntosh, S. J. Yenello and A. Bonasera, "Isoscalling heavy projectile residues and N/Z equilibration in peripheral heavy-ion collisions below the Fermi energy", *Physical Review C* **90** 064612 (2014)